

# A first-principle study on lattice properties and atom positions of TiNiCu shape memory alloys

Gou, Liangliang

2016

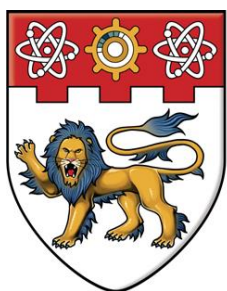
Gou, L. (2016). A first-principle study on lattice properties and atom positions of TiNiCu shape memory alloys. Doctoral thesis, Nanyang Technological University, Singapore.

<https://hdl.handle.net/10356/68525>

<https://doi.org/10.32657/10356/68525>

---

**NANYANG TECHNOLOGICAL UNIVERSITY**



**NANYANG  
TECHNOLOGICAL  
UNIVERSITY**

**A First-Principle Study on Lattice Properties and  
Atom Positions of TiNiCu Shape Memory Alloys**

by

Gou Liangliang

Supervisor: A/P Liu Yong

Co-supervisor: A/P Ng Teng Yong

A dissertation submitted to Nanyang Technological University in partial

fulfilment of the requirements for the degree of

DOCTOR OF PHILOSOPHY

School of Mechanical and Aerospace Engineering

2016

---

---

# Acknowledgements

First of all, I wish to express my greatest gratitude to my supervisor Associate Professor Liu Yong and co-supervisor Associate Professor Ng Teng Yong. Without their academic guidance and invaluable encouragement, the studies presented in this report would neither have started nor finished. They are not only professional mentors but also wonderful gentlemen. From them, I have not only learnt the methods and knowledge associated with the research, but also a life-long treasure of the smart thinking and analytical skill.

Then, many thanks go to my senior apprentice, Yan Lina. During the research period, she gave me many constructive suggestions and supports both on my research and course work.

Meanwhile, I would like to thank all my teachers, friends and families, for their consistent support and encouragement.

Many thanks also go to High Performance Computing Center at Nanyang Technological University. Parts of the computations were carried out on their hpc-rds platform.

Last but not least, my heartfelt thanks go to my parents and my girlfriend Gu Yan. Their consistent love, encouragement and support are always the best impetus to my studies as well as to my life.

---

---

# Abstract

Since its discovery, TiNi-based shape memory alloys (SMAs) have attracted much attention and have spawned various innovative applications in the biomedical, aerospace, robotic and automotive industries. Besides high strength, ductility and biocompatibility, TiNi-based SMAs exhibit unique properties such as shape memory effect (SME) and superelasticity (SE) which are associated with reversible martensitic transformation (MT). However, even as TiNi-based SMAs have been discovered and used for many decades, a refined atomic-level understanding of MT is still lacking. With the rapid development of high performance computing, computational methods are playing an increasingly important role in materials research. By using computational methods, the martensite structures of TiNi-based SMAs at quantum level are explored in detail here.

In the present work, the martensite crystal structures, electronic structures and atomic displacements of TiNi and TiNiCu alloys have been studied based on ab initio Density Functional Theory (DFT) calculations. The computational results are compared with previous experimental data and it is found that the equilibrium lattice constants are in good agreement with reported values. It is observed that for TiNiCu alloys with Cu content between 0 at% to 25 at%, and

---

this Cu addition to TiNi, the martensite lattice parameters  $a$  and  $c$  and the monoclinic angle decrease, whereas the lattice parameter  $b$  increases. When Cu content reaches 20 at%, the monoclinic martensite crystal structure becomes unstable and an orthorhombic crystal structure is formed. However, when Cu content exceeds 25 at%, the changes of lattice parameters are insignificant, in which  $a$  decreases slightly while  $b$  and  $c$  increase slightly, and the stable martensite structure remains orthorhombic.

Furthermore, as a result of Cu addition to TiNi, the electrons which escape from Ti atom increase linearly. Since each Cu atom attracts more electrons than Ni atom, fewer charge transfer from Ti to Ni has occurred compared to that in binary TiNi alloy. With increasing Cu content, the distance between two neighboring Ni/Cu atoms increases along the  $x$ -axis while two neighboring Ti atoms get closer, which is responsible for the rotation of the (100) plane, leading to a decrease in the monoclinic angle. The charge transfer between Ti and Ni/Cu atoms is suggested to be responsible for the observed atomic displacements. Since the displacements of both Ti and Ni/Cu atoms along the  $x$ -axis are progressive, there is no dramatic change in TiNiCu martensite crystal structures but the monoclinic angle decreases gradually until the orthorhombic structure is formed.

---

## List of Publications

1. “An investigation on the crystal structures of  $\text{Ti}_{50}\text{Ni}_{50-x}\text{Cu}_x$  shape memory alloys based on density functional theory calculations”  
**Gou L**, Liu Y, Ng TY.  
**Intermetallics** 53:20-25 (2014).
2. “Crystal structures of  $\text{Ti}_{50}\text{Ni}_{50-x}\text{Cu}_x$  shape memory alloys investigated by DFT calculations”  
**Gou L**, Liu Y, Ng T Y.  
**Proceedings of SMART 2015, the 7th ECCOMAS Thematic Conference on Smart Structures and Materials, 3 – 5 June 2015, Ponta Delgada, Azores, Portugal** (2015).
3. “Effect of Cu content on atomic positions of  $\text{Ti}_{50}\text{Ni}_{50-x}\text{Cu}_x$  shape memory alloys based on density functional theory calculations”  
**Gou L**, Liu Y, Ng T Y.  
**Metals** 5: 2222-2235 (2015).
4. “Effect of charge transfers on lattice properties of  $\text{TiNiCu}$  shape memory alloys”  
**Gou L**, Liu Y, Ng TY.  
**In preparation.**

---

---

# Contents

<b>Acknowledgements .....</b>	<b>I</b>
<b>Abstract.....</b>	<b>II</b>
<b>List of Publications .....</b>	<b>IV</b>
<b>Contents .....</b>	<b>V</b>
<b>List of Figures.....</b>	<b>VIII</b>
<b>List of Tables .....</b>	<b>XI</b>
<b>List of Abbreviations and Symbols .....</b>	<b>XII</b>
<b>Chapter 1 Introduction.....</b>	<b>1</b>
1.1 Background of the research problem .....	1
1.2 Objective and Scope .....	5
1.3 Organization of The Thesis.....	8
<b>Chapter 2 Literature Review on TiNi-based SMAs.....</b>	<b>10</b>
2.1 Shape Memory Alloys and Related Phenomena .....	10
2.1.1 Shape Memory Alloys .....	10
2.1.2 TiNi-based Shape Memory Alloys.....	11
2.1.3 Shape Memory Effect .....	15
2.1.3.1 Mechanism of Shape Memory Effect.....	16
2.1.3.2 One-way Shape Memory Effect.....	18
2.1.3.3 Two-way Shape Memory Effect .....	19
2.1.4 Superelasticity .....	21
2.1.5 Application of Shape Memory Alloys .....	23
2.2 Phase Transformations in TiNi-based SMAs.....	26
2.2.1 Crystal Structures in TiNi-based SMAs.....	27
2.2.2 Temperature-induced Martensitic Transformation .....	30

---

2.2.3 Stress-induced Martensitic Transformation .....	31
2.3 Transformation Paths in TiNi-based SMAs .....	32
2.4 Recent Computational Studies of TiNi-based SMAs.....	39
<b>Chapter 3 First-Principle Method .....</b>	<b>46</b>
3.1 Background .....	46
3.2 The Schrödinger Equation.....	47
3.3 Hartree-Fock Theory .....	49
3.3.1 Slater Determinant .....	50
3.3.2 Hartree-Fock Theory .....	52
3.3.3 Limitations of Hartree-Fock Theory .....	53
3.4 Density Functional Theory .....	54
3.4.1 Hohenberg-Kohn Theorem .....	55
3.4.2 Kohn-Sham Theory.....	57
3.4.3 Local Density Approximation.....	59
3.4.4 Generalized Gradient Approximation .....	60
3.4.5 Limitations of Density Functional Theory .....	61
3.5 CASTEP Based on DFT.....	62
3.5.1 Geometry Optimization.....	63
3.5.2 Pseudopotentials.....	64
3.5.3 Energy Cutoff.....	66
3.5.4 Mulliken Population Analysis.....	66
3.5.5 The Density of State.....	67
3.6 Convergence Test .....	69
3.7 Structure Optimization of Equiatomic TiNi in Martensite.....	71
<b>Chapter 4 Calculated Results and Related Discussions .....</b>	<b>77</b>
4.1 Background .....	77
4.2 Computational Methodology.....	78
4.3 Effect of Cu Content on Crystal Structure of TiNiCu SMAs.....	79
4.3.1 Research Method.....	79
4.3.2 Results and Discussions .....	82



---

---

4.3.3 Summary .....	91
4.4 Effect of Cu Content on Atom Positions of TiNiCu SMAs .....	92
4.4.1 Research Method.....	92
4.4.2 Results and Discussions .....	94
4.4.3 Summary .....	106
4.5 Effect of Charge Transfers on Lattice Properties of TiNiCu SMAs .....	107
4.5.1 Research Method.....	108
4.5.2 Results and Discussions .....	109
4.5.3 Summary .....	119
<b>Chapter 5 Conclusions and Future Work .....</b>	<b>121</b>
5.1 Summary .....	121
5.2 Conclusions .....	122
5.3 Suggestions for Future Work .....	124
<b>Reference .....</b>	<b>127</b>

---

## List of Figures

Figure 2.1 Phase diagram of TiNi alloy [49].	12
Figure 2.2 A Typical DSC Curve of TiNi Shape Memory Alloy	13
Figure 2.3 Relationship between nickel content and transformation start temperature [51].	14
Figure 2.4 Schematic of a stress-strain-temperature curve showing the shape memory effect [56].	16
Figure 2.5 Mechanism of shape memory effect: (a) original parent single crystal, (b) self-accommodated martensite, (c-d) deformation of martensite proceeds by the growth of one variant at the expense of the other, (e) upon heating to a temperature above $A_f$ , each variant reverts to the parent phase in the original orientation by the reverse transformation [63].	18
Figure 2.6 Illustration of two-way shape memory effect [64].	20
Figure 2.7 Schematic of a superelastic stress-strain diagram [56].	22
Figure 2.8 Applications of shape memory component in automotive [76-78].	24
Figure 2.9 The variable geometry chevron developed by Boeing [88].	25
Figure 2.10 Example of biomedical application of SMAs [106].	26
Figure 2.11 Crystal structure of TiNi alloys (a) in austenite B2 phase (b) in martensite B19' phase.	28
Figure 2.12 Phase transformation versus temperature curve.	31
Figure 2.13 Three transformation paths in TiNi-based alloys [71].	32
Figure 2.14 Electrical resistivity and temperature curves for the three martensitic transformations in TiNi-based alloys: (a) B2-B19' transformation; (b) B2-R-B19' transformation; (c) B2-B19-B19' transformation [71].	34
Figure 2.15 Effect of Cu content on transformation temperatures of TiNiCu alloys [121].	36
Figure 2.16 Elongation( $\epsilon$ )-temperature(T) curves under the nearly same stress (about 40 MPa) for TiNiCu alloys [121].	37
Figure 2.17 Lattice parameters of TiNiCu alloys with different Cu content [122].	38
Figure 2.18 Lattice parameters of TiNiCu martensite phase with different Cu content [123].	39
Figure 2.19 The BCO minimum-energy structure with further doubled conventional cell (shaded box) [126].	40
Figure 2.20 The twinned supercells constructed using (a) B19' structural parameters and (b) BCO structural parameters before their optimization. (c) The result of the optimization process. [131].	42

Figure 2.21 Crystal structure of B19'' phase [134].	43
Figure 2.22 Energy of B19', B19'' and BCO with different monoclinic angle [134].	43
Figure 2.23 The 2×2×2 supercells of (a) Ti <sub>50</sub> Ni <sub>50</sub> ; (b) Ti <sub>50</sub> Ni <sub>43.75</sub> Cu <sub>6.25</sub> ; (c) Ti <sub>50</sub> Ni <sub>37.5</sub> Cu <sub>12.5</sub> ; (d) Ti <sub>50</sub> Ni <sub>31.25</sub> Cu <sub>18.75</sub> ; (e) Ti <sub>50</sub> Ni <sub>25</sub> Cu <sub>25</sub> . [137].	44
Figure 3.1 Flow chart of Hartree-Fock method.	53
Figure 3.2 Flow chart of DFT method.	62
Figure 3.3 Convergence test for cutoff energy.	70
Figure 3.4 Convergence test for k-points.	71
Figure 3.5 Energy change during optimization.	73
Figure 3.6 Illustration of optimization convergence.	74
Figure 3.7 (a) DOS of BCO; (b) DOS of B19''; (c) PDOS of BCO; (d) PDOS of B19''.	75
Figure 4.1 Initial unit cells and supercells of Ti <sub>50</sub> Ni <sub>50-x</sub> Cu <sub>x</sub> (a) unit cell of Ti <sub>50</sub> Ni <sub>25</sub> Cu <sub>25</sub> (b) 1×1×2 supercell of Ti <sub>50</sub> Ni <sub>25</sub> Cu <sub>25</sub> (c) 1×1×5 supercell of Ti <sub>50</sub> Ni <sub>25</sub> Cu <sub>25</sub> (d, e) 1×1×2 supercell of Ti <sub>50</sub> Ni <sub>37.5</sub> Cu <sub>12.5</sub> (f) 1×1×5 supercell of Ti <sub>50</sub> Ni <sub>45</sub> Cu <sub>5</sub> (g) unit cell of Ti <sub>50</sub> Ni <sub>50</sub> (h) 1×1×5 supercell of Ti <sub>50</sub> Ni <sub>35</sub> Cu <sub>15</sub> (i) 1×1×4 supercell of Ti <sub>50</sub> Ni <sub>31.25</sub> Cu <sub>18.75</sub> (j) 1×1×5 supercell of Ti <sub>50</sub> Ni <sub>30</sub> Cu <sub>20</sub> .	81
Figure 4.2 Density of states (DOS) for (a) Ti <sub>50</sub> Ni <sub>50</sub> ; (b) Ti <sub>50</sub> Ni <sub>45</sub> Cu <sub>5</sub> ;	86
Figure 4.3 Variation of lattice parameters with Cu content.	88
Figure 4.4 Variation of unit cell volume and monoclinic angle with Cu content.	89
Figure 4.5 Schematic of the unit cell of (a) B19' martensite structure, and (b) B19 martensite structure.	93
Figure 4.6 Projections of the martensite crystal structures along <010> direction of (a) binary Ti <sub>50</sub> Ni <sub>50</sub> ; (b) Ti <sub>50</sub> Ni <sub>45</sub> Cu <sub>5</sub> ; (c) Ti <sub>50</sub> Ni <sub>37.5</sub> Cu <sub>12.5</sub> ; (d) Ti <sub>50</sub> Ni <sub>35</sub> Cu <sub>15</sub> ; (e) Ti <sub>50</sub> Ni <sub>31.25</sub> Cu <sub>18.75</sub> ; (f) Ti <sub>50</sub> Ni <sub>30</sub> Cu <sub>20</sub> and (g) Ti <sub>50</sub> Ni <sub>25</sub> Cu <sub>25</sub> , comparing the typical relative average positions of Ni site (blue) and Ti site (grey) along 'a' and 'c' lattice parameters with respect to the binary alloy.	97
Figure 4.7 3-D diagrams showing the atomic positions of (a) Ti <sub>50</sub> Ni <sub>45</sub> Cu <sub>5</sub> ; (b) Ti <sub>50</sub> Ni <sub>37.5</sub> Cu <sub>12.5</sub> ; (c) Ti <sub>50</sub> Ni <sub>35</sub> Cu <sub>15</sub> ; (d) Ti <sub>50</sub> Ni <sub>31.25</sub> Cu <sub>18.75</sub> ; (e) Ti <sub>50</sub> Ni <sub>30</sub> Cu <sub>20</sub> and (f) Ti <sub>50</sub> Ni <sub>25</sub> Cu <sub>25</sub> .	98
Figure 4.8 Schematic diagram showing the transition of martensite crystal structure from B19' to B19 as a result of Cu addition in TiNi.	100
Figure 4.9 Variation of Ni/Cu-Ti bond length with Cu content.	102
Figure 4.10 Band structures and associated partial density of states for (a) binary Ti <sub>50</sub> Ni <sub>50</sub> ; (b) Ti <sub>50</sub> Ni <sub>45</sub> Cu <sub>5</sub> ; (c) Ti <sub>50</sub> Ni <sub>37.5</sub> Cu <sub>12.5</sub> ; (d) Ti <sub>50</sub> Ni <sub>35</sub> Cu <sub>15</sub> ; (e) Ti <sub>50</sub> Ni <sub>31.25</sub> Cu <sub>18.75</sub> ; (f) Ti <sub>50</sub> Ni <sub>30</sub> Cu <sub>20</sub> ; and (g) Ti <sub>50</sub> Ni <sub>25</sub> Cu <sub>25</sub> with the Fermi level defined at 0 eV.	103

---

Figure 4.11 2D total electron density projection plots in the XZ plane with color legend indicating magnitude of charge distribution for (a) binary $\text{Ti}_{50}\text{Ni}_{50}$ ; (b) $\text{Ti}_{50}\text{Ni}_{45}\text{Cu}_5$ ; (c) $\text{Ti}_{50}\text{Ni}_{37.5}\text{Cu}_{12.5}$ ; (d) $\text{Ti}_{50}\text{Ni}_{35}\text{Cu}_{15}$ ; (e) $\text{Ti}_{50}\text{Ni}_{31.25}\text{Cu}_{18.75}$ ; (f) $\text{Ti}_{50}\text{Ni}_{30}\text{Cu}_{20}$ ; and (g) $\text{Ti}_{50}\text{Ni}_{25}\text{Cu}_{25}$ . .....	105
Figure 4.12 Initial unit cells and supercells of $\text{Ti}_{50}\text{Ni}_{50-x}\text{Cu}_x$ (a) unit cell of $\text{Ti}_{50}\text{Ni}_{25}\text{Cu}_{25}$ (b) $1 \times 1 \times 5$ supercell of $\text{Ti}_{50}\text{Ni}_{20}\text{Cu}_{30}$ (c) $1 \times 1 \times 5$ supercell of $\text{Ti}_{50}\text{Ni}_{15}\text{Cu}_{35}$ (d) $1 \times 1 \times 2$ supercell of $\text{Ti}_{50}\text{Ni}_{12.5}\text{Cu}_{37.5}$ (e) $1 \times 1 \times 5$ supercell of $\text{Ti}_{50}\text{Ni}_{10}\text{Cu}_{40}$ (f) $1 \times 1 \times 5$ supercell of $\text{Ti}_{50}\text{Ni}_5\text{Cu}_{45}$ (g) unit cell of $\text{Ti}_{50}\text{Cu}_{50}$ . ...	109
Figure 4.13 Variation of lattice parameters and monoclinic angle with Cu content. ....	112
Figure 4.14 Density of states (DOS) for (a) $\text{Ti}_{50}\text{Ni}_{25}\text{Cu}_{25}$ ; (b) $\text{Ti}_{50}\text{Ni}_{20}\text{Cu}_{30}$ ; (c) $\text{Ti}_{50}\text{Ni}_{15}\text{Cu}_{35}$ ; (d) $\text{Ti}_{50}\text{Ni}_{12.5}\text{Cu}_{37.5}$ ; (e) $\text{Ti}_{50}\text{Ni}_{10}\text{Cu}_{40}$ ; (f) $\text{Ti}_{50}\text{Ni}_5\text{Cu}_{45}$ and (g) $\text{Ti}_{50}\text{Cu}_{50}$ . ....	113
Figure 4.15 (a) 3-D illustration of $\text{Ti}_{50}\text{Ni}_{25}\text{Cu}_{25}$ (b) Variation of charge transfer and Ni/Cu-Ti bond length with Cu content. ....	117

---



---

## List of Tables

Table 2.1 Crystal structures and lattice parameters of the different phases in TiNiCu alloys.....	39
Table 3.1 Crystallographic data and atomic parameters of TiNi BCO and B19".	72
Table 3.2 Atomic Mulliken populations of BCO and B19".....	74
Table 4.1 Lattice parameters of B2, B19, B19' and BCO from previous experimental and theoretical work.....	80
Table 4.2 Lattice parameters and free energy of $\text{Ti}_{50}\text{Ni}_{50-x}\text{Cu}_x$ alloys obtained by the Supercell Method.....	83
Table 4.3 Lattice parameters and free energy of $\text{Ti}_{50}\text{Ni}_{50-x}\text{Cu}_x$ alloys obtained by the Virtual Crystal Method.....	84
Table 4.4 Calculated charge transfer per atom in TiNiCu alloys.....	85
Table 4.5 Lattice parameters of, B19, B19' and BCO from earlier experimental and theoretical works.....	93
Table 4.6 Atomic coordinates of Ti and Ni/Cu in TiNiCu alloys ( $y = 0.25$ ) from VCM.....	94
Table 4.7 Atomic coordinates of Ti and Ni/Cu in TiNiCu alloys ( $y = 0.25$ ) from SM.....	94
Table 4.8 Atomic coordinates of Ti and Ni/Cu in TiNiCu alloys ( $y = 0.75$ ) from VCM.....	95
Table 4.9 Atomic coordinates of Ti and Ni/Cu in TiNiCu alloys ( $y = 0.75$ ) from SM.....	95
Table 4.10. Lattice parameters and free energy of TiNiCu alloys with Cu content exceeding 25 at% obtained by the Supercell Method.....	110
Table 4.11 Lattice parameters and free energy of TiNiCu alloys with Cu content exceeding 25 at% obtained by the Virtual Crystal Method.....	111
Table 4.12 Calculated charge transfer per atom in TiNiCu alloys with Cu content exceeding 25 at%.....	112
Table 4.13 Atomic coordinates of Ti and Ni/Cu in TiNiCu alloys with Cu content exceeding 25 at% ( $y = 0.25$ ) from VCM.....	114
Table 4.14 Atomic coordinates of Ti and Ni/Cu in TiNiCu alloys with Cu content exceeding 25 at% ( $y = 0.25$ ) from SM.....	115
Table 4.15 Atomic coordinates of Ti and Ni/Cu in TiNiCu alloys with Cu content exceeding 25 at% ( $y = 0.75$ ) from VCM.....	115
Table 4.16 Atomic coordinates of Ti and Ni/Cu in TiNiCu alloys with Cu content exceeding 25 at% ( $y = 0.75$ ) from VCM.....	116

---

---

# List of Abbreviations and Symbols

## Abbreviations

BCC	Body-centred Cubic
BCO	Base-centred Orthorhombic
BFGS	Broyden–Fletcher–Goldfarb–Shanno
CASTEP	Cambridge Serial Total Energy Package
DFT	Density Functional Theory
DOS	Density of States
GGA	Generalized Gradient Approximation
HF	Hartree-Fock
LDA	Local Density Approximation
MPA	Mulliken Population Analysis
MT	Martensitic Transformation
PBE	Perdew, Burke and Ernzerhof
PDOS	Partial Density of States
SCF	Self-consistent Field
SE	Superelasticity
SM	Supercell Method
SMA	Shape Memory Alloys
SME	Shape Memory Effect
VASP	Vienna ab initio Simulation Package
VCM	Virtual Crystal Method
VGC	Variable Geometry Chevron

---

## Symbols

$A_f$	Austenitic transformation finish temperature
$A_s$	Austenitic transformation start temperature
$E$	Total energy
$e_v$	Valence electrons
$E_{xc}$	Exchange-correlation energy
$\hbar$	Reduced Planck's constant
$\mathbf{H}$	Hamiltonian operator
$m$	Mass
$M_f$	Martensitic transformation finish temperature
$M_s$	Martensitic transformation start temperature
$\mathbf{p}$	Momentum
$\mathbf{T}$	Kinetic energy
$\mathbf{V}$	Potential energy
$\mathbf{v}$	Velocity
$\beta$	Monoclinic angle
$\sigma^{Af}$	Stress level of austenitic transformation completes
$\sigma^{As}$	Stress level of austenitic transformation initiates
$\sigma^{Mf}$	Stress level of martensitic transformation completes
$\sigma^{Ms}$	Stress level of martensitic transformation initiates

# Chapter 1 Introduction

## 1.1 Background of the research problem

Materials act as an important part in the history of human civilization. Among the innumerable material types, metal and alloy materials are indispensable for modern human existence. Ever since its discovery, shape memory alloys (SMAs), a kind of alloy that can remember the original shape and that when deformed returns to its pre-deformed shape when heated, have become a hot research topic, and have been widely applied, particularly in the biomedical, aerospace, robotic and automotive fields. Shape memory effect (SME), an unusual deformation behavior, is one of the most common and unique characteristics for the SMAs. The martensitic transformation (MT) is the underlying characteristic of the SME. Attributed to the SME, SMAs can generate much larger recovery strain and stress as compared to other “shape-changing” materials (such as piezoelectric materials etc.).

Shape memory alloy, or “smart alloy”, was first discovered in cadmium-gold alloys by Arne Ölander in 1932 [1]. Later in 1941, Vernon first described “shape-memory” for his polymeric dental material [2]. In 1951, the shape memory effect was observed by Chang and Read [3] in Au-47.5 at% Cd, which however did not attract much attention initially due to its high price. Subsequently, the shape memory effect became well known with its discovery



in an equiatomic TiNi alloy (also called Nitinol) by William Buehler and Frederick Wang at Naval Ordnance Laboratory in 1963 [4, 5].

Since its discovery, TiNi alloy has become one of the most commonly used materials in a wide spectrum of applications of SMAs. This is a result of the many desirable properties possessed by TiNi alloy, such as SME, superelasticity, good damping capacity, wear resistance, high strength and ductility as well as excellent biocompatibility [6-9]. One example of the successful applications is the TiNi eyeglass frame, which can exactly return to its original shape after deformation without damaging the frames due to its superelasticity.

Along with the extensive usage of TiNi alloy in various fields, the limitation presents gradually. In some cases, the applications are required to have narrow or wide transformation temperature hysteresis or to work at extreme temperatures. However, TiNi binary alloy cannot fulfill these requirements due to the constraint of the MT temperature. In order to change the transformation hysteresis and MT temperature, and to improve the physical and mechanical properties, various elements, such as Fe, Co, V, Cr, Al, Mn, Pt, Pd, Cu and Nb, have been added to TiNi binary alloy [10-30].

To date, many industries such as automotive and aerospace require SMAs possessing high response frequency characteristics. In order to meet this requirement, TiNiCu SMAs in which Cu substitutes for Ni, have been widely studied owing to their narrow MT temperature hysteresis in comparison with

TiNi binary alloy [31]. Recent research indicates that along with Cu added into TiNi alloy, the MT temperature remains stable but the MT pathway changes. With increasing Cu content in TiNiCu alloy, the transformation temperature hysteresis can be reduced to as low as 5K [32].

On the other hand, owing to the favorable superelasticity and biocompatibility, TiNi alloy has been widely used in biomedical fields. Although recent research has pointed out that pure Ni is a toxic element and causes Ni-hypersensitivity [33], the majority of biocompatibility studies suggest that TiNi alloy has low cytotoxicity (both in vitro and in vivo) as well as low genotoxicity [34]. The release of Ni ions depends on the surface state and the surface chemistry. Smooth surfaces with well-controlled structures and chemistries of the outermost protective TiO<sub>2</sub> layer lead to negligible release of Ni ions, with concentrations below the normal human daily intake [34].

However, the protective TiO<sub>2</sub> layer may be destroyed in some extreme conditions and this may result in releasing of Ni ions. In view of this concern, the research on Ni-free SMAs has been getting more and more traction in recent years. To tackle this issue, Cu substitution for Ni in an equiatomic TiNi alloy is an excellent choice as it can reduce Ni content, improve the superelasticity and also reduce the hysteresis of the superelasticity [29, 35, 36].

Currently, the research on SMAs is mainly explored experimentally. The inherent disadvantages for lab experiments are obvious. Firstly, it is time and resource consuming and sometimes, even challenging to fabricate the expected

materials due to technical hurdles. For example, Cu content exceeding 20 at% embrittles the TiNiCu alloy and adversely affects its formability. Only a few experimental investigations with the melt spinning process [37, 38], have been conducted to study the TiNiCu alloys with Cu content higher than 25 at% [39-41]. Moreover, the lab experiment is difficult to examine the characteristics of SMAs at atomic and/or electronic level, which is critical in establishing a holistic understanding of the underlying principle of the SME. Thus, a theoretical simulation and calculation is necessary to be carried out to solve these problems.

This study carries out three-pronged examines on SMAs at the atomic level, namely crystal structures, atomic displacements and charge transfers in the TiNiCu alloys in relation to the increasing of Cu content. The crystal structures and lattice constants of solids are of fundamental importance in determining the phase transformation, microstructural morphologies as well as other physical properties of SMAs [42]. A theoretical study on the changes of crystal structures of SMAs is indispensable to understand the shape memory effect and superelasticity thoroughly. Moreover, the study aims to further examine the atomic displacements which are the determinant for the crystal structures. Lastly, the study intends to unravel the charge transfers in the TiNiCu alloys, which is the mechanism behind the atomic displacements.

In summary, this research focuses on SMAs that have narrow hysteresis, specifically, TiNiCu SMAs with different Cu contents. Through the

computational approach, the crystal structures, electronic structures and atomic displacements of TiNiCu alloys with different Cu content will be studied and the effects of Cu content on crystal structures, electronic structures as well as atomic displacements will be examined in detail.

## **1.2 Objective and Scope**

To date, due to the aforementioned limitations of the experimental investigation, there is a lack of a holistic atomic level understanding of the relationship among the properties in TiNi-based SMAs, the crystal structures and the element content. The aim of the present research is to investigate the relationship between element content and crystal structures, electronic structures as well as atomic displacements of TiNi-based SMAs using a computational method, specifically in TiNiCu alloys. Success in this research will provide us an alternative method to examine the SMAs other than mass experiments and acts as a useful tool to predict the crystal structures of SMAs, which is instrumental for designing new desired SMAs owing specific properties.

In this research, the Cambridge Serial Total Energy Package (CASTEP) based on Density Functional Theory (DFT) is used to carry out all the calculations with plane-wave pseudo-potential. The numerical results were compared with reported experimental data to ensure their reliability. Furthermore, the total energies, density of states (DOS) and Mulliken

populations have been analyzed. Based on the computational results, the mechanism behind the change of crystal structures is established from a microstructure point of view. In view of specific applications, such understanding can provide a general guideline for designing new alloys with desired crystal structures without carrying out a large number of experiments.

The scope of this research is listed as follows:

### **(1) Structure Optimization of Equiatomic TiNi in Martensite**

The model of equiatomic TiNi martensite crystal structure is built based on experimental data. After the convergence test, the structure is optimized so as to obtain more stable structure. The calculated lattice constants are compared with existing experimental results to ensure the method and the basis set used in the calculations are reasonable.

### **(2) Martensite Crystal Structures in TiNiCu Alloys**

In order to design new SMAs possessing very small transformation temperature hysteresis, understanding the effect of alloying on martensite structures is of vital importance. In the present study, using the computational method, the effect of Cu content on the equilibrium structure of martensitic TiNiCu alloys is investigated. The lattice parameters  $a$ ,  $b$ ,  $c$  and the monoclinic angle are compared with experimental observations and a plausible prediction of the stable martensite crystal structures in TiNiCu alloys is proposed.

### **(3) Atomic Displacements in TiNiCu Alloys**

The change of crystal structures is generally governed by atomic displacement. Understanding the atomic displacement is of primary importance for studying the crystal structure transition resulting from alloying. In the present study, the atomic positions and displacements in martensite crystal structures of TiNiCu alloys are investigated through numerical calculations. The atomic positions of TiNiCu alloys with different Cu content are compared and the shifting of Ti and Ni/Cu atoms along all the directions are studied. Moreover, the rotation of the crystal plane has been analyzed and the mechanism behind the crystal structure transition is proposed.

### **(4) Charge Transfers in TiNiCu Alloys**

In order to establish a better understanding of the alloying effect on crystal structures as well as the shape memory and superelastic effects, the driving force for the atomic displacement in TiNiCu alloys is of crucial importance. However, little research has been done to explore the reasons behind the occurrence of such displacement. In the present study, the charge transfers and bond length between different atoms are calculated and the relationship between them is also investigated. In addition, a plausible explanation for the atomic displacement and crystal structure transition is proposed. Based on the computational results, the shape memory effect can be explained in detail and the relationship between crystal structure and electronic structure is established.

### 1.3 Organization of The Thesis

The thesis is presented as follows:

In the current chapter, Chapter 1, the history of shape memory alloys, TiNi-based shape memory alloys in particular, have been introduced. A framework of the studies on TiNi-based SMAs was also introduced.

Chapter 2 presents a literature survey of the shape memory alloys (especially TiNi-based shape memory alloys), shape memory effect, superelasticity as well as some basic concepts about phase transformations. Some earlier computational research results about TiNi-based SMAs are also introduced.

Chapter 3 provides basic information on the methods used to implement the first-principle calculations. In this chapter, the convergence test will be conducted and followed by the optimization of equiatomic TiNi martensite crystal structure.

In Chapter 4, the calculated results are presented and related discussions are conducted. Specifically, results on the effect of Cu content on the stable martensite crystal structures as well as the electronic structures of  $\text{Ti}_{50}\text{Ni}_{50-x}\text{Cu}_x$  ( $x = 0, 5, 12.5, 15, 18.75, 20, 25$ ) SMAs are presented and discussed; the atomic positions as well as their displacements in martensite crystal structures of  $\text{Ti}_{50}\text{Ni}_{50-x}\text{Cu}_x$  ( $x = 0, 5, 12.5, 15, 18.75, 20, 25$ ) SMAs are presented and the relationship between such displacements and the stable martensite structures are discussed; the results of lattice properties of  $\text{Ti}_{50}\text{Ni}_{50-x}\text{Cu}_x$  ( $x = 25, 30, 35, 37.5,$

40, 45, 50) alloys are presented and the relationship between the charge transfer and the lattice properties is discussed.

Finally, the conclusions were drawn in Chapter 5 and some suggested future works are proposed.



# **Chapter 2 Literature Review on TiNi-based SMAs**

In this chapter, a literature survey of SMAs, especially TiNi-based SMAs, including shape memory effect, two-way memory effect, superelasticity as well as the applications, are presented. Furthermore, the martensitic phase transformation, transformation paths and the crystal structures in TiNi-based SMAs are reviewed. Lastly, particular attention is paid to the recent computational progress in TiNi-based SMAs.

## **2.1 Shape Memory Alloys and Related Phenomena**

### **2.1.1 Shape Memory Alloys**

Shape memory alloys (SMAs) are often referred to as smart materials. The two main characteristics of SMAs are shape memory effect (SME) and superelasticity (SE). SMAs are the group of alloys which are able to remember their original shape and can recover to that shape upon heating even after being highly deformed. This phenomenon is called the SME. At above a critical temperature, SMAs can return to the original shape upon unloading after a substantial deformation. This phenomenon is called superelasticity, which is also sometimes termed pseudoelasticity [43].

There are two main classes of SMAs developed as smart materials in recent decades. One is the traditional SMAs such as TiNi, CuAlNi, TiNiCu, etc., in

which the SME is induced by temperature or stress. The other is ferromagnetic SMAs like NiMnGa, FePt, FePb, etc., in which the actuation energy for SME is transmitted via magnetic fields [44-48]. In the present research, particular attention is given to the traditional SMAs, specifically, TiNi-based SMAs.

### 2.1.2 TiNi-based Shape Memory Alloys

TiNi-based SMAs have been studied extensively due to their highest number of commercial applications in various fields, such as biomedical, automotive and aerospace industries. These applications exploit mainly two unique properties: shape memory effect and superelasticity which are caused by martensitic transformation (MT).

The phase diagram of the TiNi alloy system is of vital importance for understanding and improving the shape memory characteristics, and Figure 2.1 shows the phase diagram of the TiNi alloy system [49]. Our interests are restricted to the central region since only equiatomic or nearly equiatomic TiNi alloys possess the shape memory effect.

Like all other metals and alloys, TiNi-based SMAs have more than one crystal structure, which is known as polymorphism. The prevailing crystal structure or phase for TiNi-based SMAs mainly depends on both temperature and external stress. For equiatomic TiNi, it has different phases under different conditions. At high temperature the austenite phase presents, and upon cooling

the martensite phase occurs due to the martensitic transformation. This transformation is reversible when temperature increases.

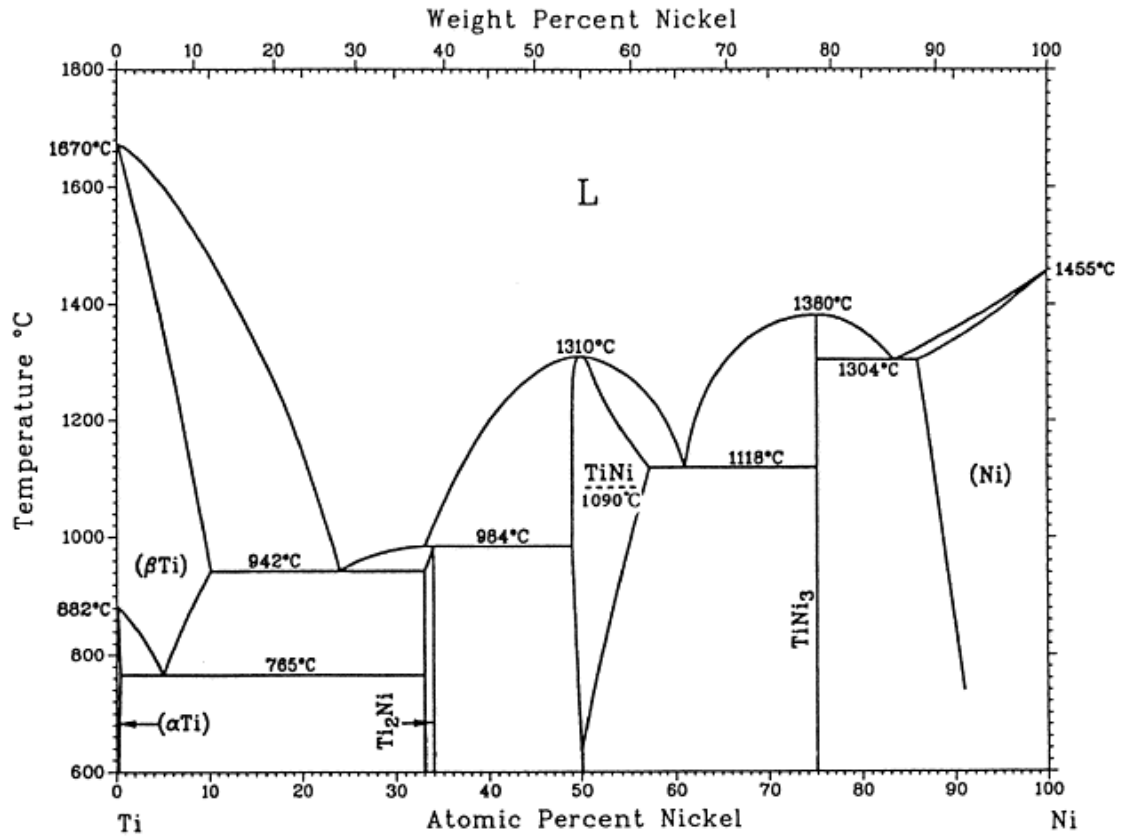


Figure 2.1 Phase diagram of TiNi alloy [49].

Figure 2.2 shows a typical Differential Scanning Calorimeter (DSC) curve of TiNi Shape Memory Alloy. A set of characteristic temperature of transformation are as follows:  $M_s$  is martensitic transformation start temperature upon cooling;  $M_f$  is martensitic transformation finish temperature upon cooling;  $A_s$  is austenitic transformation start temperature upon heating and  $A_f$  is austenitic transformation finish temperature upon heating.

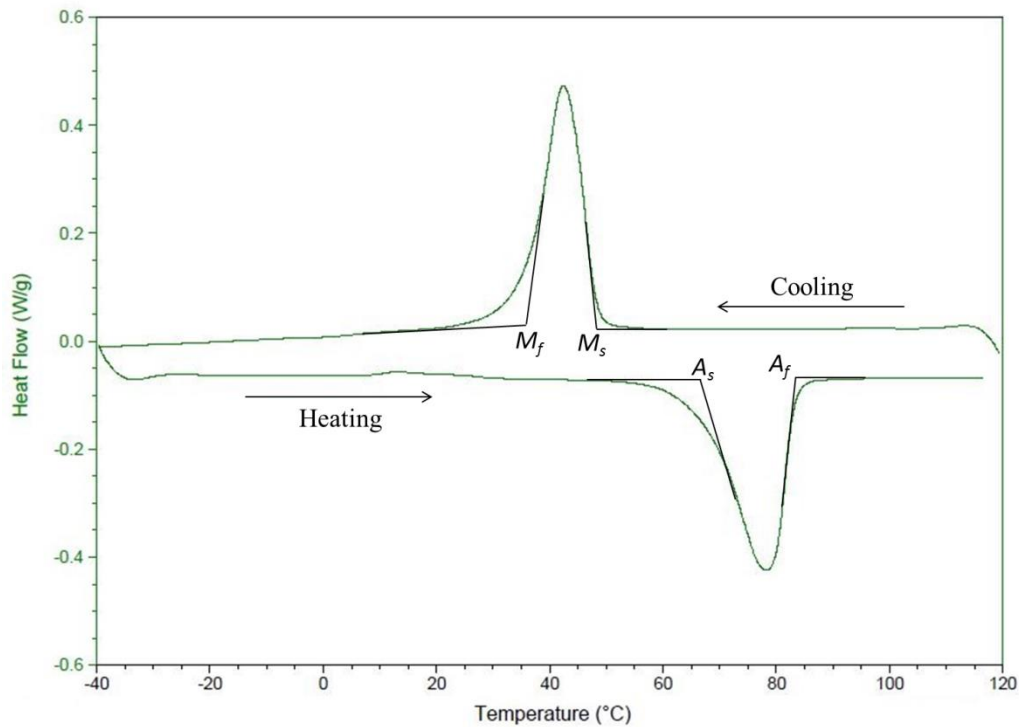


Figure 2.2 A Typical DSC Curve of TiNi Shape Memory Alloy

Martensite phase starts to form when temperature drops below  $M_s$  and completes transformation when temperature drops below  $M_f$ . Austenite phase does the opposite and starts to form when the temperature is raised up to  $A_s$  and finishes transformation when temperature is above  $A_f$ . However, there is a gap between  $M_s$  and  $A_f$ , and this is called hysteresis. That is to say, the temperature range from the martensite to austenite transformation which takes place upon heating is higher than that for the reverse transformation upon cooling. The difference between these two temperatures upon heating and cooling is termed the hysteresis. Generally, the hysteresis is defined as the difference between the temperatures at which the material is 50% transformed to austenite upon heating and 50% transformed to martensite upon cooling [50].

In TiNi binary alloy, the content of nickel or titanium has a strong influence on the  $M_s$ . Alloys with greater than 51 at% nickel are quite brittle in the unaged condition. Aging depletes the TiNi matrix of nickel, thus restoring ductility but of course increasing the transformation temperature as well [51, 52]. In order to achieve a specific transformation temperature, their relative concentrations should be controlled. The relationship between nickel content in binary TiNi alloy and  $M_s$  temperature is shown in Figure 2.3.

With increasing nickel content, the  $M_s$  temperature is lowered. In particular, for nickel rich TiNi SMAs, the  $M_s$  temperature reduces drastically with slight increase in nickel content. On the other hand, for titanium rich TiNi SMAs, this temperature is more stable, which can reach up to 300 °C, but these usually have poor thermal conductivities [51, 52].

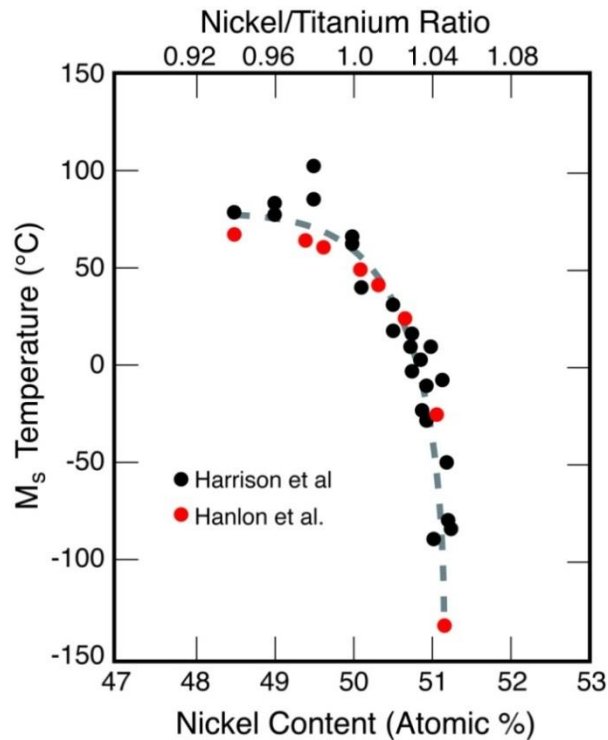


Figure 2.3 Relationship between nickel content and transformation start temperature [51].

It is not easy to change the MT temperatures by controlling the content of nickel or titanium because the shape memory effect presents only for a narrow range of nickel composition of 50 atomic percent. In order to control the MT temperatures more effectively and also to improve the mechanical and physical properties, a third element is usually used to partially substitute nickel or titanium in the TiNi binary alloy.

In order to lower the transformation temperatures, Fe, Co, V, Cr, Al, and Mn could be substituted in small quantities for nickel without seriously impairing the shape memory effect [10-14]. In addition, Pt and Pd could be used to form the alloys Ti-Pt-Ni and Ti-Pd-Ni to increase transformation temperatures beyond 600 °C [15-20]. TiNiNb alloys were developed due to its wide MT temperature hysteresis which can be over 70 °C [21-25]. The addition of Cu does not significantly change the MT temperatures, but with increasing Cu content, the MT type would change to that with a narrow MT temperature hysteresis [26-30].

### 2.1.3 Shape Memory Effect

The shape memory effect (SME) is a unique property of certain alloys exhibiting martensite transformation. The alloy can recover its original shape by reverse transformation upon heating to a critical temperature called the reverse transformation temperature even though it is deformed in a low temperature phase [53-55].

### 2.1.3.1 Mechanism of Shape Memory Effect

Martensitic phase transformation plays a substantial role in shape memory effect. When nickel and titanium atoms are in one alloy, in a given proportion, it forms a crystal structure, which is able to undergo a change from one form of crystal structure to another. The transformation from one form of crystalline structure to another creates the mechanism by which the shape change occurs in SMAs. For TiNi, this kind of change involves transition between a monoclinic crystal structure (martensite) and a body centred cubic crystal structure (austenite). The martensite structure is stable at lower temperatures, and the austenite phase is stable at higher temperatures.

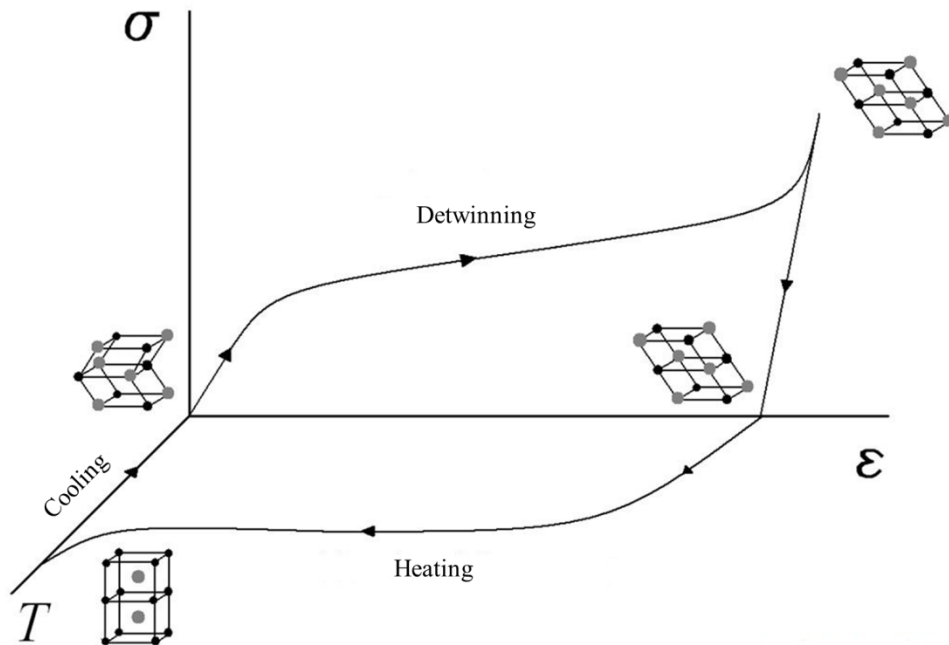


Figure 2.4 Schematic of a stress-strain-temperature curve showing the shape memory effect [56].

In the martensite phase, the martensite twins are able to flip their orientation, in a simple shearing motion, to the opposite tilt, creating a cooperative movement of individual twins. As shown in Figure 2.4, the SMA is in its twinned martensite form when the temperature is below  $M_f$  upon cooling. While loading, the twinned martensite undergoes typical elastic deformation and then detwinning initiates. Upon unloading, the phase changes to the high temperature austenite phase by heating the material above  $A_f$ . Upon cooling, the structure returns to the original twinned martensite form [56]. For ordinary metals, they cannot reverse the initial shape once deformation occurs by dislocation motion and atomic planes sliding over another, which takes on a new crystal position, and this results in permanent damage to the crystalline order. Distinct from these ordinary metals, SMAs deform by detwinning which just changes the tilt orientation of twins and does not cause any dislocation. Detwinning allows the martensite phase to absorb dislocation to a given extent. Shape recovery only occurs from detwinning, but not to a deformation process involving slip which is irreversible [57].

From the crystallographic viewpoint, twinning and detwinning are important microstructure processes partially responsible for the shape memory effect because the deformation associated with detwinning is recoverable. A lot of reported research results show that there are various twinning modes frequently observed in TiNi-based shape memory alloys. There are  $\{1\ 1\ 1\}$  Type I twinning and  $\langle 0\ 1\ 1 \rangle$  Type II twinning, etc., in B19' martensite [58, 59].



In B19 martensite, there are two twinning modes:  $\{1\ 1\ 1\}$  Type I and  $\{0\ 1\ 1\}$  compound twins [60, 61], which are both associated with small twinning shears. There are also two types of twinning modes in the R-phase [58-62].

### 2.1.3.2 One-way Shape Memory Effect

The procedure and theory of one-way shape memory effect can be explained using a simplified model proposed by Otsuka as shown Figure 2.5 [63]. The exact processes and underlying principles are of course much more complicated.

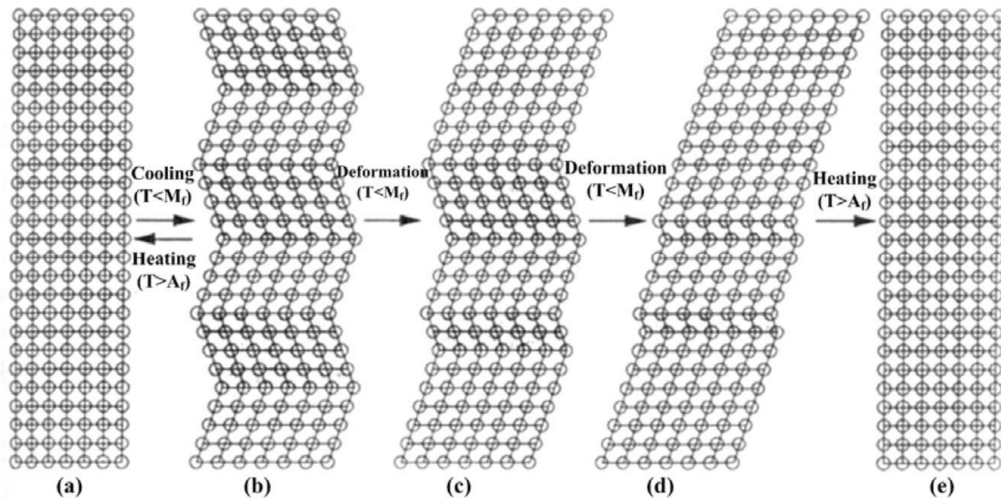


Figure 2.5 Mechanism of shape memory effect: (a) original parent single crystal, (b) self-accommodated martensite, (c-d) deformation of martensite proceeds by the growth of one variant at the expense of the other, (e) upon heating to a temperature above  $A_s$ , each variant reverts to the parent phase in the original orientation by the reverse transformation [63].

It is known that the austenite structure is formed at high temperature. It transforms to twinned martensite structure upon cooling. During this process, the shape of the sample does not change. When external stress is applied, detwinning will occur and the twinned martensite structure will reorient certain

numbers of variants after a typical elastic deformation. If the load applied is sufficiently high, the twinned martensite structure could transform to detwinned martensite structure which means the variants present in twinned structure could transform to a single variant. When the ambient temperature is above the austenite finish temperature  $A_f$ , detwinned martensite structure will again transform to austenite structure by which the shape memory effect occurs.

#### 2.1.3.3 Two-way Shape Memory Effect

SMAAs can recover their original shape upon heating after being deformed in a relatively low temperature and the shape memory effect that exists only in the heating process is called a one-way shape memory effect as stated above. However, some shape memory alloys can recover the shape of high temperature phase by heating and can also restore the shape of low temperature phase by cooling. This behavior is known as the two-way shape memory effect. As shown in Figure 2.5, it is quite easy to understand the one-way shape memory effect. The shape remains the same when SMAAs cool down from high temperature austenite phase and the shape changes when a stress is applied on SMAAs at low temperature martensite phase. It will then recover to the original shape before deformation by heating to a temperature over  $A_f$ . While cooling down again to below the  $M_f$ , this shape will not change.

It is also possible in some of SMAAs to possess two-way shape memory ability in which the shape change occurs upon both heating and cooling. However, the amount of the shape change for two-way shape memory is always

significantly less than the change obtained with one-way shape memory [64-66].

As shown in Figure 2.6, two-way shape memory effect is such that the SMAs are able to return to a low temperature shape upon cooling as well as to a high temperature shape on heating. However, during cooling with the two-way shape memory effect, the material simply recovers its low temperature shape but the force able to be exerted against a load is relatively weak [67, 68]. Without the external force, it is difficult to completely recover the original shape for two-way shape memory alloys. In this sense, two-way shape memory effect is not as reliable as one-way shape memory effect.

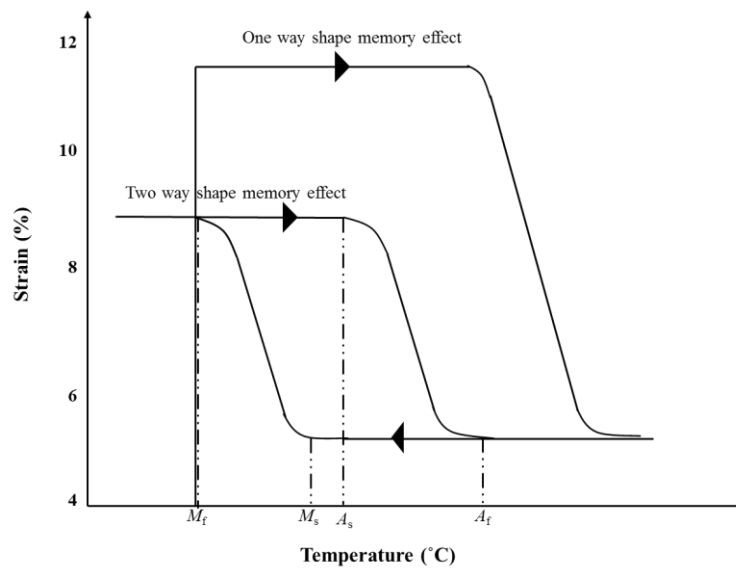


Figure 2.6 Illustration of two-way shape memory effect.

Two-way shape memory effect is a result of some special thermomechanical treatments, called training. In fact, the training processes

involve the repetition of thermomechanical cycles. Following this, the alloys can repeat two new shapes continuously by heating and cooling. The two new shapes are a little different from either the original shape in high temperature austenite phase or the shape just after training [69, 70].

#### 2.1.4 Superelasticity

At a temperature above  $A_f$ , when the alloys are subjected to a loading lower than the critical slip stress, they can restore directly to the original shape simply by unloading. This phenomenon is known as the superelasticity effect, which is also sometimes called pseudoelasticity.

The superelastic effect of SMAs is characterized by the remarkable amount of possible “elastic” strain, which is more than 20 times higher compared to conventional materials. Thus, it is called “superelasticity” or “pseudoelasticity”.

SMAs in the austenite phase exhibit a highly elastic behavior. This allows the material to deform up to 7% and then fully recover the resulting strain by simply removing the load. Deformed superelastic material is in the formation of martensite crystal, and it is called stress-induced martensite. In fact, the superelasticity is prompted by stress-induced martensitic transformation. The process of superelasticity can be observed in Figure 2.7 [56]. The stress levels at which the martensite transformation initiates and completes are denoted by  $\sigma^{Ms}$  and  $\sigma^{Mf}$ , respectively. Similarly, as the SMA is unloaded, the stress levels at

which the material starts and finishes its reverse transformation to austenite are denoted by  $\sigma^{As}$  and  $\sigma^{Af}$ , respectively.

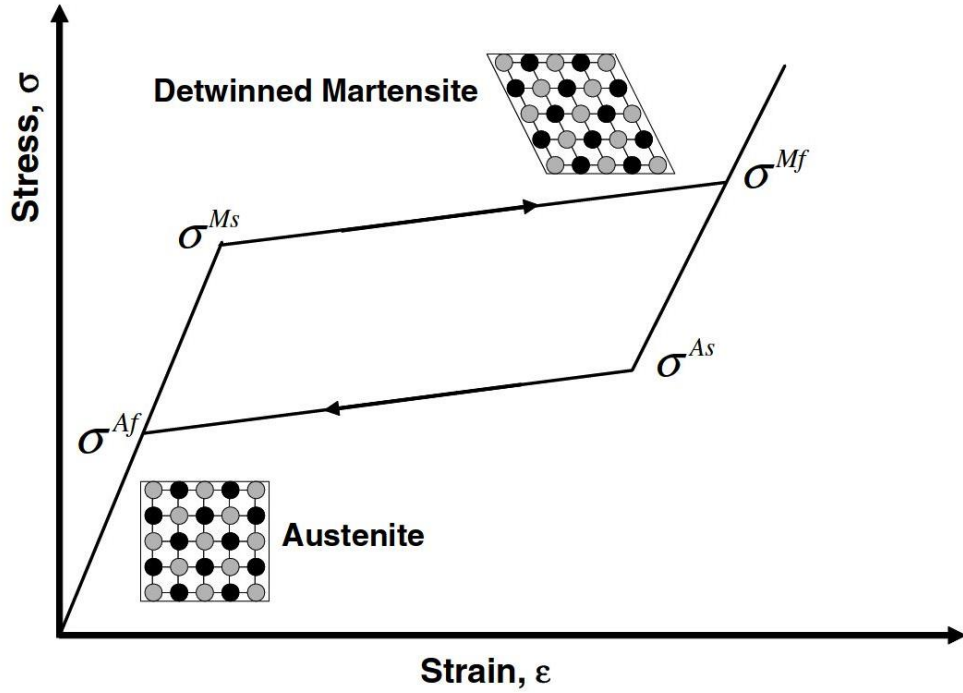


Figure 2.7 Schematic of a superelastic stress-strain diagram [56].

In the high temperature austenite phase, the martensitic transformation occurs upon loading. There will be a plastic deformation if the loading is beyond the critical stress for dislocation slip. The reverse transformation occurs subsequently by unloading and the large deformation can be recovered by which the superelasticity presents [71-74]. In superelasticity, temperature changes are not necessary for its occurrence. However, if the material in the austenitic phase is tested above the  $A_s$  temperature, but below the  $A_f$  temperature, only partial shape recovery is observed [56].

### 2.1.5 Application of Shape Memory Alloys

SMAAs are widely used for their special shape memory and superelasticity effects. TiNi-based alloys are one kind of SMAAs which has achieved the level of commercial exploitation. The TiNi-based alloys have high shape memory strain which is up to 8% and tend to be more thermally stable than other SMAAs. In addition, the TiNi-based alloys have excellent corrosion resistance and low susceptibility to stress-corrosion cracking, and also possess high ductility. The basis of TiNi-based alloys is the binary TiNi alloy, which is an equiatomic intermetallic compound. Since the TiNi intermetallic compound has moderate solubility range for excess nickel or titanium, as well as most other metallic elements, it allows alloying with many other elements to improve both mechanical properties and transformation properties.

For SMAAs, the motion and force can be generated by SME. Thus, shape memory components can be designed to exert force over a considerable range of motion, often for many cycles. On the other hand, the superelasticity of SMAAs can be applied to store deformation energy. According to the primary function, the shape memory applications generally can be divided in four categories, which are automotive applications, aerospace applications, robotic applications and biomedical applications [75].

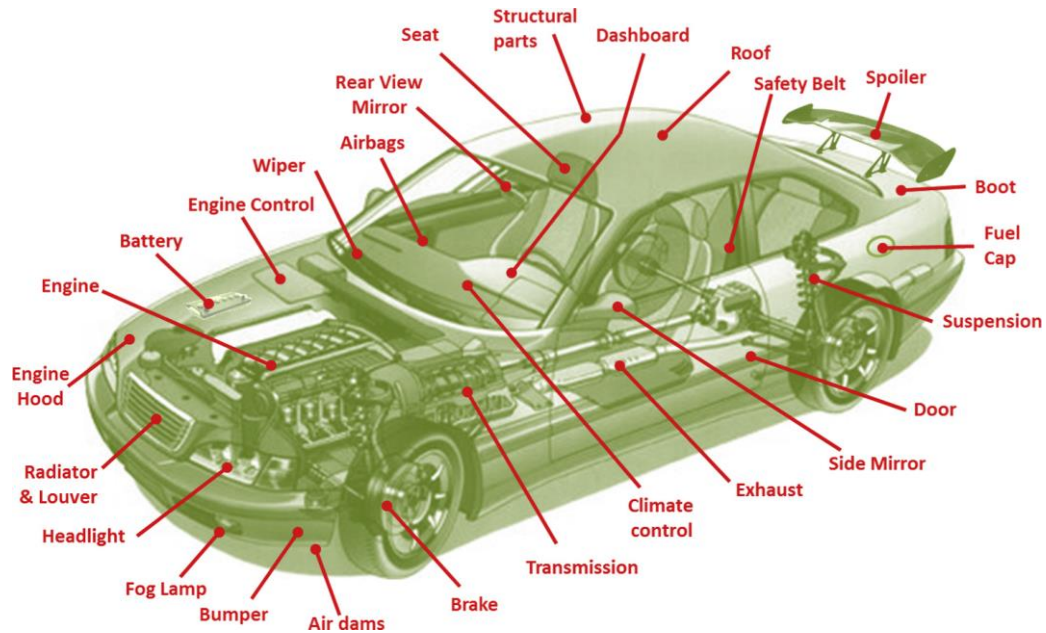


Figure 2.8 Applications of shape memory component in automotive [76-78].

To date, in order to fulfill the requirement for safer and more comfortable vehicles, as shown in Figure 2.8, an increasing number of actuators and sensors are used. In these applications, the SMA component is used to open a spring or press a button when it is heated. Upon cooling, the SMA actuator becomes weaker and the “springback” easily deforms the actuator [76-80].

In the 1970s, since its successful application in F-14 fighter jets, SMAs have attracted more and more interest in aerospace applications [81-85]. Recently, Boeing has developed a variable geometry chevron (VGC) which is an active serrated aerodynamic device. As shown in Figure 2.9, it has been proved that by maximizing the chevron deflection, the VGC can effectively reduce the noise when taking-off and by minimizing the chevron deflection, it can improve fuel economy when cruising at a high altitude [86-88].

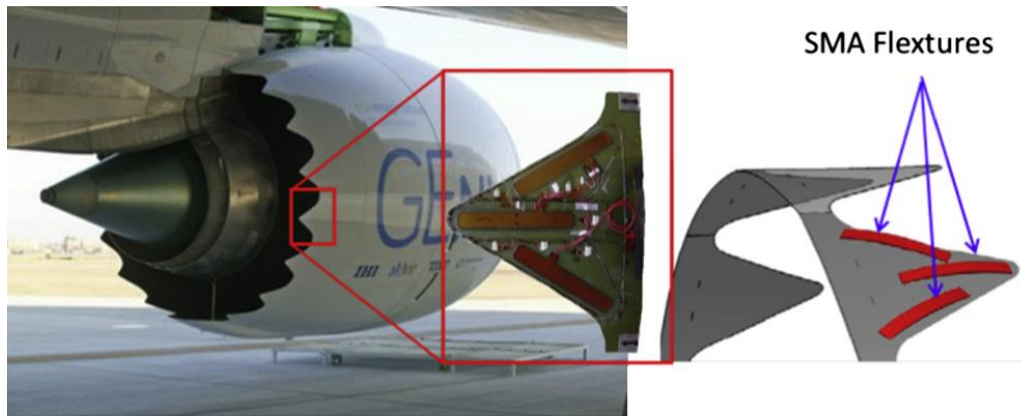


Figure 2.9 The variable geometry chevron developed by Boeing [88].

Large-scale application of SMAs in commercial robotic systems started from the 1980s which mostly focus on the micro-actuators and artificial muscles [89-95]. To date, more and more robotic applications are biological inspired and also widely used in biomedical fields, in which SMAs are playing an increasingly important role [96-98].

Furthermore, the excellent corrosion resistance [99, 100] and biocompatibility characteristics [101, 102] of TiNi-based alloys make them ideal for biomedical applications. The material can be fabricated into the very small sizes often required. They are widely used in the areas of dentistry, orthopedic surgery, operation devices, etc. [103-105] As shown in Figure 2.10, this is an example of a biomedical application of SMAs for the correction of severe rigid scoliosis [106].



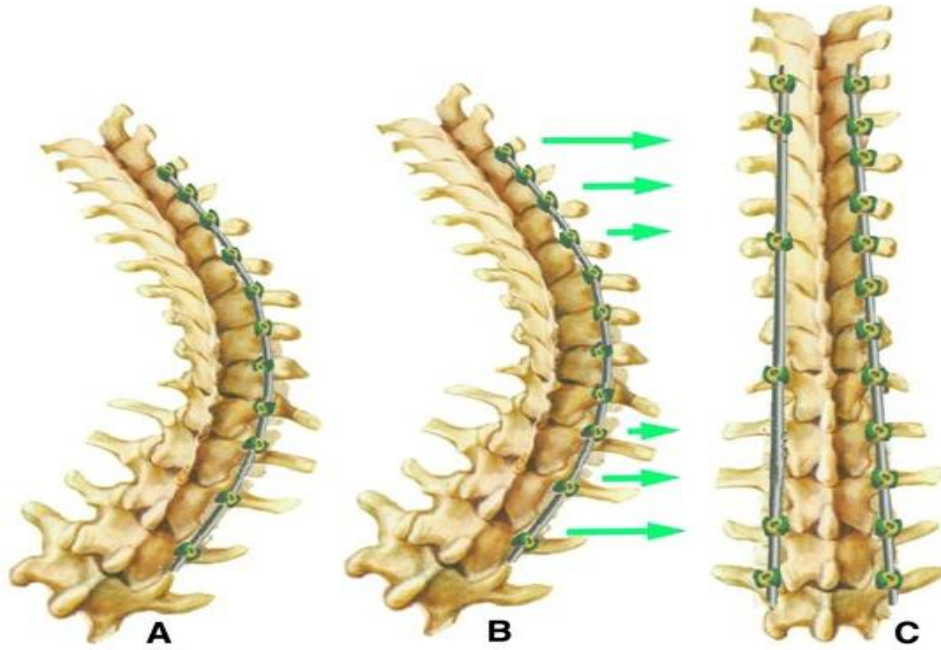


Figure 2.10 Example of biomedical application of SMAs [106].

At present, most interesting applications of the superelastic effect can be found in medical implants and instrumentations. For example, SMAs have recently been used as stents for thin-walled tubing. Due to its high elasticity, the stents can be folded into catheters and pushed into the vessel, where they can expand and provide a force to keep the vessel open [107].

## 2.2 Phase Transformations in TiNi-based SMAs

There are two types of phase transformations in solid state which are diffusional and displacive. Martensitic transformation (MT) belongs to the latter. The MT from austenite to martensite and its reverse transformation are lattice transformations involving a shearing deformation that results from cooperative atomic movements. It is a diffusionless first order phase transformation in the solid state, which proceeds by the nucleation and growth of the new phase [108-110].

The unique behavior of TiNi-based SMAs is based on the temperature dependent austenite-to-martensite phase transformation on an atomic scale, which is also called thermoelastic martensite phase transformation. During thermoelastic martensite transformation, the crystal lattice structure needs to accommodate to the minimum energy state.

The diffusionless martensitic transformation is a significant reason for the shape memory effect. Thus it is important to understand the manner in which the coordinated movement of atoms occurs during the phase transformation.

### 2.2.1 Crystal Structures in TiNi-based SMAs

Generally speaking, the austenite phase of TiNi-based SMAs is the parent phase with a cubic structure while the martensite phase has a monoclinic, orthorhombic or trigonal structure. In TiNi-based alloys, there are usually four phases observed. The B2 phase is the austenite phase or parent phase with a cubic structure, while the B19, B19' and R phases are the martensite phases with orthorhombic, monoclinic and trigonal structures, respectively.

The crystal structures of TiNi-based alloys in the austenite B2 phase and in the martensite B19' phase are as shown in Figure 2.11. In this figure, nickel atoms are in blue color while titanium atoms are gray. In the martensite transformation of TiNi-based alloys, the crystal structure transforms from high temperature B2 phase to low temperature B19' phase. In this process, the

composition of TiNi-based alloys remains the same but the crystal structure changes [43, 111-114].

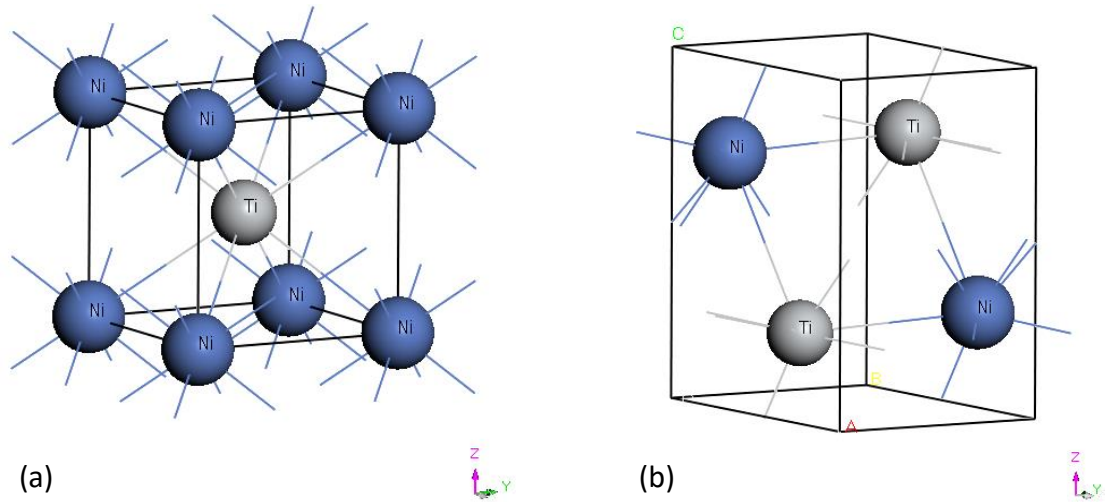


Figure 2.11 Crystal structure of TiNi alloys (a) in austenite B2 phase (b) in martensite B19' phase.

For TiNi-based alloys, the austenite phase or parent phase at high temperature is B2 which has a body-centred cubic (BCC) lattice. The lattice parameter is  $a_0 = 3.015 \text{ \AA}$ . The B19' crystal structure is obtained when binary TiNi alloy is quenched from high temperature after solution-treatment. The crystal structure of the B19' martensite was first reported as hexagonal by Purdy and Parr [115] in 1961. Then Dautovich and Purdy [116] reported it to be triclinic with lattice parameters  $a = 0.460 \text{ nm}$ ,  $b = 0.286 \text{ nm}$ ,  $c = 0.411 \text{ nm}$ ,  $\alpha = 90.1^\circ$ ,  $\beta = 90.9^\circ$ ,  $\gamma = 96.7^\circ$  by using electron diffraction and X-ray powder diffraction methods. Thus far, the structure of B19' martensite is established as

monoclinic with lattice parameters  $a = 2.885 \text{ \AA}$ ,  $b = 4.12 \text{ \AA}$ ,  $c = 4.622 \text{ \AA}$  and  $\beta = 96.8^\circ$  [117].

For the crystal structure of B19 martensite, it is more straightforward to be established. The crystal structure of B19 martensite has been established as orthorhombic and the lattice parameters are  $a = 2.88 \text{ \AA}$ ,  $b = 4.28 \text{ \AA}$ ,  $c = 4.52 \text{ \AA}$ . It is essentially the same as the structure of  $\gamma'2$  martensite in Au-47.5Cd and  $\gamma'1$  martensite in Cu-Al-Ni alloy [71].

The so-called R-phase appears as an intermediate phase under certain conditions during the martensitic transformation. The R-phase was clearly observed by electron microscopy and it has been earlier reported to be tetragonal in structure [118], but recently Schryvers and Potapov [119] re-examined the structure of the R-phase by using electron diffraction patterns from single crystalline areas in the R-phase. It was then proposed that the crystal structure of the R-phase should be trigonal.

In TiNi-based SMAs, the crystal structure of martensite is relatively less symmetric compared to that of the austenite phase. When a single crystal of the parent phase is cooled to below  $M_f$ , the martensite variants with a total of 24 crystallographically equivalent habit planes are generally created. However, only one possible parent phase orientation exists, and all martensite configurations revert to that single defined structure and shape upon heating to above  $A_f$ . The mechanism by which the martensite variants deform is called twinning, and it can be described as a mirror symmetry displacement of atoms

across a particular atom plane, namely the twinning plane. Unlike most metals, which deform by dislocation or slip, TiNi-based SMAs respond to stress by simply changing the orientation of its crystal structure through the movement of twin boundaries.

The phase transformation is a thermo-mechanical process which means the martensitic transformation can be induced by temperature change as well as applied stress. Recent research shows that magnetic field can also lead to diffusionless martensitic transformation, which however will not be discussed in this thesis.

### 2.2.2 Temperature-induced Martensitic Transformation

Generally, the temperature-induced martensitic transformation is of primary importance for the shape memory effect. The driving force for this martensitic transformation is the changing of Gibbs free energy of the parent and martensite phases with respect to temperature. The crystal structures always tend to minimize the total free energy towards a more stable state.

Figure 2.12 shows the phase transformation versus temperature curve. By heating TiNi-based SMAs, austenite begins to form when temperature reaches  $A_s$  and this transformation process is completed at  $A_f$ . In the cooling process, martensite starts to form at  $M_s$  and completes at  $M_f$ .

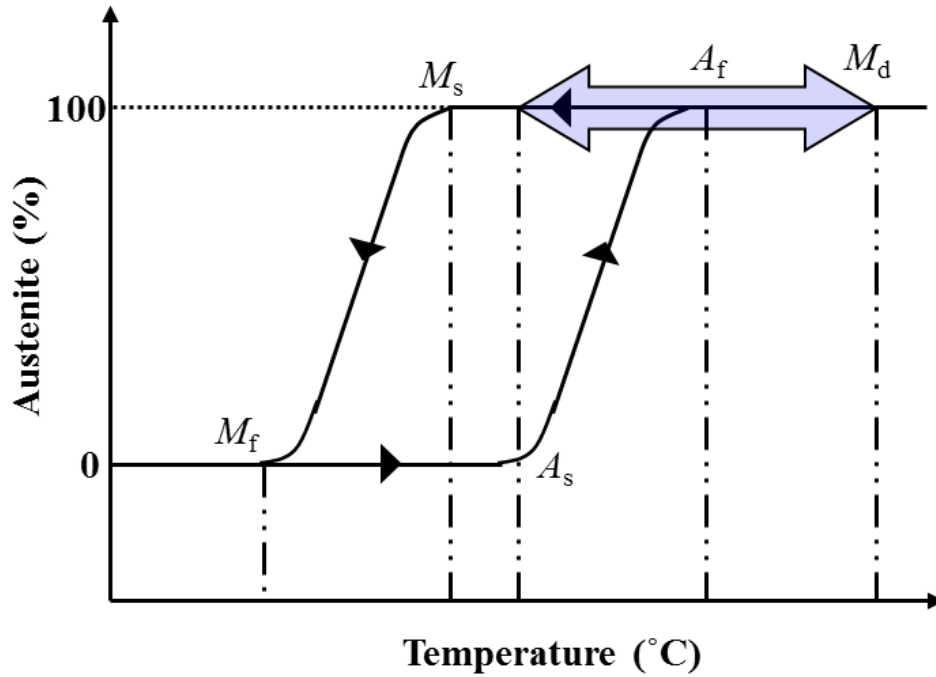


Figure 2.12 Phase transformation versus temperature curve.

### 2.2.3 Stress-induced Martensitic Transformation

Generally, the stress-induced martensitic transformation is the mechanism for superelasticity. As shown in Figure 2.12, the area between  $A_s$  and  $M_d$  is the transformational pseudoelasticity temperature range. In the process of stress-induced martensitic transformation, strains and deformations can be caused by applied loads to the materials. As a result, the free energy of the system will increase. As the system always tends towards minimizing the free energy, the transformation is induced.  $M_d$  is a critical temperature, above which the critical stress for inducing martensitic transformation is greater than that needed to cause plastic deformation. In this case, the dislocation would occur rather than transformation. As a result, the stress-induced martensitic

transformation would no longer exist. Thus  $M_d$  is the highest temperature for a certain shape memory alloy to have stress-induced martensitic transformation.

## 2.3 Transformation Paths in TiNi-based SMAs

There are three distinct types of martensitic transformations in TiNi-based alloys: B2-B19' transformation, B2-R-B19' transformation and B2-B19-B19' transformation. With different elements added in TiNi alloy or different treatment methods, the transformation paths from austenite phase to martensite phase can be quite different. Three transformation paths in TiNi-based alloys are shown in Figure 2.13.

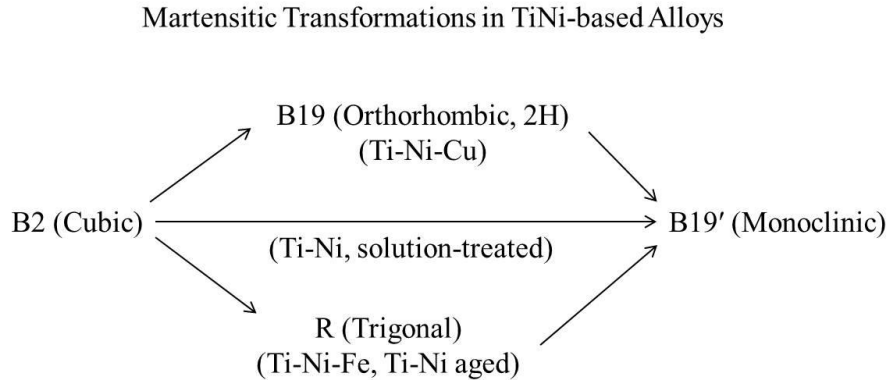


Figure 2.13 Three transformation paths in TiNi-based alloys [71].

From this figure, the martensitic transformation occurs from B2 to B19' directly for the solution-treated binary TiNi alloy. B19 orthorhombic structure may present when Cu atoms substitute for specific Ni atoms in TiNi alloy during the martensitic transformation. With Fe added in TiNi alloy, the R phase may occur as an intermediate phase. However, the intermediate phases are difficult to observe because they exist for just a short time [71, 120].

Annealed near-equiatomic TiNi alloy transforms from the B2 parent phase directly to the monoclinic B19' phase, while thermally cycled or thermo-mechanically treated near-equiatomic TiNi alloy transforms in two steps, from the B2 phase to the R-phase and then to the B19' phase [71]. In these two steps, the crystallography of the B2 phase to R-phase transformation, generally, can easily be observed. However the crystallography of R-phase to the B19' phase is not so clear. More extensive work on the R-phase to B19' phase transformation is currently still being carried out using the electron diffraction technique [71].

The B2-B19-B19' successive transformation has been studied by Fukuda et al. [120] using X-ray diffraction method for  $\text{Ti}_{49.5}\text{Ni}_{45.5}\text{Cu}_{5.0}$ . The recent research shows that the two successive transformations occur in the similar temperature range with overlapping. The effect of the former transformation reflects strongly on electrical resistivity which leads to resistivity increase with lowering temperature. The electrical resistivity and temperature curves of the three martensitic transformations are shown in Figure 2.14.



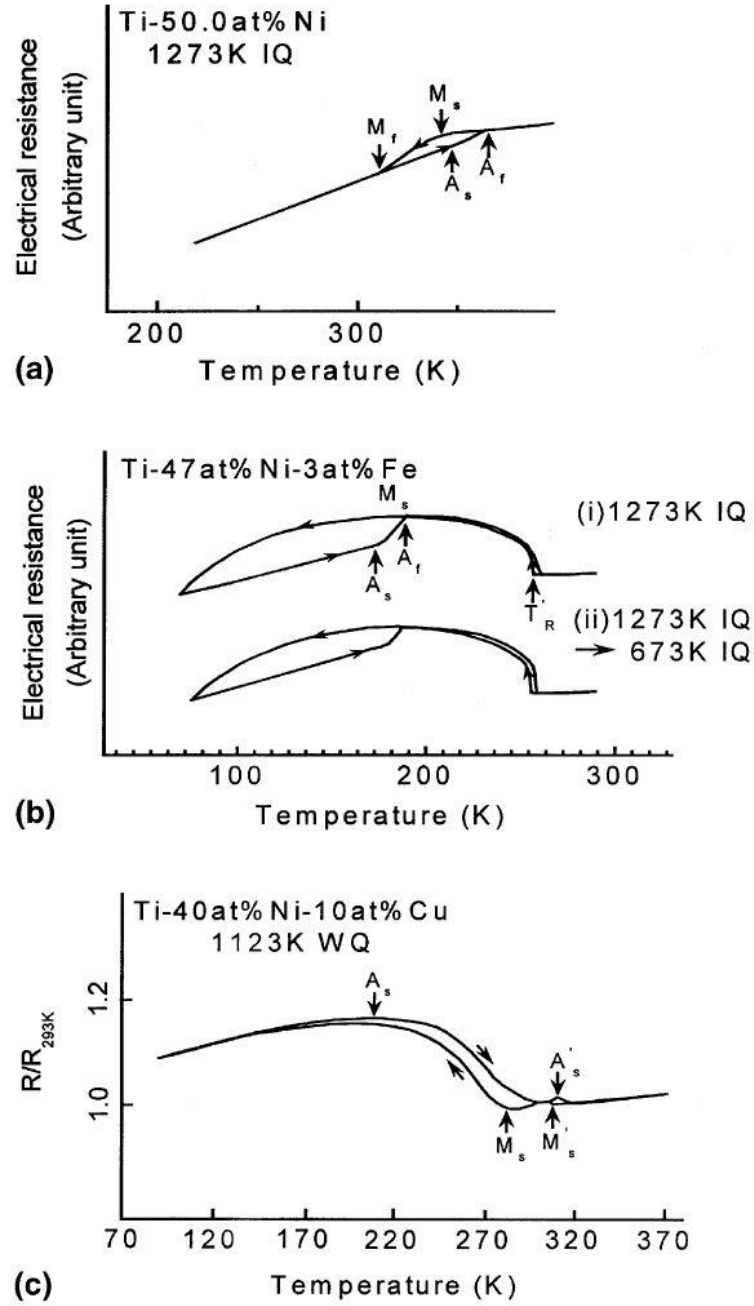


Figure 2.14 Electrical resistivity and temperature curves for the three martensitic transformations in TiNi-based alloys: (a) B2-B19' transformation; (b) B2-R-B19' transformation; (c) B2-B19-B19' transformation [71].

In this figure,  $M_s$  is the martensitic transformation start temperature from B2;  $M_f$  is the martensitic transformation finish temperature;  $A_s$  is the reverse martensitic transformation start temperature and  $A_f$  is the reverse martensitic

transformation finish temperature.  $T'_R$  represents R-phase transformation start temperature,  $M'_s$  the transformation start temperature of B19 and  $A'_s$  the reverse transformation start temperature of B19.

This figure shows that if some other metals such as Cu or Fe are added to TiNi, the martensitic phase transformation path will be changed. Also, the gap between  $M_f$  and  $A_s$  will be changed.

As mentioned in Section 2.2, the martensitic transformation can be induced by both temperature and applied stress. Moreover, the alloying process is also able to affect the martensitic transformation. In this thesis, we will focus on the TiNiCu alloys which are obtained by using Cu elements to partially substitute Ni in TiNi binary alloy.

As shown in Figure 2.15, there are different types of martensitic transformation with varying Cu content. In this figure,  $M'_s$  is the transformation start temperature from B2 phase to B19 phase and  $M_s$  the transformation start temperature from B2 phase to B19' phase.

The relationship among the three phases B2, B19 and B19' of TiNiCu alloys is also presented in Figure 2.15. From this figure, it is evident that  $M'_s$  increases slightly with increasing Cu content while  $M_s$  reduces significantly. Therefore, the transformation temperature from B2 to B19 is more stable with increasing Cu content [121].

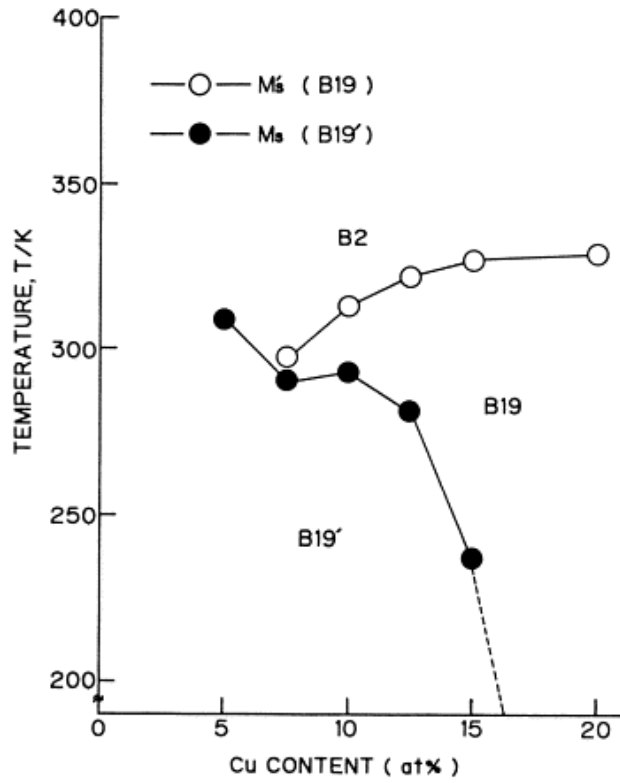


Figure 2.15 Effect of Cu content on transformation temperatures of TiNiCu alloys [121].

From Figure 2.16, which shows different levels of Cu substitutes for Ni in TiNi binary alloy, it is observed that there is little appreciable change in the transformation temperature and all the new alloys generally have a narrow temperature hysteresis. However, the transformation pathway changes significantly for different Cu content. For  $\text{Cu} \leq 7.5 \text{ at\%}$ ,  $\text{B2} \rightarrow \text{B19'}$  transformation occurs; for  $7.5 \text{ at\%} < \text{Cu} \leq 15 \text{ at\%}$ ,  $\text{B2} \rightarrow \text{B19} \rightarrow \text{B19'}$  transformation will take place and for  $\text{Cu} \geq 15 \text{ at\%}$ , it is a  $\text{B2} \rightarrow \text{B19}$  transformation.

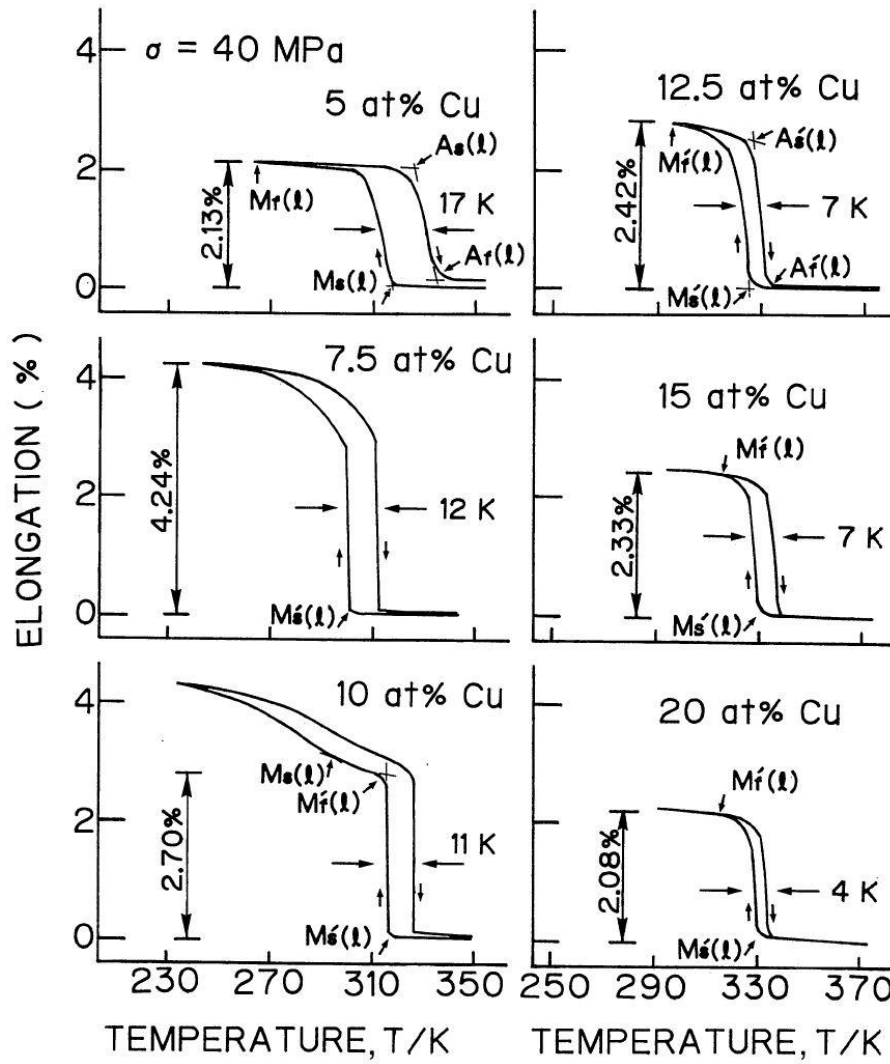


Figure 2.16 Elongation( $\epsilon$ )-temperature( $T$ ) curves under the nearly same stress (about 40 MPa) for TiNiCu alloys [121].

With increasing Cu content, the transformation temperature hysteresis becomes smaller, which means that the B2→B19 transformation has a smaller transformation temperature hysteresis than the B2→B19' transformation. From this figure, it can also be observed that with varying Cu content, the TiNiCu alloys all have good shape memory strain, which is also an important reason for the wide applications of TiNiCu alloys.

TiNiCu alloys have been deployed in many practical applications and also been studied systematically for an extended period already. From references [38, 122-125], the lattice parameters of TiNiCu alloys with different Cu contents have been determined.

The lattice parameters of the B2 parent phase, B19 martensite and B19' martensite phase shown in Figure 2.17 were proposed by Nam et al. [122]. In this figure,  $a_c$  stands for the lattice parameter of the B2 parent phase;  $a_0$ ,  $b_0$  and  $c_0$  represent the lattice parameters of the B19 martensite phase and  $a_m$ ,  $b_m$ ,  $c_m$  and  $\beta$  are for the lattice parameters of the B19' martensite phase. From this figure, it is obvious that the lattice parameter of the B2 parent phase increases slightly with increasing Cu content. The lattice parameters reported by Bricknell et al. [123] for TiNiCu martensite phases with different Cu content at room temperature are shown in Figure 2.18.

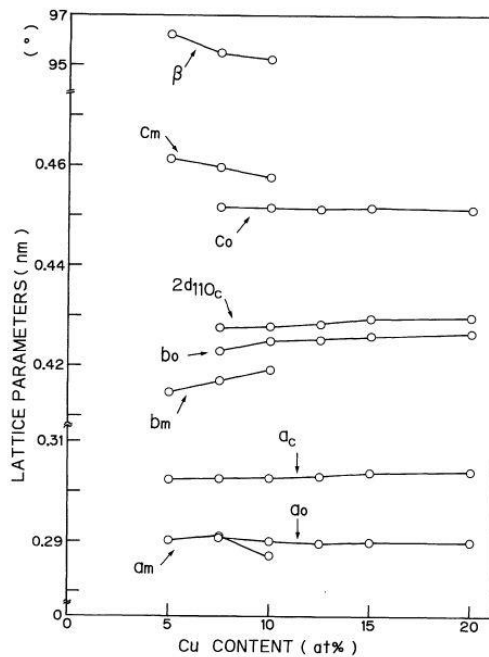


Figure 2.17 Lattice parameters of TiNiCu alloys with different Cu content [122].

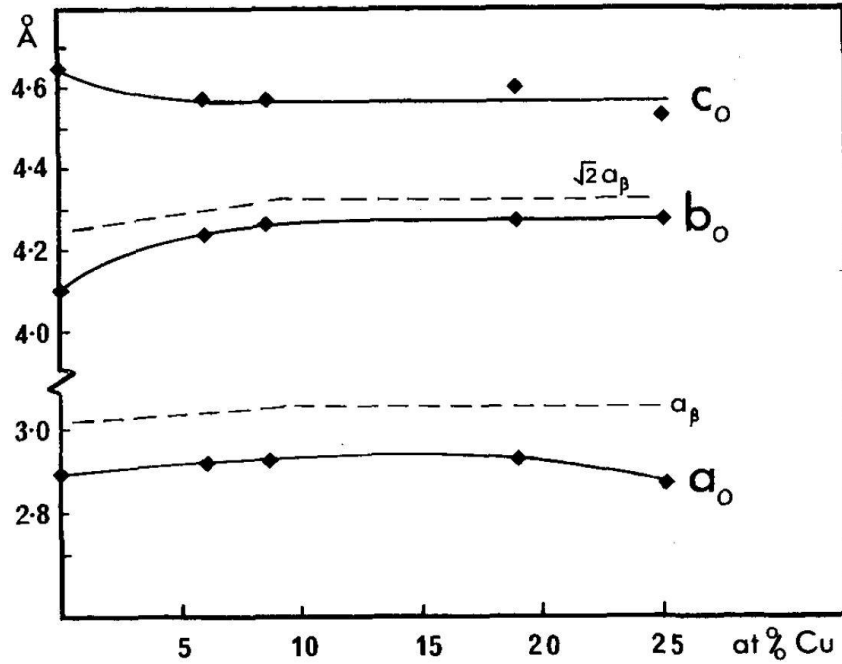


Figure 2.18 Lattice parameters of TiNiCu martensite phase with different Cu content [123].

From these references and the two figures, the lattice parameters of TiNiCu with different phases can be summarized in Table 2.1.

Table 2.1 Crystal structures and lattice parameters of the different phases in TiNiCu alloys.

Phase	a (Å)	b (Å)	c (Å)	$\beta$ (°)
B2-Cubic	3.05	--	--	--
B19-Orthorhombic	2.88	4.28	4.52	--
B19'-Monoclinic	2.89	4.12	4.62	96.5

## 2.4 Recent Computational Studies of TiNi-based SMAs

In the study of SMAs, the electronic structure of each phase is of essential importance for understanding the mechanism of martensitic transformation and its related behavior at the atomic level. Recently, with the development of high

performance computing and refinement of the density functional theory (DFT) methodology, significant progress has been made by first-principle investigations.

For TiNi alloy in general, the high temperature austenite phase is B2 cubic structure and the low temperature martensite phase is B19' monoclinic structure, from experimental observations. However, in reference [126], it was indicated that the reported B19' structure [127, 128] of TiNi is unstable relative to a base-centred orthorhombic (BCO) structure that is not reversible to B2 at the atomic level. The crystal structure of BCO reported by Huang et al. [126] is shown in Figure 2.19. Actually, this so-called BCO is monoclinic structure with a monoclinic angle of  $107^\circ$ . In the present thesis, all BCO structures refer to the monoclinic structure with a monoclinic angle of  $107^\circ$ .

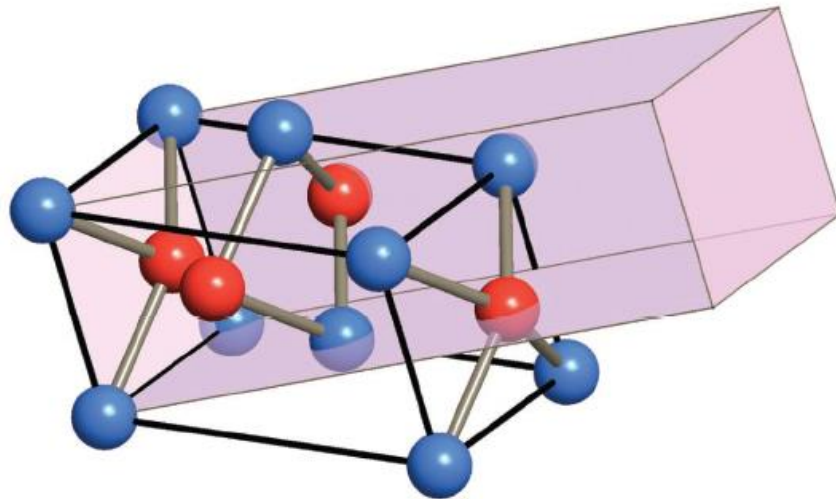


Figure 2.19 The BCO minimum-energy structure with further doubled conventional cell (shaded box) [126].

In order to study the structural energetics of TiNi, a series of DFT calculations were carried out to determine the martensite structure with minimum energy distortion. In this calculation, Vienna ab initio Simulation Package (VASP) [129, 130] was used to optimize the TiNi martensite structure and calculate the total energy with energy cut-off 302 eV, smearing parameter of 0.1 eV and 2000 k-points per atom.

From the calculation, they found that the angle associated with the minimum energy distortion is not the experimentally reported 98 °, but 107 ° instead. In their opinion, the reported structure obtained by experiments is stabilized by a wide range of applied or residual internal stresses which also store the shape information. However, the reason for the difference of martensite structure between experimental observations and calculation results should be further investigated.

In 2011, Šesták et al. [131] proposed that twinning can stabilize B19' structure in TiNi martensite. As illustrated in Figure 2.20, the (1 0 0) compound twins were constructed which contain 10 unit cells of TiNi martensite because this twinning mode can often be observed and is thus easy to be studied.

In this study, the Abinit software [132, 133] and VASP were chosen for carrying out the DFT implementations, along with a pseudopotential approach. The cut-off energies were set to 1000 eV and 500 eV, while the k-point meshes were set to  $1 \times 11 \times 11$  and  $1 \times 13 \times 13$  for Abinit and VASP, respectively.



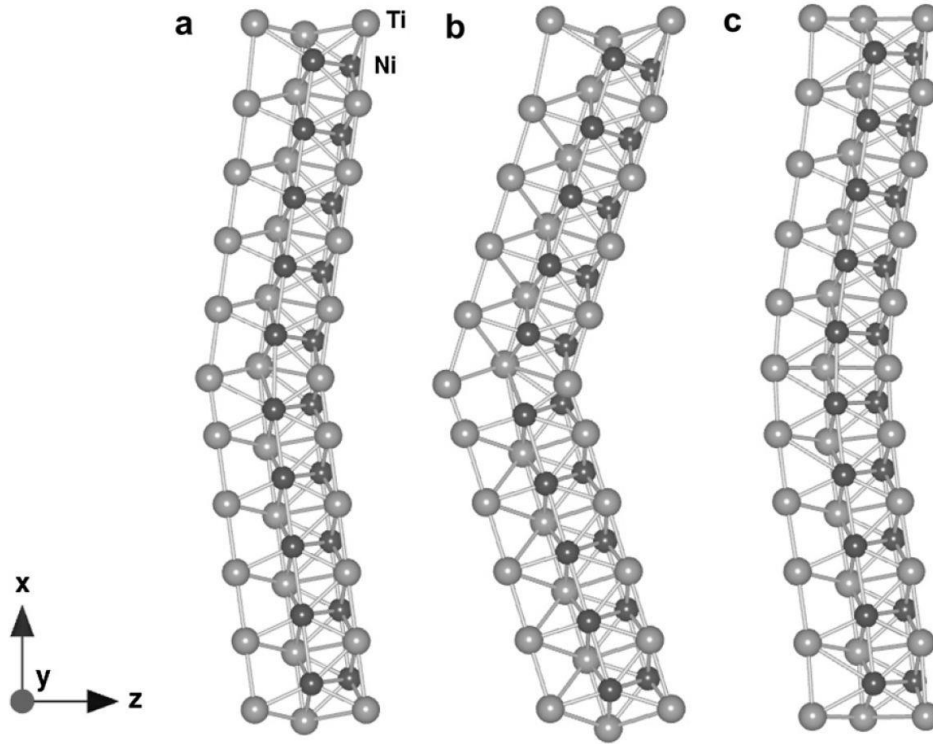


Figure 2.20 The twinned supercells constructed using (a) B19' structural parameters and (b) BCO structural parameters before their optimization. (c) The result of the optimization process. [131].

The calculation results suggested that with (1 0 0) compound twins, the lattice parameters of B19' structure were much closer to the experimental results than to the theoretical BCO. Thus it demonstrated that the B19' structure in TiNi martensite can be stabilized by twinning, but more kinds of twins should be studied to further establish that twinning is generally able to stabilize the TiNi martensite structure.

A new martensite structure of TiNi called B19'' phase was predicted by Guda Vishnu [134]. The crystal structure of this B19'' phase and the energy of B19', B19'' and BCO with different monoclinic angle are shown in Figure 2.21 and Figure 2.22, respectively.

In this study, the SeqQuest code [135] was used to implement the calculations with norm-conserving pseudopotential. A  $14 \times 10 \times 10$  k-mesh was used for the calculations of all phases.

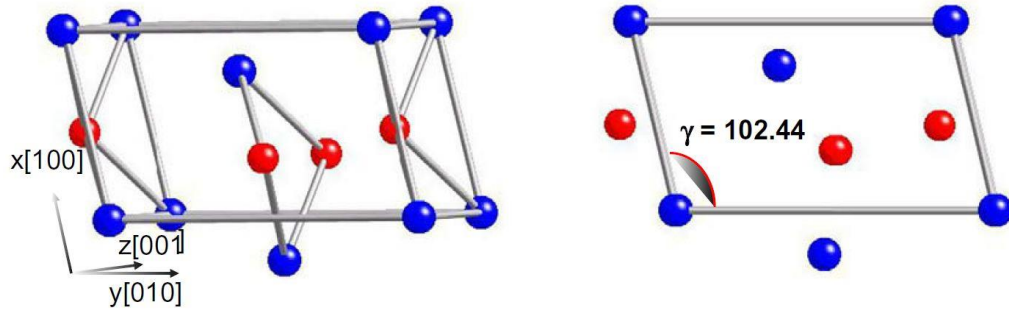


Figure 2.21 Crystal structure of B19'' phase [134].

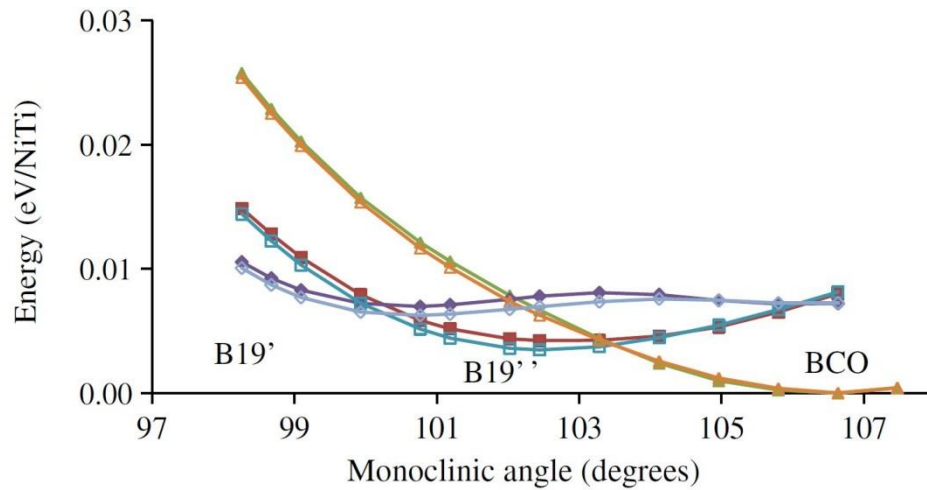


Figure 2.22 Energy of B19', B19'' and BCO with different monoclinic angle [134].

It was stated in [134] that there is a small energy barrier of 1 meV/TiNi in the  $B2 \rightarrow B19'$  transformation, and that there is no energy barrier in the  $B2 \rightarrow B19$  transformation, but this is inconsistent with reference [136] in which the energy barrier is reported to be 13 meV/TiNi. It also considered the B19'' phase as an intermediate phase between the transition from B19' to BCO, and

that the B19'' phase may play a role in the stabilization of the observed B19' structure. However, the existence of the B19'' phase should be examined more closely with further numerical efforts.

Teng et al. [137] carried out ab initio calculations to investigate how the crystal structure will change when Cu is substituted for Ni in TiNi binary alloy.

The structures used to carry out the calculations are illustrated in Figure 2.23.

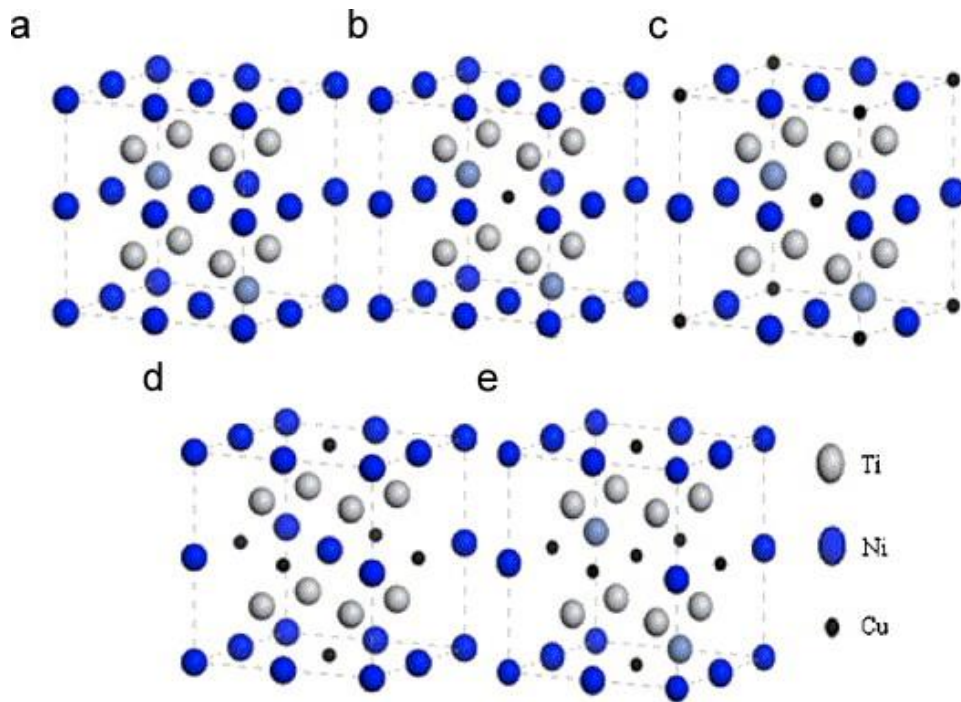


Figure 2.23 The  $2 \times 2 \times 2$  supercells of (a)  $\text{Ti}_{50}\text{Ni}_{50}$ ; (b)  $\text{Ti}_{50}\text{Ni}_{43.75}\text{Cu}_{6.25}$ ; (c)  $\text{Ti}_{50}\text{Ni}_{37.5}\text{Cu}_{12.5}$ ; (d)  $\text{Ti}_{50}\text{Ni}_{31.25}\text{Cu}_{18.75}$ ; (e)  $\text{Ti}_{50}\text{Ni}_{25}\text{Cu}_{25}$ . [137].

The  $2 \times 2 \times 2$  supercells of B2 phase with cubic structure were built for the calculations. In this calculation, the cut-off energy was set to 310 eV and the k-point mesh was set to  $4 \times 4 \times 4$ . From the calculation results, it was found that both the formation energy and lattice constant increased with increasing Cu content, to the limit of 25 at% Cu substituting for Ni. The conclusion was made

that the structure of B2 phase becomes progressively more stable; Ti-Ni and Ti-Cu bonds are stronger as progressively more electrons transfer from Ti atoms to Ni and Cu atoms with increasing Cu content. Thus the layer transition is more difficult.

Moreover, a number of calculations on the influences of twinning structures were carried out using first-principle methods. It was indicated that in the  $\{1\ 1\ 0\}$  planes, shearing was much easier than in the  $\{1\ 1\ 2\}$  planes for the TiNi B2 phase [138]. Small energy barriers were obtained by Ezaz et al. [139] for the  $(1\ 0\ 0)$  and  $(0\ 0\ 1)$  twinning cases in the B19' martensite phase of TiNi, which are less than  $7.6\ \text{mJ m}^{-2}$  and  $41\ \text{mJ m}^{-2}$ , respectively. Wang [140] also demonstrated the importance of studying the twinned martensite structure for understanding the mechanism of shape memory effect in the smart alloys. Recently, various twinning modes in TiNi martensite have also been studied and it was found that the hydrostatic stress has significant contributions to the stabilization of B19' martensite structure [141-143].

# Chapter 3 First-Principle Method

In this chapter, the basic information on first-principle calculation is introduced. Following the convergence test, the equiatomic TiNi martensite crystal structure is optimized using the basis set obtained from the convergence test.

## 3.1 Background

With the advent of super computers and high performance computing, many computational methods have been used for electronic structure calculations. These methods span from very accurate quantum chemistry techniques applied to a small number of molecules, to tight-binding semi-empirical schemes which makes it possible to simulate systems composed of about one thousand molecules.

The application of first-principle methods which are also called ab initio methods uses the basic laws of quantum mechanics, to simulate matter at the atomic scale in a highly accurate manner. The physical and mechanical properties can be calculated without recourse to experimental input.

For quantum mechanical modeling, the Schrödinger equation is the basis for describing the physical and chemical properties of ensembles of particles. The behavior of the nuclei and electrons which build up the solids are governed by the basic laws of quantum theory expressed by the Schrödinger equation. While it is not possible to solve the N-electron Schrödinger equation directly,

several assumptions and methods are proposed to obtain the solutions of the Schrödinger equation.

### **3.2 The Schrödinger Equation**

The physical and chemical properties of matter are usually described by an ensemble of particles, which can be very complex. However, regardless of what phase or state (gas, liquid or solid) these particles are in, whether they distribute in the system in a homogenous, amorphous or heterogeneous way, they can be unambiguously treated as some well-defined collection of interacting atoms. For these atoms, one of the fundamental parameters which attract our interest is their energy. Moreover, it is also important to know how this energy changes if the atoms move around.

As it is well-known, an atom is formed by its nucleus and electrons. The mass of the atomic nuclei is much greater than that of the electrons, and the approximate ratio of the mass of a proton in a nucleus to an electron is  $1836 : 1$ . Therefore, electrons respond much more rapidly to changes in their surroundings than nuclei can. This also means that the electron motion is much faster than the nuclei motion. Thus, the nuclei can be considered to be fixed. As a result, this physical question can be sliced into two parts. Firstly, for fixed positions of atomic nuclei, we can solve the equations that describe the electron motion. Then, for a given set of electrons moving in the field of a set of nuclei, the lowest energy configuration, or state, of the electrons can be found. The lowest state is known as the ground state of electrons. The separation of the

general problem into the nuclei and electrons is frequently called the Born-Oppenheimer approximation [144].

One simple form of the Schrödinger equation, which is the time-independent, nonrelativistic Schrödinger equation, is as follows:

$$\mathbf{H}\psi = E\psi \quad (3.1)$$

where  $\mathbf{H} = \mathbf{T} + \mathbf{V}$ . In this equation,  $\mathbf{H}$  is the Hamiltonian operator;  $E$  is the total energy and  $\psi$  is a set of solutions of the Hamiltonian.  $\mathbf{T}$  and  $\mathbf{V}$  are the kinetic energy and potential energy, respectively.

The simplest case we can have is that of just one particle without potential energy in a free space. In this situation,  $\mathbf{V} = 0$  and the Schrödinger equation becomes

$$\mathbf{T}\psi = E\psi \quad (3.2)$$

where  $\mathbf{T} = \frac{-\hbar^2}{2m} \frac{d^2}{dx^2}$  with  $\hbar$  being the reduced Planck's constant ( $1.05457266 \times 10^{-34} \text{ m}^2\text{kg/s}$ ). Finally, the equation can be obtained as:

$$\left( \frac{d^2}{dx^2} + \frac{2mE}{\hbar^2} \right) \psi = 0 \quad (3.3)$$

If we define  $k$  as  $k^2 = \frac{2mE}{\hbar^2}$ , we can obtain  $\psi = Ae^{ikx} + Be^{-ikx}$ .

However, we are generally interested in the situation where multiple electrons are interacting with multiple nuclei. In this case, a more complete description of the Schrödinger equation is

$$\left[ \frac{\hbar^2}{2m} \sum_{i=1}^N \nabla_i^2 + \sum_{i=1}^N V(\mathbf{r}_i) + \sum_{i=1}^N \sum_{j < i}^N U(\mathbf{r}_i, \mathbf{r}_j) \right] \psi = E\psi \quad (3.4)$$

where  $\hbar$  is the reduced Planck's constant,  $m$  is the electron mass and  $\nabla_i^2$  is the Laplacian operator with respect to the electronic coordinates. In this equation, the three terms in the bracket are respectively the kinetic energy of each electron, the interaction energy between each electron and the collection of atomic nuclei, and the interaction energy between different electrons.

For the chosen Hamiltonian without consideration of electron spin,  $\psi$  is the electronic wave function, which is a function of the spatial coordinates of each of the  $N$  electrons. Thus,  $\psi = \psi(\mathbf{r}_1, \dots, \mathbf{r}_N)$  and  $E$  is the ground-state energy of the electrons. The ground-state energy is independent of time, and this is thus the time-independent Schrödinger equation.

### 3.3 Hartree-Fock Theory

The Hartree-Fock (HF) theory was developed to enable a solution to the Schrödinger equation and includes the effects of the electrostatic repulsion of electrons. It is a method of approximation for the determination of the ground-state wave function and ground-state energy of a quantum many-body system by numerical techniques. The first simplification it uses is the Born-Oppenheimer approximation as mentioned in Section 3.2. The second approximation is the replacement of the many-electron Hamiltonian with an effective one-electron Hamiltonian, which acts on one-electron wave functions



called orbitals. The Coulomb repulsion between electrons is represented in an averaged manner. In other words, the HF method is a mean-field approach [145].

### 3.3.1 Slater Determinant

Two important principles, which are the antisymmetry principle and the Pauli exclusion principle, have to be considered. The antisymmetry principle states that the wave function must change sign if two electrons change places with each other. The Pauli exclusion principle states that no two electrons can have the same set of quantum number, and each spatial orbital can only accommodate two electrons of opposite spin.

For a system of  $N$  electrons, if the electrons have no effect on each other, the Hamiltonian for the electrons can be written as:

$$H = \sum_{i=1}^N h_i \quad (3.5)$$

where  $h_i$  is the kinetic and potential energies of the electron  $i$ . For just one electron based on this Hamiltonian, the Schrödinger equation should be

$$h\varphi = E\varphi \quad (3.6)$$

where  $\varphi$  is a set of eigenfunctions which are also called spin orbitals. When the total Hamiltonian is simply a sum of one-electron operators, the eigenfunctions of  $H$  are products of the one-electron spin orbitals:

$$\psi(\mathbf{r}_1, \dots, \mathbf{r}_N) = \varphi_1(\mathbf{r}_1) \varphi_2(\mathbf{r}_2) \cdots \varphi_N(\mathbf{r}_N) \quad (3.7)$$

where  $\mathbf{r}_i$  is a vector of coordinates that defines the position of electron  $i$  and its spin state (up or down). This product of spin orbitals is called the Hartree product. However, the Hartree product is not adequate because it does not satisfy the antisymmetry principle.

Thus, a better approximation to the wave function uses a Slater determinant, which is the determinant of an  $N \times N$  matrix of single-electron spin orbitals for a system of  $N$  electrons. The Slater determinant can be written as:

$$\psi(\mathbf{r}_1, \dots, \mathbf{r}_N) = \frac{1}{\sqrt{N!}} \det \begin{bmatrix} \varphi_1(\mathbf{r}_1) & \varphi_2(\mathbf{r}_1) & \cdots & \varphi_N(\mathbf{r}_1) \\ \varphi_1(\mathbf{r}_2) & \varphi_2(\mathbf{r}_2) & \cdots & \varphi_N(\mathbf{r}_2) \\ \vdots & \vdots & \ddots & \vdots \\ \varphi_1(\mathbf{r}_N) & \varphi_2(\mathbf{r}_N) & \cdots & \varphi_N(\mathbf{r}_N) \end{bmatrix} \quad (3.8)$$

where  $\frac{1}{\sqrt{N!}}$  is a normalization factor,  $\varphi_j(\mathbf{r}_i)$  a function that depends on the space and the coordinates of the electron at  $\mathbf{r}_i$ , and  $j$  is the number of the spin orbital.

As the Slater determinant satisfies both the antisymmetry principle and the Pauli exclusion principle, it can be used to solve Schrödinger equation which includes exchange.

### 3.3.2 Hartree-Fock Theory

In Hartree-Fock (HF) calculation, the complete wave function can be approximated using a single Slater determinant. We fix the positions of the atomic nuclei and focus on determining the wave function of  $N$ -interacting electrons. We look for the minimum of the many-electron Schrödinger equation in the class of all wave functions that are written as a single Slater determinant. In the HF equation, a single electron is affected by other electrons as an average, rather than by the instantaneous repulsive forces.

$$\psi(\mathbf{r}_1, \dots, \mathbf{r}_N) = \|\text{Slater}\| \quad (3.9)$$

$$\begin{aligned} & \left[ -\frac{1}{2} \nabla_i^2 + \sum_I V(\mathbf{R}_I - \mathbf{r}_i) \right] \varphi_\lambda(\mathbf{r}_i) \\ & + \left[ \sum_\mu \int \varphi_\mu^*(\mathbf{r}_j) \frac{1}{|\mathbf{r}_j - \mathbf{r}_i|} \varphi_\mu(\mathbf{r}_j) d\mathbf{r}_j \right] \varphi_\lambda(\mathbf{r}_i) \\ & - \sum_\mu \left[ \int \varphi_\mu^*(\mathbf{r}_j) \frac{1}{|\mathbf{r}_j - \mathbf{r}_i|} \varphi_\lambda(\mathbf{r}_j) d\mathbf{r}_j \right] \varphi_\mu(\mathbf{r}_i) = \varepsilon \varphi_\lambda(\mathbf{r}_i) \quad (3.10) \end{aligned}$$

In order to solve the HF equation, the self-consistent approach is used and the HF calculation is actually an iterative procedure. First, an initial estimate of the spin orbitals is made. Then, the electron density is defined from the current estimate of the spin orbitals. Next, the single-electron equations for the spin orbitals are solved using the electron density obtained. This procedure is iterated until convergence is achieved where the solved spin orbitals are

consistent with the initial spin orbitals. The procedure of the HF method is shown in Figure 3.1.

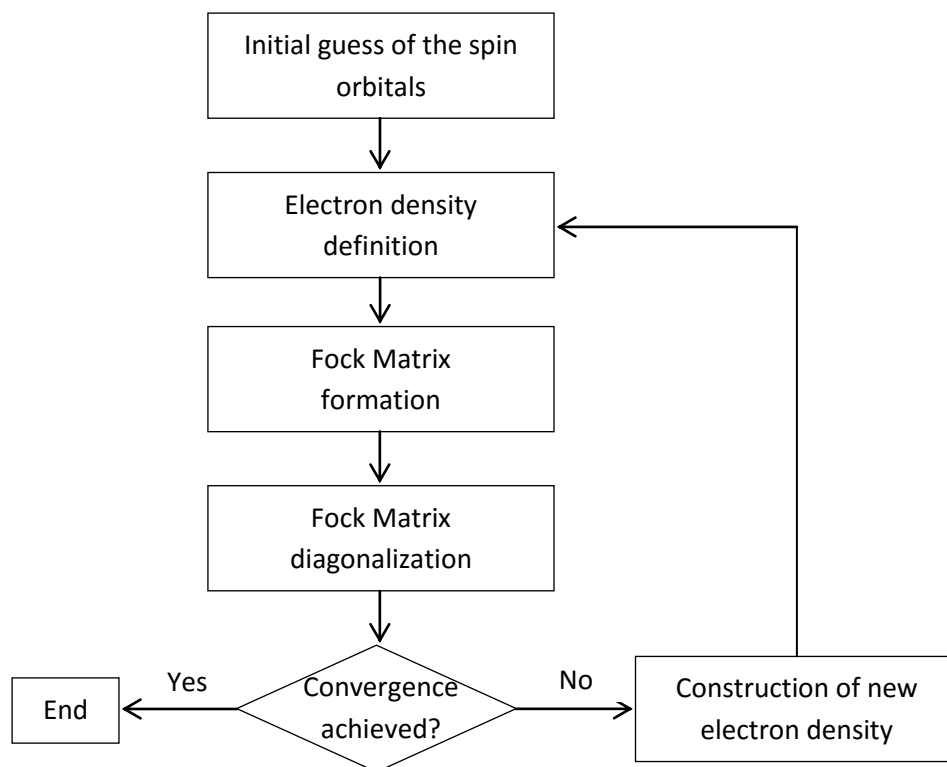


Figure 3.1 Flow chart of Hartree-Fock method.

### 3.3.3 Limitations of Hartree-Fock Theory

It has been demonstrated that the Hartree-Fock theory is an effective method for the calculation of electronic structure, especially for the ground states of molecules near the equilibrium geometries. However, significant challenges have to be overcome when using the HF method.

Electron correlation is basically the repulsion between pairs of electrons. If there is no interaction among electrons, which is impossible in reality, the

quantum eigenstates could be solved exactly. For the HF theory, the challenge in electronic structure calculations is dealing with electron correlation. The HF theory does not treat electron correlation exactly since it only treats electron correlation in an average manner. Thus, the HF method is not able to provide exact solutions to the Schrödinger equation, and neglecting electron correlation can lead to severely anomalous results which have large deviations from actual experimental observations.

As the HF method is an iterative method, another drawback is that it is often difficult to achieve convergence for excited states of the wave functions. In general, the excited state collapses to the ground state upon orbital optimization as it has a different overall symmetry than the ground state. Thus, the HF method cannot provide useful information on the charge densities of excited states.

An alternative to Hartree-Fock calculations used in many studies today is density functional theory, which treats both exchange and correlation energies, albeit approximately.

### **3.4 Density Functional Theory**

The density functional theory (DFT) method is one of the most popular ab initio methods used in computational material science and solid-state physics. It is widely used because of its relatively high computational efficiency among the first-principle methods as well as its high accuracy. The DFT provides a

method to efficiently and accurately determine the ground state electronic structure of a system [146-148].

In contrast to the Hartree-Fock procedure, which begins with a description of each individual electron's interaction with the nuclei and other electrons in the system, the DFT method starts with a consideration of the whole electron system. In the DFT method, the properties of a many-electron system can be determined by employing a functional, which is the function of another function. In this case, the functional is the spatially dependent electron density. Hence the name density functional theory comes from the usage of a functional of the electron density.

Within the DFT, all aspects of the electronic structure of the system of interacting electrons are completely determined by the electronic charge density. In fact, two fundamental mathematical theorems are the essence of the DFT, which are the Hohenberg-Kohn theorem and the Kohn-Sham theory.

### 3.4.1 Hohenberg-Kohn Theorem

The Hohenberg-Kohn theorem is one of the core concepts of the DFT which shows that the energy of a quantum-mechanical system is uniquely determined by its electron density. It states that, for a given ground-state density, it is possible in principle, to calculate the corresponding unique ground-state wave functions [147, 149].

In this thesis,  $n(\mathbf{r})$  is defined as the electron density at position  $\mathbf{r}$ . Thus, the Hohenberg-Kohn theorem can be described herewith: the ground state energy  $E$  can be expressed as  $E[n(\mathbf{r})]$ , which implies that the ground state electron density uniquely determines all properties, including the energy and wave function, of the ground state. This theorem is important because based on it, the Schrödinger equation can be solved, meaning that the ground state energy can be found, by determining the electron density, a function of three spatial variables, rather than the wave function, a function of  $3N$  variables for  $N$ -electron systems.

However, the first Hohenberg-Kohn theorem simply proves that a functional of the electron density exists which is helpful for solving the Schrödinger equation. The second Hohenberg-Kohn theorem provides an explanation about what the functional actually is. It states that the proper electron density corresponding to the solution of the Schrödinger equation is the one which can minimize the energy of the overall functional. The energy functional can be written as

$$E[n(\mathbf{r})] = T_s[n(\mathbf{r})] + V_{Ne}[n(\mathbf{r})] + E_{xc}[n(\mathbf{r})] \quad (3.11)$$

$$V_{Ne}[n(\mathbf{r})] = \int n(\mathbf{r})V_{ext}(\mathbf{r})d\mathbf{r} \quad (3.12)$$

$$T_s[n(\mathbf{r})] = -\frac{1}{2} \sum_{i=1}^N \langle \psi(\mathbf{r}) | \nabla^2 | \psi(\mathbf{r}) \rangle \quad (3.13)$$

where  $T_s[n(\mathbf{r})]$  is defined as the kinetic energy of a non-interacting electron gas with density  $n(\mathbf{r})$ , and is not the kinetic energy of the real system;  $V_{Ne}[n(\mathbf{r})]$  is the electron-nuclei interaction; and  $E_{xc}[n(\mathbf{r})]$  is the exchange-correlation energy, which includes all the kinetic terms due to interactions with the electron gas.  $V_{ext}(\mathbf{r})$  is an additive constant which is determined by  $n(\mathbf{r})$ .

In Eq. (3.11), the kinetic energy term  $T_s$  and the exchange-correlation energy  $E_{xc}$  are difficult to express in terms of the electron density. In order to express  $T_s$ , the Kohn-Sham Theory is invoked and the local density approximation is often used to determine  $E_{xc}$ .

### 3.4.2 Kohn-Sham Theory

In order to express the kinetic energy term, Kohn and Sham [148] proposed a hybrid method involving both the wave function and electron density to simplify the many-body system. By this method, the many-body system is simplified into a system in which a single electron moves without interaction with the others in an effective potential field. The effective potential field includes the external potential and the influence of coulomb interaction among electrons. Thus, the Schrödinger equation can be simplified into a simple single-particle system rather than an  $N$ -electron system.

The kinetic energy can be calculated from the wave function which can be written in terms of non-interacting orbitals



$$n(\mathbf{r}) = \sum_{i=1}^N |\psi_i(\mathbf{r})|^2 \quad (3.14)$$

Thus, the total energy functional can be written as

$$\begin{aligned} E[n(\mathbf{r})] = & T_s[n(\mathbf{r})] + \frac{1}{2} \iint \frac{n(\mathbf{r})n(\mathbf{r}')}{|\mathbf{r} - \mathbf{r}'|} d\mathbf{r}d\mathbf{r}' + E_{xc}[n(\mathbf{r})] \\ & + \int n(\mathbf{r})V_{ext}(\mathbf{r})d\mathbf{r} \end{aligned} \quad (3.15)$$

In this equation, the second term on the right side is the self-interaction, which represents interaction of  $n(\mathbf{r})$  with itself.  $V_{ext}(\mathbf{r})$  is the external potential which indicates the potential due to nuclei. The functional  $E_{xc}[n(\mathbf{r})]$  is the exchange-correlation energy which contains all the interaction terms.

By applying the variational principle, a normalization constraint is introduced on the electron density, and the following equations can be written:

$$\int n(\mathbf{r})d\mathbf{r} = N \quad (3.16)$$

$$\left[ -\frac{1}{2}\nabla^2 + \left( V_{ext}(\mathbf{r}) + \int \frac{n(\mathbf{r}')}{|\mathbf{r} - \mathbf{r}'|} d\mathbf{r}' + V_{xc}(\mathbf{r}) \right) \right] \psi_\lambda = E_\lambda \psi_\lambda \quad (3.17)$$

where  $\psi_\lambda$  is the wave function for the  $\lambda^{\text{th}}$  orbital, and  $V_{xc}(\mathbf{r})$  is the potential due to the exchange-correlation energy  $E_{xc}$ , which is defined as the functional derivative of  $E_{xc}$  with respect to  $n(\mathbf{r})$

$$\frac{\delta E_{xc}[n(\mathbf{r})]}{\delta n(\mathbf{r})} = V_{xc}(\mathbf{r}) \quad (3.18)$$

Thus, the effective potential is

$$V_{\text{eff}}(\mathbf{r}) = V_{\text{ext}}(\mathbf{r}) + \int \frac{n(\mathbf{r}')}{|\mathbf{r} - \mathbf{r}'|} d\mathbf{r}' + V_{xc}(\mathbf{r}) \quad (3.19)$$

Effectively, Eq. (3.17) is a single particle Schrödinger equation, and the self-consistent solution leads to the ground state charge density of the system.

### 3.4.3 Local Density Approximation

The local density approximation (LDA) is a class of approximations to the exchange-correlation energy functional in the DFT. In fact, the notable local approximations are derived from the homogeneous electron gas model. Thus, the LDA is generally synonymous with functionals based on the homogeneous electron gas approximation. The LDA states that for regions of a material where the electron density varies slowly on an atomic scale, the exchange-correlation energy at the point  $\mathbf{r}$  can be considered the same as that for a locally uniform electron gas of the same electron density, and the total exchange-correlation energy can be obtained by integrating the uniform electron gas result [150, 151].

As such, the exchange-correlation energy functional  $E_{xc}$  can be written as

$$E_{xc}^{LDA}[n(\mathbf{r})] = \int \varepsilon_{xc}[n(\mathbf{r})]n(\mathbf{r}) d\mathbf{r} \quad (3.20)$$

where  $\varepsilon_{xc}[n(\mathbf{r})]$  is the exchange-correlation energy per particle of a uniform electron gas of density  $n(\mathbf{r})$ . In fact, the LDA is a very simple approximation.

However, this approximation forms the core for most current DFT codes

because of its surprising accuracy. However, some shortcomings still exist for the LDA. The atomic ground state energy and ionization energies are usually under-predicted when applying this approximation. In addition, the binding energies are often over-predicted. It is also known to overly favor high spin state structures. As a result, another approximation method named the generalized gradient approximation (GGA) was proposed to make the exchange-correlation energy more accurate. Since the major source of error in the LDA is the exchange energy, the gradient of the density, as well as the value, at a given point are considered in GGA.

### 3.4.4 Generalized Gradient Approximation

The LDA uses the exchange-correlation energy for the ideal uniform electron gas at every point in the system. However, the electron density of a real system is far from uniform, and the computational results by LDA usually are not able to meet the requirements. To further improve the numerical accuracy, we need to consider the inhomogeneity of electron density, which means that for a system with inhomogeneous electron density, not only the electron density  $n(\mathbf{r})$  at a particular point  $\mathbf{r}$ , but also the gradient of the electron density  $\nabla n(\mathbf{r})$  is considered. This method is known as the generalized gradient approximation (GGA) [152-154].

The GGA can be written in terms of an analytic function known as the enhancement factor,  $F_{xc}[n(\mathbf{r}), \nabla n(\mathbf{r})]$ , which directly modifies the LDA energy

density. Thus, the exchange-correlation energy functional  $E_{xc}^{GGA}$  can be written as

$$E_{xc}^{GGA}[n(\mathbf{r})] = \int n(\mathbf{r}) \varepsilon_{xc}[n(\mathbf{r})] F_{xc}[n(\mathbf{r}), \nabla n(\mathbf{r})] d\mathbf{r} \quad (3.21)$$

For very high electron density, the exchange-correlation energy plays a predominant role. Thus, the GGA non-locality is quite suitable for dealing with the inhomogeneity of the electron density. The GGA can significantly improve the numerical results of the exchange-correlation energy, while the ionization energies only incur small changes. When using the GGA, the bond lengths of molecules and the lattice constants of solids increase slightly, but the dissociation energy and the cohesive energy can be significantly decreased. Generally, the GGA results compare well with experimental observations, not only for the bond energies of covalent and metallic bonds, but also significantly improve those of hydrogen bonds and van der Waals interactions.

### 3.4.5 Limitations of Density Functional Theory

The procedure of the DFT method can be presented as shown in Figure 3.2. It is important to note that practical DFT calculations are not the exact solutions of the full Schrödinger equation since the exact functional that the Hohenberg-Kohn theorem applied to is not known. As the Hohenberg-Kohn theorem is only applicable for the ground state energy, the DFT calculations have limited accuracy in the calculations of excited electronic states. Another shortcoming of the DFT is the underestimation of calculated band gaps in semiconducting and

insulating materials. Moreover, the DFT calculations may provide inaccurate results for the weak van der Waals attractions which exist between atoms or molecules.

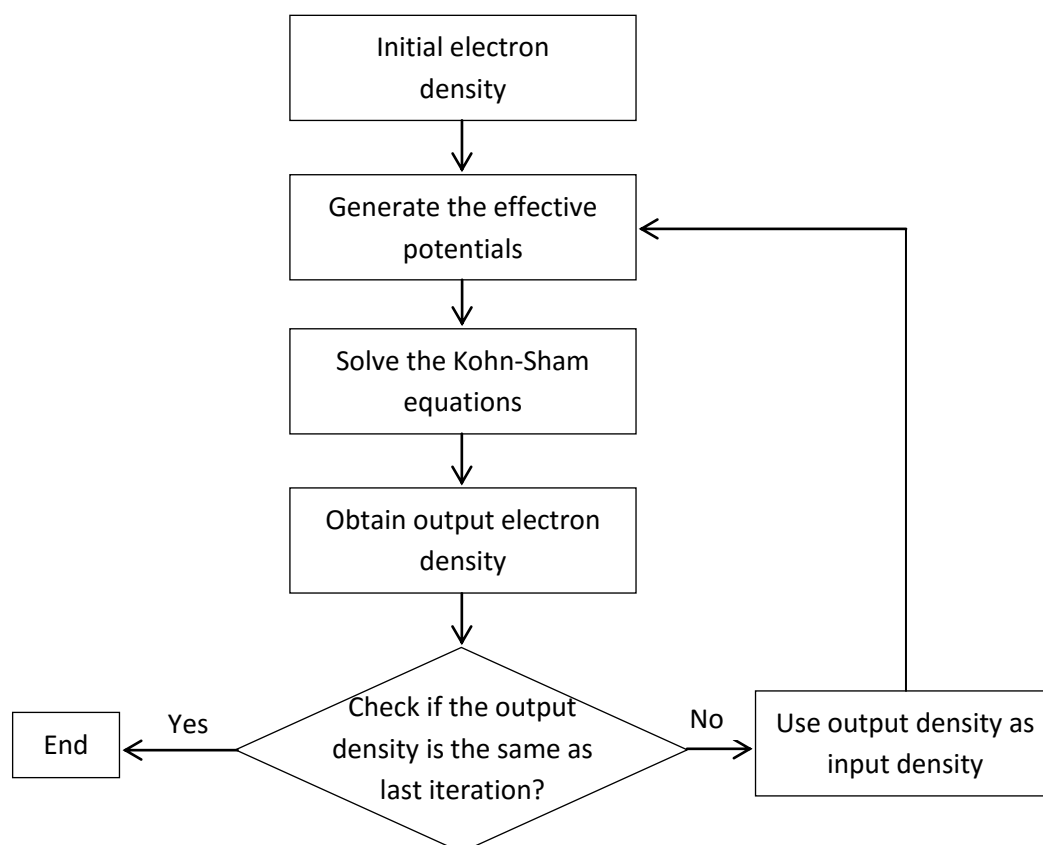


Figure 3.2 Flow chart of DFT method.

### 3.5 CASTEP Based on DFT

There are several codes to carry out DFT calculations. In our research, the CASTEP code is used.

CASTEP was originally developed by Payne et al. [155] in the late 1980s and early 1990s. It was then completely redesigned in 1999 in order to allow refinements to be easily added in a rapid manner [156].

In CASTEP, the plane-wave pseudopotential approach is used to solve a set of one-electron Schrödinger equations. The wave functions are expanded in a plane wave basis set and the potentials can be described either by norm-conserving pseudopotential [157] or ultrasoft pseudopotential [158].

CASTEP is a powerful DFT solver which can carry out a series of quantum chemistry calculations with different basis sets such as structure optimization, total energies, electronic structure, etc. Usually, the results based on the local density approximation (LDA) are obtained by using the Perdew–Zunger [159] parameterization, while the generalized gradient approximation (GGA) results are obtained by using the Perdew–Wang [160] parameterization in both spin-dependent and spin-independent forms.

In this thesis, the CASTEP code is used to study the structures of TiNi-based SMAs. All TiNi-based structures considered were found to be paramagnetic in spin-dependent versions of the LDA and GGA. For Ti, the pseudopotential was constructed by treating the occupied 3p electronic levels as valence levels.

### 3.5.1 Geometry Optimization

A routine feature in molecular simulation is the optimization of the structure or minimization of the potential energy of the system being examined. For instance, it is always desirable to optimize a structure after it has been sketched, since sketching often creates the molecular model in a high energy

configuration and starting a simulation from such a structure without optimization can lead to erroneous results. Thus, geometry optimization is usually the first step, which is also a very important step, in a simulation run.

For the CASTEP code, it supports two schemes for geometry optimization, which are the Broyden–Fletcher–Goldfarb–Shanno (BFGS) method [155] and the damped molecular dynamics method [161]. The BFGS method is widely used since it is able to perform cell optimization including optimization at fixed external stress, while damped molecular dynamics method involves only internal coordinates which means the cell parameters have to be fixed.

The BFGS scheme uses a starting Hessian Matrix which is recursively updated during optimization. The CASTEP implementation involves a Hessian in the mixed space of internal and cell degrees of freedom, so that both lattice parameters and atomic coordinates can be optimized.

### 3.5.2 Pseudopotentials

It is obvious that the calculation could run faster with a smaller system size, and one important way to simplify the system is through the use of pseudopotentials. From a physical viewpoint, the tightly bound core electrons are not especially important in defining chemical bonding and other physical characteristics of materials. These properties are dominated by the less tightly bound valence electrons.

Pseudopotentials are used to replace the electron density from a chosen set of core electrons with a smoothed density chosen to match various important physical and mathematical properties of the true ion core. A solid can be considered as a collection of valence electrons and ion cores. The ion cores contain nuclei and tightly bound core electrons. The valence-electron wave functions are orthogonal to core wave functions. In a pseudopotential method, the ion cores are considered to be frozen which means that properties of the molecular system are calculated on the assumption that the ion cores are not involved in chemical bonding and do not change as a result of structural modifications. This assumption is called the frozen core approximation.

All-electron wave functions of valence electrons exhibit rapid oscillations in the core region in order to satisfy the orthogonality constraint. It is impractical to represent such functions using plane waves as the size of the basis set would be prohibitive. The pseudopotential approximation replaces core electrons and the strong Coulomb potential by a weaker pseudopotential that acts on a set of pseudo wave functions. This potential can be represented with a small number of Fourier coefficients. Traditionally, pseudopotentials are constructed so as to faithfully reproduce the scattering properties of the full ionic potential [162].



### 3.5.3 Energy Cutoff

The cutoff energy  $E_{\text{cut}}$  is an important parameter which must be defined whenever a DFT calculation is performed. Following expansion of the plane waves, a series of plane waves are chosen with respect to a given energy, which is called the cutoff energy. Thus, when a higher cutoff energy is chosen, more plane waves can be used and the calculations become more accurate. However, the proportion of the high energy portion is relatively small after expanding the plane waves, and with more plane waves, more computational time is required to carry out the calculations. So for overall efficiency considerations, the cutoff energy cannot be too high. In this respect, the pseudopotentials, especially the ultrasoft pseudopotentials, can be used to allow calculations to be performed with a low cutoff energy for the plane wave basis set.

### 3.5.4 Mulliken Population Analysis

It is important to determine the charge or spin distribution of a molecular system or cluster since it can be used to interpret the results in terms of qualitative concepts. There are several ways to analyze the atomic charges, among which the Mulliken Population Analysis (MPA) is often used.

Due to the delocalized nature of the basis states, a disadvantage of the use of a plane wave basis set is that it provides no information regarding the localization of the electrons in the system. Thus, a series of formalism was

proposed and described by Segall et al. [163, 164] to carry out the calculations of Mulliken charges and bond populations.

Mulliken charges arise from the Mulliken population analysis and provide a means of estimating partial atomic charges from calculations carried out by the methods of computational chemistry.

Population analysis in CASTEP is performed using a projection of the plane wave states onto a localized basis using a technique described by Sanchez-Portal et al. [165]. Population analysis of the resulting projected states is then performed using the Mulliken formalism [166]. This technique is widely used in the analysis of electronic structure calculations.

### 3.5.5 The Density of State

The electronic density of states (DOS) acts as another primary quantity used to describe the electronic state of a material. In solid-state and condensed matter physics, the DOS of a system describes the number of states per interval of energy at each energy level that are available to be occupied by electrons. Unlike isolated systems, the atoms or molecules in solid-state are in gas phase, and the density distributions are not discrete like a spectral density but continuous. A high DOS at a specific energy level means that there are many states available for occupation. A DOS of zero means that no states can be occupied at that energy level. In general a DOS is an average over the space and time domains occupied by the system.

In order to calculate the available states in k-space, the energy-momentum relation in parabolic bands is used to give the density of states in terms of energy. By considering the electrons in a solid as free electron gas, the free electron of mass  $m$  has a velocity  $\mathbf{v}$  and a momentum  $\mathbf{p} = m\mathbf{v}$ . The energy consists entirely of kinetic energy as potential energy is zero. Thus,

$$E = \frac{1}{2}m\mathbf{v}^2 = \frac{|\mathbf{p}|^2}{2m} \quad (3.22)$$

A wave number  $\mathbf{k}$  can be given because of the idea of particle-wave duality

$$\mathbf{k} = \frac{\mathbf{p}}{h} \quad (3.23)$$

Considering the equation for energy of the electron in terms of  $\mathbf{k}$

$$E = \frac{h^2}{2m}(k_x^2 + k_y^2 + k_z^2) = \frac{h^2|\mathbf{k}|^2}{2m} \quad (3.24)$$

Thus,

$$|\mathbf{k}| = \sqrt{\frac{2mE}{h^2}} \quad (3.25)$$

Therefore, the solution of the Schrödinger equation can be written in the form

$$\psi(\mathbf{r}) = C \exp(i\mathbf{k} \cdot \mathbf{r}) \quad (3.26)$$

### 3.6 Convergence Test

To carry out the calculations using the CASTEP code based on density functional theory, it is essential that we determine the most appropriate basis set to use in the calculations. Then we optimize the structure of equiatomic TiNi in martensite compare the results obtained with earlier reported works.

For the CASTEP calculations, there are two important factors: cutoff energy and k-points which have a substantial effect on the numerical results. The convergence tests implemented center on these two factors. Generally, the higher these two parameters are, the more refined the results will be. However, with consideration of the computational costs, the objective is to select the lowest parameter values which are just able to provide the desired accuracies.

The convergence test is implemented on the B19' structure of equiatomic TiNi in martensite by calculating the free energies. When the difference between two continuous energy calculations is sufficiently small, it can be considered as converged. These two core parameters will be decided separately, where one parameter will be fixed the other is progressively increased.

Figure 3.3 shows the convergence characteristics of the free energy as the cutoff energy in the calculations was varied. During this convergence test, the k-points were set to  $22 \times 16 \times 16$  which is sufficiently high to ensure accuracy. From this figure, it is obvious that for cutoff energy above 1000 eV, the difference among free energies is less than 0.1 eV, even as the cutoff energy is increased to three times that of 1000 eV.

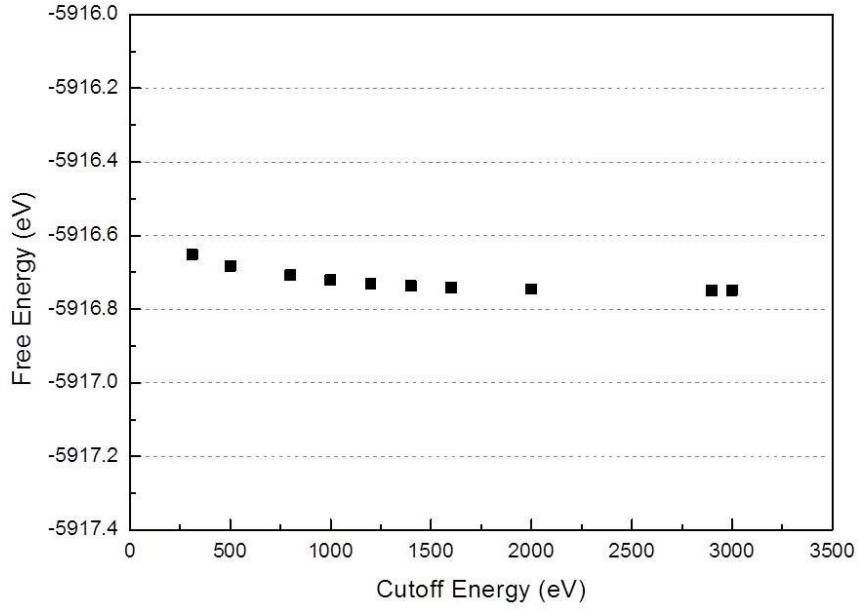


Figure 3.3 Convergence test for cutoff energy.

On the other hand, a cutoff energy of 500 eV was used in the calculations of reference [126], while cutoff energies of 500 eV and 1000 eV were used in reference [131]. Further, a cutoff energy of 310 eV was applied in the calculations of reference [137]. Thus, for the calculations carried out in this research, the cutoff energy was set to 1000 eV, which is sufficiently high to attain converged results.

The convergence test for the k-points is illustrated in Figure 3.4. For the convergence test of k-points, the cutoff energy was set to 1000 eV which has just been determined. From this figure, the conclusion can be drawn that for k-points above 150, the difference among free energies is lower than 0.01 eV, even though the k-points is increased to ten times that of 150. Consequently, in

this research, the  $9 \times 6 \times 6$  mesh was employed for the calculations, which means that 162 k-points were used to carry out all the calculations.

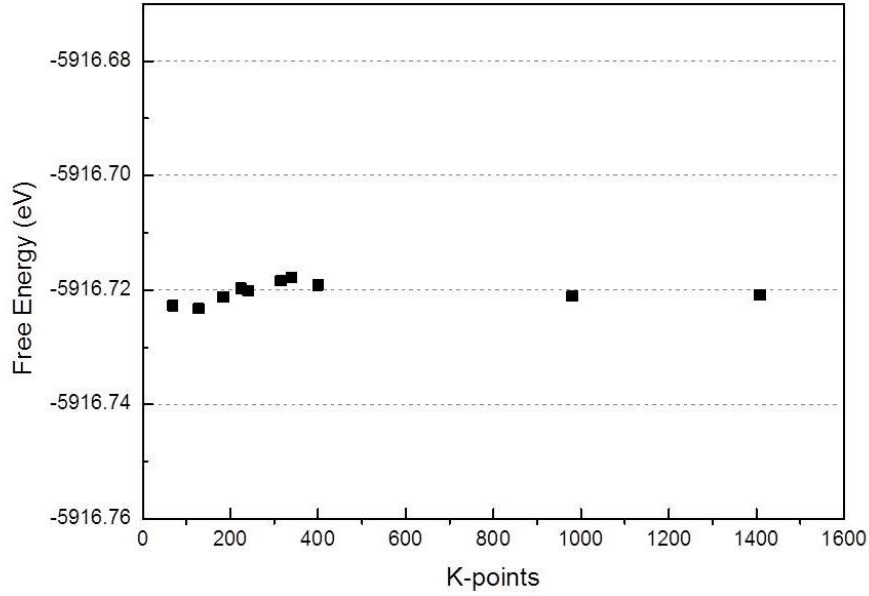


Figure 3.4 Convergence test for k-points.

### 3.7 Structure Optimization of Equiatomic TiNi in Martensite

In this section, the B19' structure of equiatomic TiNi in martensite is studied and the relevant calculations are performed. The crystal structures of B2 phase and B19' phase are shown in Figure 2.11 of Section 2.

During the optimization process, the calculated total energy for isolated Ti and Ni atoms are -1596.3451 eV/atom and -1347.3182 eV/atom, respectively. The optimized structure is not B19' but a new structure named base-centred orthorhombic (BCO) which is in line with the results of Huang et al. [126].

Moreover, we observed that if the k-points of the basis set are changed from  $9 \times 6 \times 6$  to  $9 \times 6 \times 5$ , the B19'' structure proposed by Vishnu et al. [136] appears. The structural parameters of BCO and B19'' are compared with prior values as shown in Table 3.1.

Table 3.1 Crystallographic data and atomic parameters of TiNi BCO and B19''.

Structures	$a$ (Å)	$b$ (Å)	$c$ (Å)	$\beta$ (°)	$X_{\text{Ni}}$	$Y_{\text{Ni}}$	$Z_{\text{Ni}}$	$X_{\text{Ti}}$	$Y_{\text{Ti}}$	$Z_{\text{Ti}}$
<b>BCO</b>	2.948	4.006	4.928	107.3	0.0852	0.25	0.6713	0.3579	0.25	0.2143
<b>BCO [126]</b>	2.940	3.997	4.936	107.0	0.086	0.25	0.673	0.358	0.25	0.214
<b>B19''</b>	2.946	4.021	4.809	102.9	0.068	0.25	0.672	0.383	0.25	0.216
<b>B19'' [136]</b>	2.923	4.042	4.801	102.44	0.064	0.25	0.079	0.115	0.25	0.037
<b>B19' [117]</b>	2.885	4.12	4.622	96.8	0.0525	0.25	0.693	0.4726	0.25	0.221

From Table 3.1, it can be observed that the present calculation outcomes agree well with the reported simulation results, which demonstrate that the present calculation methodology is appropriate, and that the present results are reliable. For the fractional atomic coordinates, certain evident errors are present in reference [136].

Figure 3.5 shows the change of the energy during the geometry optimization process. As mentioned in Section 3.5.1, geometry optimization is a procedure to minimize the potential energy of the system and to find a more stable state for a given structure. In this figure, the horizontal axis is the optimization step. It is evident that the energy decreases continuously with increasing the number of steps. In fact, the energy difference between the initial

structure and final state is quite small at about 0.16 eV. This means the original system is in a relative stable state, which is also corroborated by reported experimental observations. However, the monoclinic angle shows a noticeable increment after optimization.

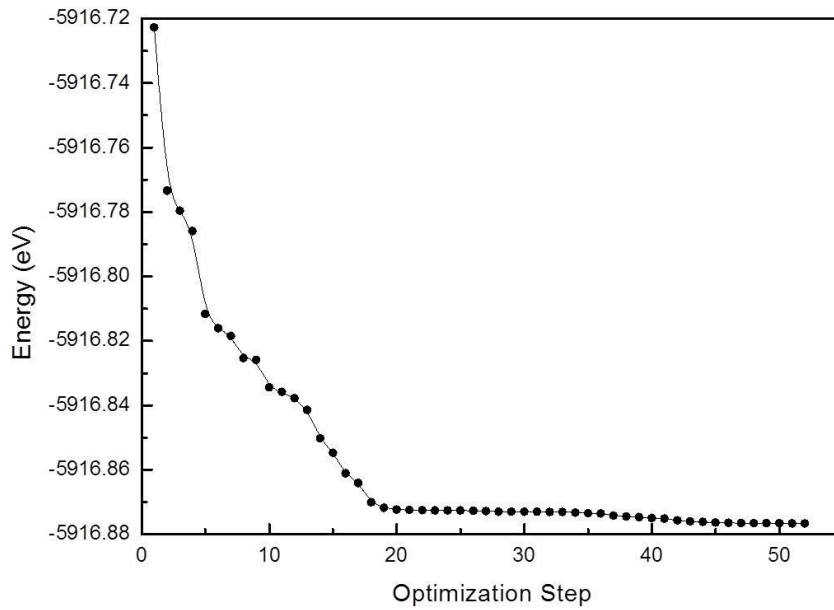


Figure 3.5 Energy change during optimization.

Figure 3.6 shows the optimization convergence characteristics during this procedure. From the top to the bottom, the four straight dash lines represent the convergence standards of maximum stress, maximum force, maximum displacement and energy change. The other four lines show the corresponding changes of these four standard lines, respectively.



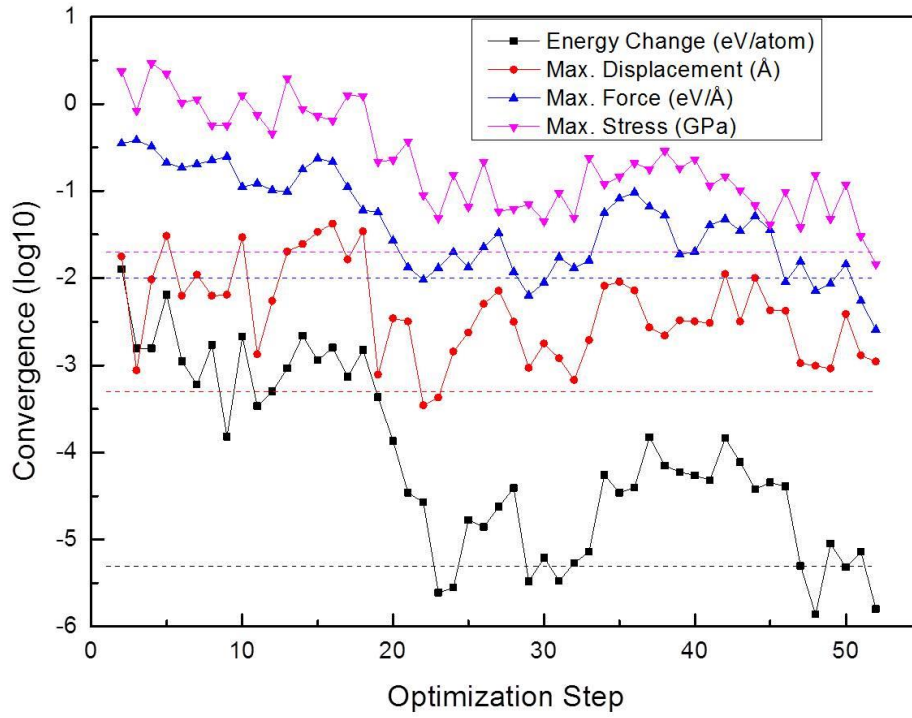


Figure 3.6 Illustration of optimization convergence.

From this figure, it can be seen that the geometry optimization is convergent. Following optimization, the final free energies of BCO and B19'' are -5916.8766 eV and -5916.8716 eV, respectively. The atomic Mulliken populations [163] are listed in Table 3.2. The density of states (DOS) and partial density of states (PDOS) are presented in Figure 3.7.

Table 3.2 Atomic Mulliken populations of BCO and B19''.

Species	s	p	d	f	Total	Charge (e)
BCO : Ti	2.27	6.78	2.58	0.00	11.63	0.37
BCO : Ni	0.60	1.08	8.70	0.00	10.37	-0.37
B19'' : Ti	2.27	6.78	2.59	0.00	11.64	0.36
B19'' : Ni	0.60	1.07	8.70	0.00	10.36	-0.36

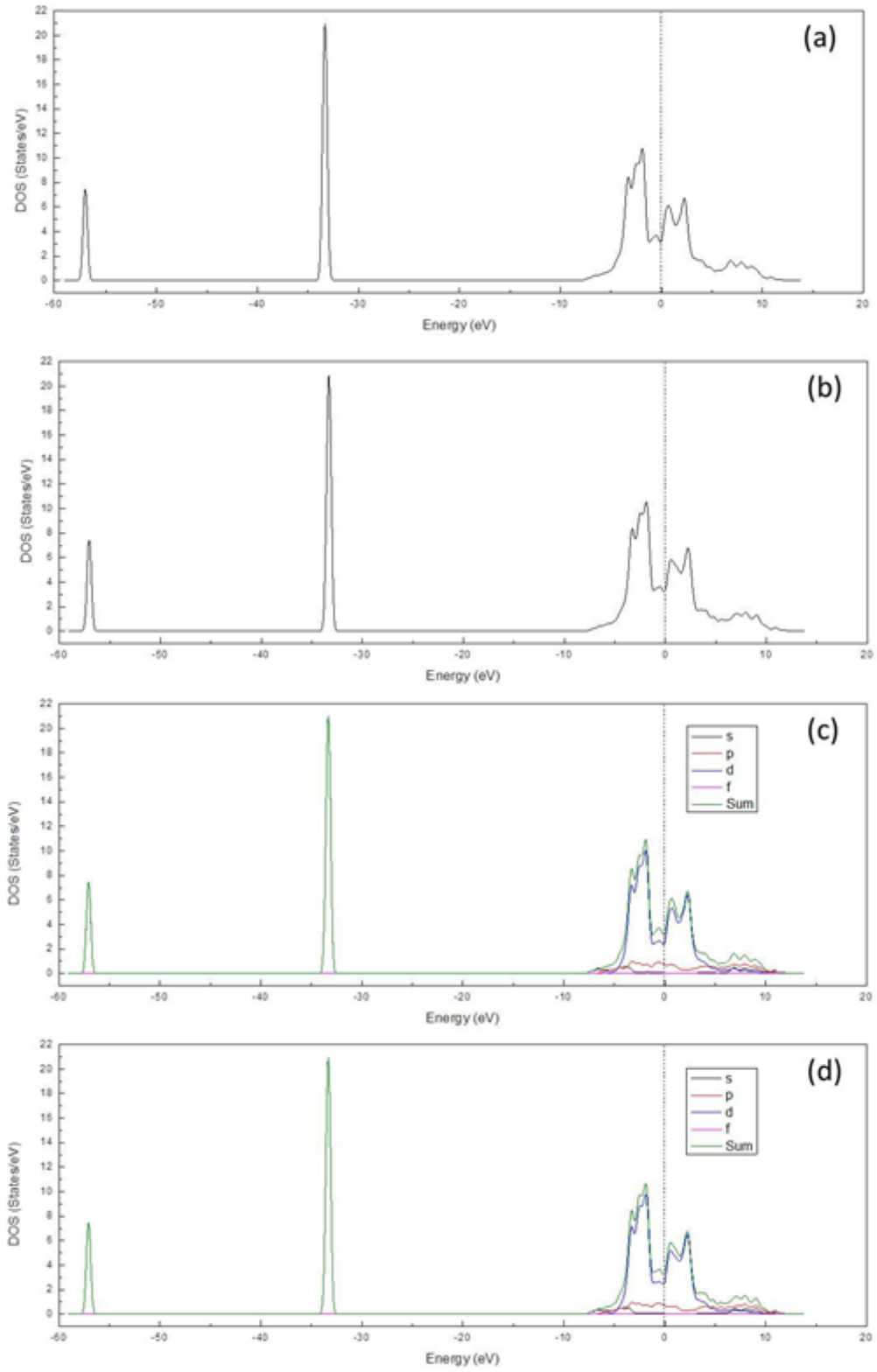


Figure 3.7 (a) DOS of BCO; (b) DOS of B19''; (c) PDOS of BCO; (d) PDOS of B19''.

Based on this comparison, it can be seen that these two structures, BCO and B19'', are actually quite similar. There are however, several slight distinctions between them. The final free energy of BCO is slightly lower than that of B19''. Table 3.2 indicates that in the BCO structure, the charge transfers are slightly higher than in B19'', from the Ti atoms to the Ni atoms. It can also be noted from Figure 3.7 that the DOS of BCO at the Fermi level are higher than that of B19''. All of these comparisons provide evidence that the BCO structure is more stable than B19'', but without any very obvious or distinct differences. As a consequence, the B19'' phase may be a transition phase between B19' and BCO, and plays a role in the stabilization of B19'structure.

## **Chapter 4 Calculated Results and Related Discussions**

In this chapter, the calculated results are presented and related discussions are conducted. The results on the effect of Cu content on the stable martensite crystal structures as well as the electronic structures; the effect of Cu content on the atomic positions as well as their displacements in martensite crystal structures; the effect of Cu content on the charge transfer are presented. The relationships among the charge transfer, the atomic displacement and the lattice properties are also discussed.

### **4.1 Background**

To date, automotive and aerospace industries require SMAs possessing high response frequency and high MT temperatures. Consequently, in order to alter the MT temperatures and to improve its physical and mechanical properties, various elements, such as Pt, Pd, Nb, Cu, etc., have been added to TiNi [10, 11, 15, 22, 26]. The developments, problems and prospects of high temperature shape memory alloys have been investigated and a comparison of high temperature shape memory behavior of ZrCu-based, TiNiZr and TiNiHf alloys has been conducted [167-169]. In order to achieve high response frequencies, TiNiCu alloys in which Cu substitutes for Ni, have been widely studied due to their narrow transformation temperature hysteresis [170-173]. These earlier efforts examined the effects of Cu content on transformation

temperature, microstructure, stress-strain characteristic and fatigue life [174-177], as well as applications as actuators [178, 179].

The lattice structures and lattice constants of solids are of fundamental importance in determining the phase transformation, microstructural morphologies, as well as other physical properties of SMAs. When Cu was added to TiNi binary alloy, understanding the changes of TiNiCu crystal structures at atomic level is of vital importance as it is very helpful for designing and developing new SMAs. Moreover, for in depth investigation of the effect of alloying on shape memory and superelastic effects, understanding how crystal structures change and the relationship between crystal structures and atomic displacements is of primary importance. Furthermore, in order to better understand the mechanism behind the crystal structures' changes and atomic displacements, a theoretical study on the charge transfer is indispensable. In this chapter, a computational method based in DFT is used to carry out all the related calculations.

## 4.2 Computational Methodology

The present calculations have been performed using the CASTEP code based on DFT with generalized gradient approximation (GGA) of Perdew, Burke and Ernzerhof (PBE) [160]. Following numerical convergence studies, the convergence tolerance of energy, maximum force, maximum stress and maximum displacement were set to be  $5.0 \times 10^{-6}$  eV/atom, 0.01 eV/Å, 0.02 GPa and  $5.0 \times 10^{-4}$  Å, respectively. The cutoff energy was chosen to be 1000 eV to

ensure a high degree of accuracy. The self-consistent field (SCF) tolerance was set to be  $5.0 \times 10^{-7}$  eV/atom and the smearing parameter of 0.05 eV was used. An appropriate k-points sampling of Monkhorst-Pack grid with  $9 \times 6 \times 6$  mesh was used to approximate the Brillouin zone. The ultrasoft pseudo-potentials were used to represent all ions. Pseudo atomic calculations performed for Ti, Ni and Cu are  $3s^2 3p^6 3d^2 4s^2$ ,  $3d^8 4s^2$  and  $3d^{10} 4s^1$ , respectively.

### **4.3 Effect of Cu Content on Crystal Structure of TiNiCu**

#### **SMA**s

Understanding the stable martensite crystal structure is a fundamental and essential issue for investigating the physics and chemistry properties of TiNiCu alloys. In order to understand the effect of Cu content on the crystal structures of TiNiCu alloys, in this section, we present a first principle investigation on the electronic structure and equilibrium structure of martensitic  $\text{Ti}_{50}\text{Ni}_{50-x}\text{Cu}_x$  ( $x = 0, 5, 12.5, 15, 18.75, 20, 25$ ). Favorable outcomes from this research will provide us with a useful tool to predict the crystal structures of SMA

s.

#### **4.3.1 Research Method**

The crystal structures found in TiNiCu alloys with different Cu content have been reported and they are listed in Table 4.1. The data of the B2, B19 and B19' phases were obtained from experimental observations and the BCO structure from reported computational results.

Table 4.1 Lattice parameters of B2, B19, B19' and BCO from previous experimental and theoretical work.

<b>Alloy</b>	<b>Phase</b>	<b><i>a</i> (Å)</b>	<b><i>b</i> (Å)</b>	<b><i>c</i> (Å)</b>	<b><i>β</i> (°)</b>	<b><i>Ref.</i></b>
<b>Ti<sub>50</sub>Ni<sub>50</sub></b>	BCO (Comp.)	2.94	3.997	4.936	107.0	[126]
<b>Ti<sub>50</sub>Ni<sub>50</sub></b>	B2-Cubic (Exp.)	3.05	--	--	--	[122, 123]
<b>Ti<sub>50</sub>Ni<sub>50</sub></b>	B19'-Monoclinic (Exp.)	2.89	4.12	4.62	96.5	[122, 123]
<b>Ti<sub>50</sub>Ni<sub>30</sub>Cu<sub>20</sub></b>	B19-Orthorhombic (Exp.)	2.88	4.28	4.52	--	[122, 123]

In the present calculations, all crystal structure optimizations were carried out starting from monoclinic structures. The atomic positions of Ni and Ti were taken as  $x = 0.0525$ ,  $y = 0.25$ ,  $z = 0.693$  and  $x = 0.4726$ ,  $y = 0.25$ ,  $z = 0.221$ , respectively [117]. In order to ensure the accuracy of the present results, all TiNiCu configurations were simulated in two different ways, namely Supercell Method (SM) and Virtual Crystal Method (VCM) and the numerical results were cross-checked. The structures used for SM are shown in Figure 4.1. On the other hand, the VCM is performed in which the ionic pseudopotential, i.e. Ni<sub>50-x</sub>Cu<sub>x</sub> is approximated by the weighted average of those of Ni and Cu in a unit cell, followed by conducting the usual ab initio self-consistent pseudopotential computation [180]. In a VCM simulation of Ti<sub>50</sub>Ni<sub>50-x</sub>Cu<sub>x</sub> one creates a new, virtual atom, which is a mixture of Ni and Cu with appropriate weights. Then, the actual calculation was performed on a unit cell with only the normal Ti atoms and the virtual Ni-Cu atoms.

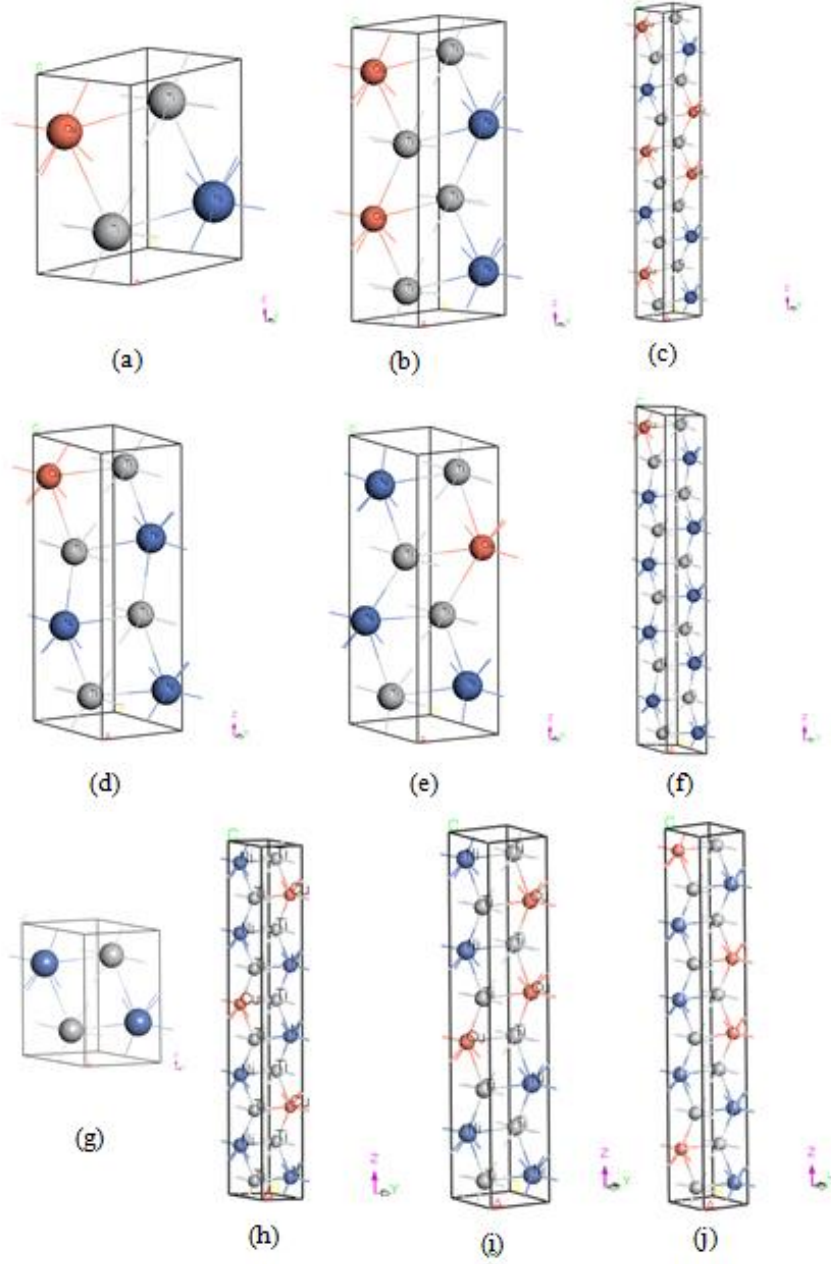


Figure 4.1 Initial unit cells and supercells of  $\text{Ti}_{50}\text{Ni}_{50-x}\text{Cu}_x$  (a) unit cell of  $\text{Ti}_{50}\text{Ni}_{25}\text{Cu}_{25}$  (b)  $1 \times 1 \times 2$  supercell of  $\text{Ti}_{50}\text{Ni}_{25}\text{Cu}_{25}$  (c)  $1 \times 1 \times 5$  supercell of  $\text{Ti}_{50}\text{Ni}_{25}\text{Cu}_{25}$  (d, e)  $1 \times 1 \times 2$  supercell of  $\text{Ti}_{50}\text{Ni}_{37.5}\text{Cu}_{12.5}$  (f)  $1 \times 1 \times 5$  supercell of  $\text{Ti}_{50}\text{Ni}_{45}\text{Cu}_5$  (g) unit cell of  $\text{Ti}_{50}\text{Ni}_{50}$  (h)  $1 \times 1 \times 5$  supercell of  $\text{Ti}_{50}\text{Ni}_{35}\text{Cu}_{15}$  (i)  $1 \times 1 \times 4$  supercell of  $\text{Ti}_{50}\text{Ni}_{31.25}\text{Cu}_{18.75}$  (j)  $1 \times 1 \times 5$  supercell of  $\text{Ti}_{50}\text{Ni}_{30}\text{Cu}_{20}$ .

In order to verify whether selection of initial number of unit cell in a supercell will affect the simulation results, supercells that consist of different



number of unit cells were test simulated. In particular, for the  $\text{Ti}_{50}\text{Ni}_{25}\text{Cu}_{25}$  alloy, a unit cell (Figure 4.1a),  $1 \times 1 \times 2$  supercell (Figure 4.1b), and  $1 \times 1 \times 5$  supercell (Figure 4.1c), were used to carry out the calculations to validate the influence of the number of unit cells on the calculated results of the lattice parameters.

In order to determine whether the positions of the Cu atoms in TiNiCu martensite structure influence the results, the positions of Cu atoms that substitute the Ni atoms in three different initial supercells, shown in Figure 4.1(a, b, c), were selected randomly. In addition, altering the Cu atom position in the same initial supercell (Figure 4.1d and Figure 4.1e) was also performed to further examine the effect of the Cu atom position on the results.

### 4.3.2 Results and Discussions

The calculated lattice parameters of  $\text{Ti}_{50}\text{Ni}_{45}\text{Cu}_5$ ,  $\text{Ti}_{50}\text{Ni}_{37.5}\text{Cu}_{12.5}$ ,  $\text{Ti}_{50}\text{Ni}_{35}\text{Cu}_{15}$ ,  $\text{Ti}_{50}\text{Ni}_{31.25}\text{Cu}_{18.75}$ ,  $\text{Ti}_{50}\text{Ni}_{30}\text{Cu}_{20}$  and  $\text{Ti}_{50}\text{Ni}_{25}\text{Cu}_{25}$  alloys are listed in Table 4.2 and Table 4.3. A comparison with previously reported data is also included.

Firstly, from the calculated results listed in Table 4.2, it can be clearly observed that the three sets of lattice parameters and free energy values of  $\text{Ti}_{50}\text{Ni}_{25}\text{Cu}_{25}$  obtained based on different initial supercells are practically identical. Hence, it can be concluded that both the positions of the Cu atoms and the number of unit cells have insignificant effect on the calculated results of lattice parameters and free energy. It can also be observed that the two

calculated results of  $\text{Ti}_{50}\text{Ni}_{37.5}\text{Cu}_{12.5}$  alloy are almost the same. This shows once again that the calculated lattice constants are independent of the atomic positions of Cu.

Table 4.2 Lattice parameters and free energy of  $\text{Ti}_{50}\text{Ni}_{50-x}\text{Cu}_x$  alloys obtained by the Supercell Method.

Alloys	No. of unit cell used	$a$ (Å)	$b$ (Å)	$c$ (Å)	$\beta$ (°)	Free Energy per unit cell (eV)	Volume per unit cell (Å <sup>3</sup> )
$\text{Ti}_{50}\text{Ni}_{45}\text{Cu}_5$	5	2.927	4.074	4.799	103.21	-5915.2012	55.7157
$\text{Ti}_{50}\text{Ni}_{37.5}\text{Cu}_{12.5}$	2	2.896	4.160	4.698	99.29	-5912.7079	55.8725
$\text{Ti}_{50}\text{Ni}_{37.5}\text{Cu}_{12.5}$	2	2.896	4.160	4.703	99.57	-5912.7082	55.8776
$\text{Ti}_{50}\text{Ni}_{35}\text{Cu}_{15}$	5	2.875	4.203	4.659	96.94	-5911.8798	55.8748
$\text{Ti}_{50}\text{Ni}_{31.25}\text{Cu}_{18.75}$	4	2.852	4.249	4.627	94.45	-5910.6293	55.9006
$\text{Ti}_{50}\text{Ni}_{30}\text{Cu}_{20}$	5	2.718	4.351	4.684	91.68	-5910.201	55.3664
$\text{Ti}_{50}\text{Ni}_{25}\text{Cu}_{25}$	1	2.684	4.396	4.702	90.09	-5908.5414	55.4807
$\text{Ti}_{50}\text{Ni}_{25}\text{Cu}_{25}$	2	2.685	4.394	4.701	89.98	-5908.5403	55.4722
$\text{Ti}_{50}\text{Ni}_{25}\text{Cu}_{25}$	5	2.726	4.358	4.691	91.58	-5908.5576	55.7136
$\text{Ti}_{50}\text{Ni}_{50}\text{-B19[122]}$	---	2.88	4.28	4.52	90	---	---
$\text{Ti}_{50}\text{Ni}_{50}\text{-B19'[123]}$	---	2.89	4.12	4.62	96.5	---	---
$\text{Ti}_{50}\text{Ni}_{50}\text{-BCO[126]}$	1	2.948	4.006	4.928	107.3	-5916.8766	55.5891
$\text{Ti}_{50}\text{Ni}_{50}\text{-B19''[134]}$	1	2.946	4.021	4.809	102.9	-5916.8716	55.5434

Table 4.3 Lattice parameters and free energy of  $\text{Ti}_{50}\text{Ni}_{50-x}\text{Cu}_x$  alloys obtained by the Virtual Crystal Method.

Alloys	$a$ (Å)	$b$ (Å)	$c$ (Å)	$\beta$ (°)	Free Energy per unit cell (eV)	Volume per unit cell (Å <sup>3</sup> )
$\text{Ti}_{50}\text{Ni}_{45}\text{Cu}_5$	2.949	4.044	4.780	101.417	-5896.4826	55.873802
$\text{Ti}_{50}\text{Ni}_{37.5}\text{Cu}_{12.5}$	2.948	4.087	4.732	99.463	-5875.1237	56.247562
$\text{Ti}_{50}\text{Ni}_{35}\text{Cu}_{15}$	2.894	4.1537	4.6956	97.190	-5870.0931	56.009568
$\text{Ti}_{50}\text{Ni}_{31.25}\text{Cu}_{18.75}$	2.8305	4.254	4.639	93.312	-5864.3132	55.771837
$\text{Ti}_{50}\text{Ni}_{30}\text{Cu}_{20}$	2.818	4.273	4.635	92.268	-5862.8376	55.768346
$\text{Ti}_{50}\text{Ni}_{27.5}\text{Cu}_{22.5}$	2.804	4.2946	4.637	91.23354	-5860.54053	55.827830
$\text{Ti}_{50}\text{Ni}_{25}\text{Cu}_{25}$	2.789	4.314	4.645	90.313	-5859.1065	55.887204
$\text{Ti}_{50}\text{Ni}_{50}\text{-B19[122]}$	2.88	4.28	4.52	90	---	---
$\text{Ti}_{50}\text{Ni}_{50}\text{-B19'[123]}$	2.89	4.12	4.62	96.5	---	---
$\text{Ti}_{50}\text{Ni}_{50}\text{-BCO[126]}$	2.948	4.006	4.928	107.3	-5916.8766	55.5891
$\text{Ti}_{50}\text{Ni}_{50}\text{-B19''[134]}$	2.946	4.021	4.809	102.9	-5916.8716	55.5434

Secondly, it can be found from Table 4.2 and Table 4.3 that the present calculation results are consistent with earlier reported experimental data. Thus, we can infer that the present structures used to carry out the calculations are reasonable and the results are accurate and reliable. For  $\text{Ti}_{50}\text{Ni}_{45}\text{Cu}_5$ ,  $\text{Ti}_{50}\text{Ni}_{37.5}\text{Cu}_{12.5}$ ,  $\text{Ti}_{50}\text{Ni}_{35}\text{Cu}_{15}$  and  $\text{Ti}_{50}\text{Ni}_{31.25}\text{Cu}_{18.75}$ , the stable martensite B19' phase is of monoclinic structure, while for  $\text{Ti}_{50}\text{Ni}_{30}\text{Cu}_{20}$  and  $\text{Ti}_{50}\text{Ni}_{25}\text{Cu}_{25}$ , they are the B19 phase with orthorhombic structure, which agree well with experimental observations. The lattice constants of  $\text{Ti}_{50}\text{Ni}_{45}\text{Cu}_5$  are very close

to those of the B19'' structure reported in an earlier work [134], further indicating the likelihood of existence of such structure in TiNi-based SMAs. In addition, the calculated lattice parameters of  $\text{Ti}_{50}\text{Ni}_{37.5}\text{Cu}_{12.5}$  are in good agreement with the experimental data of the B19' structure, except that there is a  $3^\circ$  difference in monoclinic angles.

Thirdly, the free energy increases with increasing Cu substitution, meaning that with increasing Cu content in TiNiCu alloys, the monoclinic martensite structure becomes less stable.

The calculated Mulliken charge transfer as a function of Cu content, are presented in Table 4.4. The densities of states (DOS) of TiNiCu alloys are shown in Figure 4.2.

Table 4.4 Calculated charge transfer per atom in TiNiCu alloys.

Alloys	Charges ( <i>e</i> )		
	Ti	Ni	Cu
$\text{Ti}_{50}\text{Ni}_{50}$	0.365	-0.365	---
$\text{Ti}_{50}\text{Ni}_{45}\text{Cu}_5$	0.399	-0.348	-0.85
$\text{Ti}_{50}\text{Ni}_{37.5}\text{Cu}_{12.5}$	0.445	-0.323	-0.82
$\text{Ti}_{50}\text{Ni}_{35}\text{Cu}_{15}$	0.464	-0.3157	-0.81
$\text{Ti}_{50}\text{Ni}_{31.25}\text{Cu}_{18.75}$	0.495	-0.294	-0.83
$\text{Ti}_{50}\text{Ni}_{30}\text{Cu}_{20}$	0.496	-0.273	-0.83
$\text{Ti}_{50}\text{Ni}_{25}\text{Cu}_{25}$	0.54	-0.23	-0.85

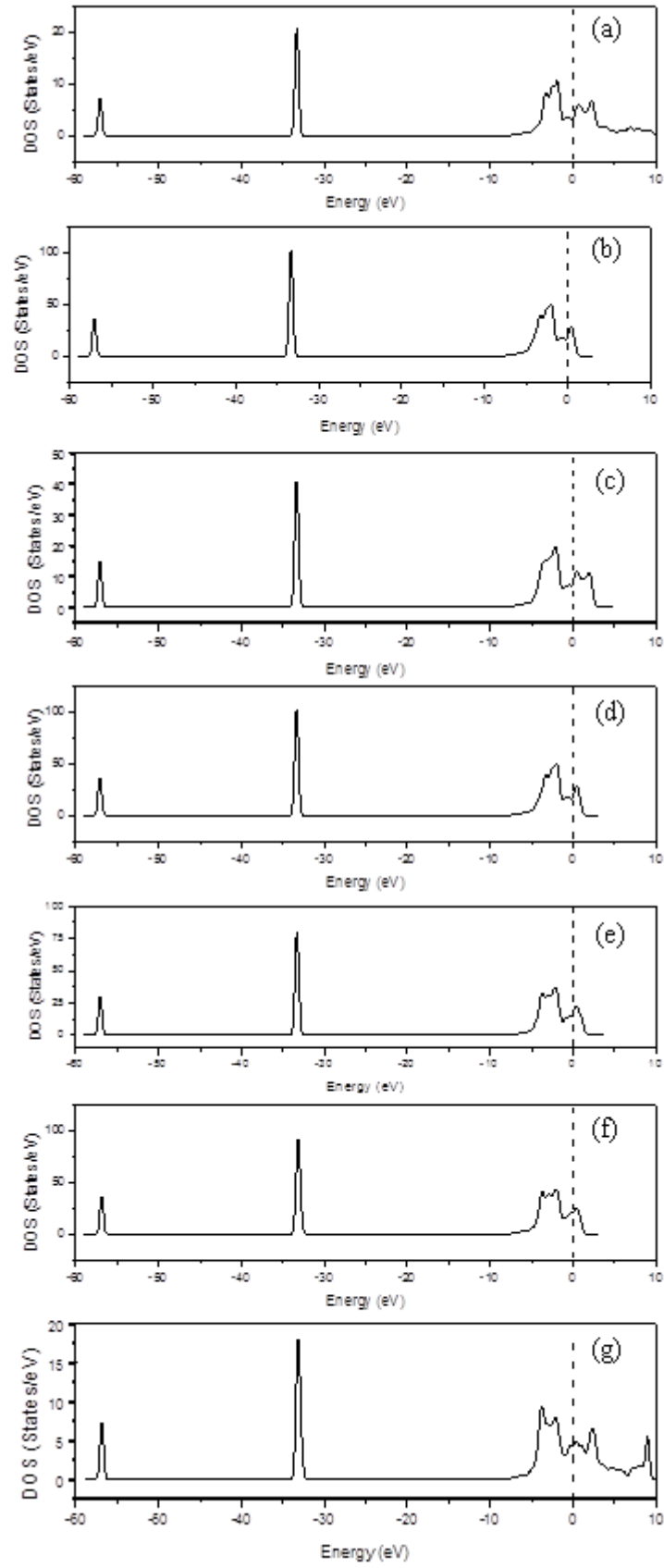


Figure 4.2 Density of states (DOS) for (a)  $\text{Ti}_{50}\text{Ni}_{50}$ ; (b)  $\text{Ti}_{50}\text{Ni}_{45}\text{Cu}_5$ ; (c)  $\text{Ti}_{50}\text{Ni}_{37.5}\text{Cu}_{12.5}$ ; (d)  $\text{Ti}_{50}\text{Ni}_{35}\text{Cu}_{15}$ ; (e)  $\text{Ti}_{50}\text{Ni}_{31.25}\text{Cu}_{18.75}$ ; (f)  $\text{Ti}_{50}\text{Ni}_{30}\text{Cu}_{20}$  and (g)  $\text{Ti}_{50}\text{Ni}_{25}\text{Cu}_{25}$ .

As presented in Table 4.4, in comparison with equiatomic TiNi binary alloy, more electrons escape from the Ti atoms with increasing Cu content. As the ability of Cu atoms to attract electrons is stronger than Ni [71], less charge transfer to Ni atoms than to Cu atoms was observed.

Naturally, since the electron DOS depends mainly on the local atomic environment [181], alloys having the same amount of Ti should have similar electron DOS. In binary intermetallic compounds, high DOS at Fermi level has been considered to be related to the structure instability. However, Ravi *et al.* [182] stated that this may not be true for ternary systems. In the present research, it has been observed that for TiNiCu ternary alloys, high DOS at Fermi level is related to the structure instability. From our calculations, the substitution of Ni by Cu seems to increase the DOS at Fermi level. By comparing the free energies of TiNiCu alloys, it shows that with increasing Cu content, the free energy increases, leading to instability of the TiNiCu martensite monoclinic structure. For binary TiNi, the martensite crystal structure is monoclinic. For  $\text{Ti}_{50}\text{Ni}_{45}\text{Cu}_5$  and  $\text{Ti}_{50}\text{Ni}_{37.5}\text{Cu}_{12.5}$ , although the crystal structures are still monoclinic, the monoclinic angle has changed. However, in  $\text{Ti}_{50}\text{Ni}_{30}\text{Cu}_{20}$  and  $\text{Ti}_{50}\text{Ni}_{25}\text{Cu}_{25}$  alloys, the stable martensite crystal structures become orthorhombic. These results suggest that there is a relationship between the DOS at Fermi level and the equilibrium crystal structure.

In Figure 4.3, the lattice parameters, as a function of Cu content in TiNiCu alloys, obtained through both SM and VCM, are presented. It can be seen that the lattice parameters  $a$  and  $c$  decrease with increasing Cu content, while the lattice parameter  $b$  increases. The two computational methods used in the present research yield results which are very similar and the trends are identical. It can be observed that Cu content has significant effect on the lattice parameters of TiNiCu alloys with Cu content less than 25 at%.

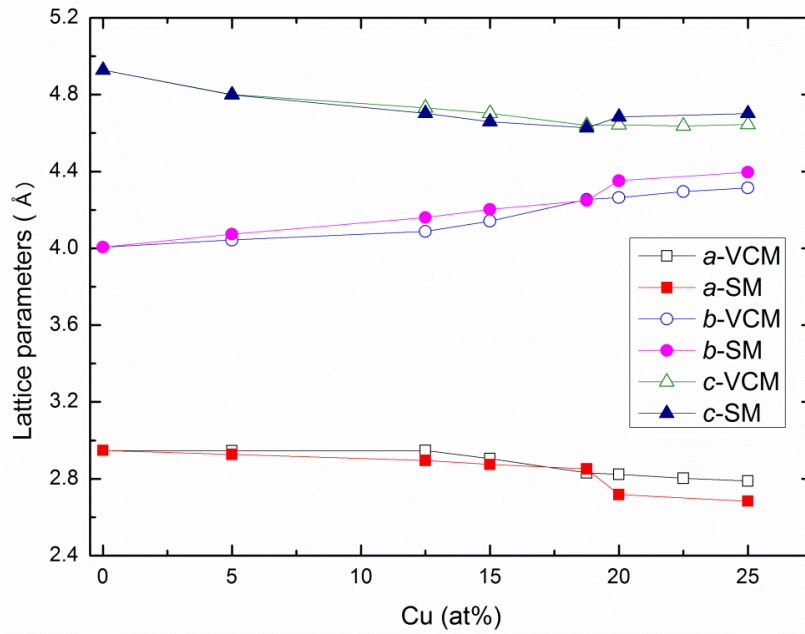


Figure 4.3 Variation of lattice parameters with Cu content.

In Figure 4.4, we present the monoclinic angle ( $\beta$ ) and unit cell volume as a function of Cu content. The results obtained through both SM and VCM are listed and compared. The unit cell volumes of the TiNiCu alloys have very slight variations with varying Cu content. The binary TiNi alloy can be

considered as a TiNiCu alloy containing zero at% Cu. The unit cell volume of an intermetallic crystal is controlled by the bond lengths, namely, it is controlled by both the size of the atoms and the number of valence electrons of the materials [183]. The atomic radii of Ni, Ti and Cu are 1.29 Å, 1.45 Å and 1.28 Å, respectively. The valence electrons are electrons in the outermost principal quantum level of an atom which means the  $s$  and  $d$  electrons make the most contribution to the valence electrons [184]. For transition metals, these  $s$  and  $d$  electrons are generally considered as the valence electrons.

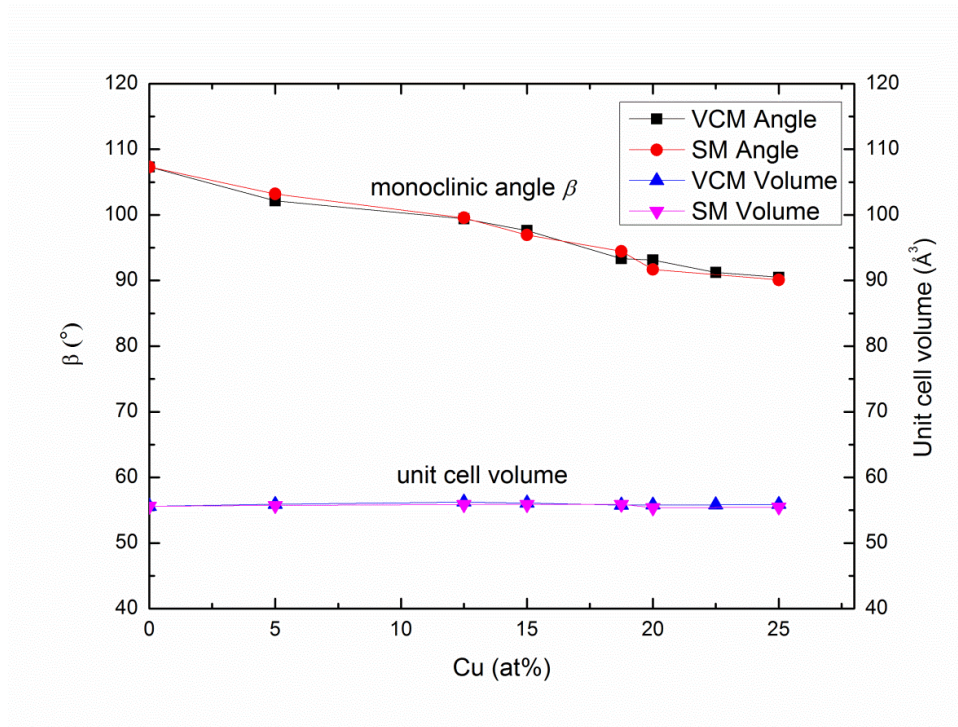


Figure 4.4 Variation of unit cell volume and monoclinic angle with Cu content.

In the present simulations, the electronic configurations adopted for Ni, Ti and Cu are  $3d^8 4s^2$ ,  $3s^2 3p^6 3d^2 4s^2$  and  $3d^{10} 4s^1$ , respectively. Thus, the numbers of valence electrons ( $e_v$ ) of these elements are  $e_v^{Ni} = 10$ ,  $e_v^{Ti} = 4$  and  $e_v^{Cu} = 11$ .



For ternary TiNiCu alloys, the number of valence electrons per atom can be defined based on the atomic fraction of the elements in the alloy [184]. The equation used to determine the number of valence electrons per atom of TiNiCu is:

$$\frac{e_v}{a} = f_{Ni}e_v^{Ni} + f_{Ti}e_v^{Ti} + f_{Cu}e_v^{Cu} \quad (4.1)$$

where  $f_{Ni}$ ,  $f_{Ti}$  and  $f_{Cu}$  are the atomic fractions of elements in the alloy for Ni, Ti and Cu, respectively. Similarly,  $e_v^{Ni}$ ,  $e_v^{Ti}$  and  $e_v^{Cu}$  are the number of valence electrons of Ni, Ti and Cu, respectively. As the number of valence electrons of Cu is slightly higher than Ni, the number of valence electrons per atom of TiNiCu increases slightly with increasing Cu content.

Since both the atomic radius and the number of valence electrons of Cu are quite similar to those of Ni, the substitution of Cu for Ni has minimal effect on the unit cell volume of the TiNiCu martensite.

From Figure 4.4, we can also note that the monoclinic angle ( $\beta$ ) decreases with increasing Cu content consistently. When Cu content is between 0 at% and 18.75 at%, a monoclinic crystal structure presents. However, when the Cu content is increased to 20 at%, an orthorhombic structure is formed.

### 4.3.3 Summary

The present section has studied the crystal structure, electronic structure and stable martensite crystal structure of  $\text{Ti}_{50}\text{Ni}_{50-x}\text{Cu}_x$  ( $x = 0, 5, 12.5, 15, 18.75, 20, 25$ ) alloys based on first-principle calculations. From the crystal structure optimizations of TiNiCu martensite with different amounts of Cu substituting Ni, the following conclusions can be drawn:

As a result of Cu addition to TiNi, the martensite lattice parameters  $a$  and  $c$  and the monoclinic angle decrease, whereas the lattice parameter  $b$  increases with increasing Cu content. When Cu content reaches 20 at%, the monoclinic martensite crystal structure becomes unstable and an orthorhombic crystal structure is formed. This computational outcome agrees well with experimental observations.

With increasing Cu content, more electrons escape from the Ti atoms. As the Cu atoms attract more electrons as compared to the Ni atoms, fewer charge transfer from Ti to Ni occurs as compared to that in binary TiNi alloy. Since both the atomic radius and the number of valence electrons of Cu are quite similar to those of Ni, the unit cell volumes of TiNiCu martensite structures vary slightly with different Cu content.

Due to the lower free energy, the base-centred orthorhombic (BCO) structure is more stable than the B19'' structure. The B19'' phase can be considered as a transition phase between B19' and BCO and might play a role

in the stabilization of the B19' structure, based on observations of the monoclinic angle.

## **4.4 Effect of Cu Content on Atom Positions of TiNiCu SMAs**

In order to effectively design SMAs with required transformation hysteresis, understanding the atomic displacement and subsequent crystal structure transition as a result of alloying is of primary importance. In Section 4.3, the stable martensite structures of TiNiCu alloys have been investigated. However, the mechanism of Cu addition in modifying the martensite crystal structure is still not clearly understood. In order to investigate the mechanism of how Cu content affects martensite crystal structures of TiNiCu alloys, in this section, a first principle investigation on the atomic displacement of martensitic  $\text{Ti}_{50}\text{Ni}_{50-x}\text{Cu}_x$  ( $x = 0, 5, 12.5, 15, 18.75, 20, 25$ ) alloys is performed.

### **4.4.1 Research Method**

The martensite crystal structures of TiNiCu alloys with different Cu contents used and compared in this chapter are listed in Table 4.5. The B19 and B19' phases were observed in experiments, while the BCO structure was obtained only from computational calculations. In the present calculations, all initial crystal structures were set to monoclinic structures, i.e. B19' phase. The

original atomic positions of Ni and Ti were taken as  $x = 0.0525$ ,  $y = 0.25$ ,  $z = 0.693$  and  $x = 0.4726$ ,  $y = 0.25$ ,  $z = 0.221$ , respectively.

Table 4.5 Lattice parameters of, B19, B19' and BCO from earlier experimental and theoretical works.

Alloy	Phase	$a$ (Å)	$b$ (Å)	$c$ (Å)	$\beta$ (°)	Ref.
<b>Ti<sub>50</sub>Ni<sub>50</sub></b>	BCO (Comp.)	2.94	3.997	4.936	107.0	[126]
<b>Ti<sub>50</sub>Ni<sub>50</sub></b>	B19'-Monoclinic (Exp.)	2.89	4.12	4.62	96.5	[122, 123]
<b>Ti<sub>50</sub>Ni<sub>30</sub>Cu<sub>20</sub></b>	B19-Orthorhombic (Exp.)	2.88	4.28	4.52	--	[122, 123]

In order to obtain and visualize the atomic displacements in TiNiCu alloys with different Cu content, the same unit cell has been used and all TiNiCu initial structures were optimized by the Virtual Crystal Method (VCM). The unit cells of B19' and B19 martensite structures are shown in Figure 4.5, in which four atoms were indicated for each unit cell.

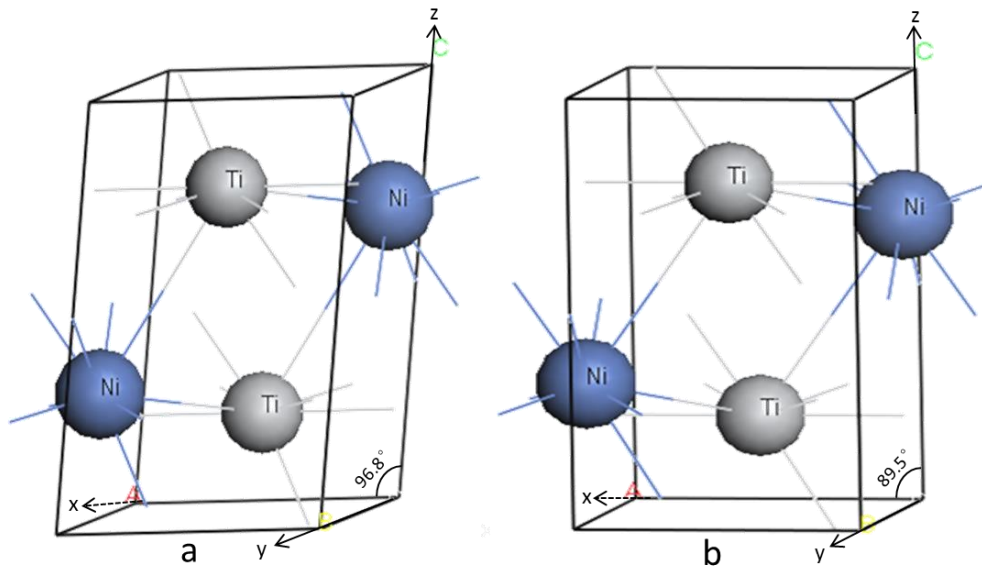


Figure 4.5 Schematic of the unit cell of (a) B19' martensite structure, and (b) B19 martensite structure.

#### 4.4.2 Results and Discussions

The calculated atomic positions of Ti and Ni/Cu as a result of Cu addition from VCM and SM are listed in Table 4.6, Table 4.8 and Table 4.7, Table 4.9, respectively, in which reported experimental data are also included. The calculated results from two methods are compared and cross-checked.

Table 4.6 Atomic coordinates of Ti and Ni/Cu in TiNiCu alloys ( $y = 0.25$ ) from VCM.

Alloys	Atomic coordinate (Ni/Cu)			Atomic coordinate (Ti)		
	$x$	$y$	$z$	$x$	$y$	$z$
<b>Ti<sub>50</sub>Ni<sub>50</sub> (Exp.)</b>	0.0525	0.25	0.693	0.4726	0.25	0.221
<b>Ti<sub>50</sub>Ni<sub>50</sub></b>	0.0898	0.25	0.671	0.3518	0.25	0.215
<b>Ti<sub>50</sub>Ni<sub>45</sub>Cu<sub>5</sub></b>	0.0639	0.25	0.670	0.3869	0.25	0.215
<b>Ti<sub>50</sub>Ni<sub>37.5</sub>Cu<sub>12.5</sub></b>	0.0471	0.25	0.669	0.4026	0.25	0.213
<b>Ti<sub>50</sub>Ni<sub>35</sub>Cu<sub>15</sub></b>	0.0349	0.25	0.671	0.4166	0.25	0.212
<b>Ti<sub>50</sub>Ni<sub>31.25</sub>Cu<sub>18.7</sub></b>	0.0126	0.25	0.677	0.4608	0.25	0.213
<b>Ti<sub>50</sub>Ni<sub>30</sub>Cu<sub>20</sub></b>	0.0116	0.25	0.677	0.4620	0.25	0.213
<b>Ti<sub>50</sub>Ni<sub>25</sub>Cu<sub>25</sub></b>	-0.0019	0.25	0.679	0.5065	0.25	0.212

Table 4.7 Atomic coordinates of Ti and Ni/Cu in TiNiCu alloys ( $y = 0.25$ ) from SM.

Alloys	Atomic coordinate (Ni/Cu)			Atomic coordinate (Ti)		
	$x$	$y$	$z$	$x$	$y$	$z$
<b>Ti<sub>50</sub>Ni<sub>50</sub> (Exp.)</b>	0.0525	0.25	0.693	0.4726	0.25	0.221
<b>Ti<sub>50</sub>Ni<sub>50</sub> (Comp.)</b>	0.0898	0.25	0.671	0.3518	0.25	0.215
<b>Ti<sub>50</sub>Ni<sub>45</sub>Cu<sub>5</sub></b>	0.0660	0.25	0.669	0.3852	0.25	0.228
<b>Ti<sub>50</sub>Ni<sub>37.5</sub>Cu<sub>12.5</sub></b>	0.0469	0.25	0.691	0.4188	0.25	0.215
<b>Ti<sub>50</sub>Ni<sub>35</sub>Cu<sub>15</sub></b>	0.0325	0.25	0.683	0.4396	0.25	0.208
<b>Ti<sub>50</sub>Ni<sub>31.25</sub>Cu<sub>18.75</sub></b>	0.0117	0.25	0.679	0.4627	0.25	0.216
<b>Ti<sub>50</sub>Ni<sub>30</sub>Cu<sub>20</sub></b>	0.0057	0.25	0.684	0.4780	0.25	0.213
<b>Ti<sub>50</sub>Ni<sub>25</sub>Cu<sub>25</sub></b>	-0.0002	0.25	0.682	0.5003	0.25	0.213

Table 4.8 Atomic coordinates of Ti and Ni/Cu in TiNiCu alloys ( $y = 0.75$ ) from VCM.

Alloys	Atomic coordinate (Ni/Cu)			Atomic coordinate (Ti)		
	$x$	$y$	$z$	$x$	$y$	$z$
<b>Ti<sub>50</sub>Ni<sub>50</sub> (Exp.)</b>	0.9475	0.75	0.307	0.5274	0.75	0.779
<b>Ti<sub>50</sub>Ni<sub>50</sub></b>	0.9147	0.75	0.329	0.6421	0.75	0.786
<b>Ti<sub>50</sub>Ni<sub>45</sub>Cu<sub>5</sub></b>	0.9360	0.75	0.330	0.6130	0.75	0.785
<b>Ti<sub>50</sub>Ni<sub>37.5</sub>Cu<sub>12.5</sub></b>	0.9529	0.75	0.331	0.5973	0.75	0.787
<b>Ti<sub>50</sub>Ni<sub>35</sub>Cu<sub>15</sub></b>	0.9651	0.75	0.330	0.5834	0.75	0.788
<b>Ti<sub>50</sub>Ni<sub>31.25</sub>Cu<sub>18.7</sub></b>	0.9814	0.75	0.323	0.5392	0.75	0.787
<b>Ti<sub>50</sub>Ni<sub>30</sub>Cu<sub>20</sub></b>	0.9883	0.75	0.323	0.5380	0.75	0.787
<b>Ti<sub>50</sub>Ni<sub>25</sub>Cu<sub>25</sub></b>	1.0079	0.75	0.321	0.4935	0.75	0.788

Table 4.9 Atomic coordinates of Ti and Ni/Cu in TiNiCu alloys ( $y = 0.75$ ) from SM.

Alloys	Atomic coordinate (Ni/Cu)			Atomic coordinate (Ti)		
	$x$	$y$	$z$	$x$	$y$	$z$
<b>Ti<sub>50</sub>Ni<sub>50</sub> (Exp.)</b>	0.9475	0.75	0.307	0.5274	0.75	0.779
<b>Ti<sub>50</sub>Ni<sub>50</sub></b>	0.9147	0.75	0.329	0.6421	0.75	0.786
<b>Ti<sub>50</sub>Ni<sub>45</sub>Cu<sub>5</sub></b>	0.9340	0.75	0.331	0.6148	0.75	0.772
<b>Ti<sub>50</sub>Ni<sub>37.5</sub>Cu<sub>12.5</sub></b>	0.9531	0.75	0.309	0.5812	0.75	0.785
<b>Ti<sub>50</sub>Ni<sub>35</sub>Cu<sub>15</sub></b>	0.9675	0.75	0.317	0.5604	0.75	0.792
<b>Ti<sub>50</sub>Ni<sub>31.25</sub>Cu<sub>18.7</sub></b>	0.9883	0.75	0.321	0.5373	0.75	0.784
<b>Ti<sub>50</sub>Ni<sub>30</sub>Cu<sub>20</sub></b>	0.9943	0.75	0.316	0.5220	0.75	0.787
<b>Ti<sub>50</sub>Ni<sub>25</sub>Cu<sub>25</sub></b>	1.0002	0.75	0.318	0.4997	0.75	0.787

From the calculated results listed in Table 4.6, Table 4.8, Table 4.7 and Table 4.9, it can be observed that the two computational methods used in the present research yield similar results and the trends are identical, which implies either of the two methods can be used to carry out the calculations. Specifically, the atomic coordinates from the SM method are the average values of the

corresponding atoms while those from VCM can be obtained directly. With higher accuracy, the results from the VCM method were used to visualize the atomic displacements in the unit cell. From the four tables, it can be clearly observed that in the  $x$ -direction, the displacements of Ni/Cu and Ti atoms are clearly evident. Increasing Cu content leads to a displacement of Ni/Cu atom along the  $[\bar{1}00]$  direction and Ti atom in the  $[100]$  direction. Both Ni/Cu and Ti atoms remain unshifted in the  $[010]$  direction with increasing Cu content. The displacements of Ni/Cu and Ti atoms along the  $[001]$  direction are relatively small in all the alloys considered here.

Since the Ni/Cu and Ti atoms remain unchanged along the  $[010]$  direction, it can be indicated that all the atomic displacements have occurred within the  $(010)$  plane. The schematic projections of the crystal structures along the  $y$ -axis for TiNiCu alloys containing different Cu contents are illustrated in Figure 4.6. The positions of Ni/Cu site (blue) and Ti site (grey) along ' $a$ ' and ' $c$ ' lattice parameters with respect to the binary alloy are clearly depicted. The dashed circles represent the original positions of Ni and Ti atoms in the computational  $\text{Ti}_{50}\text{Ni}_{50}$  B19' structure.

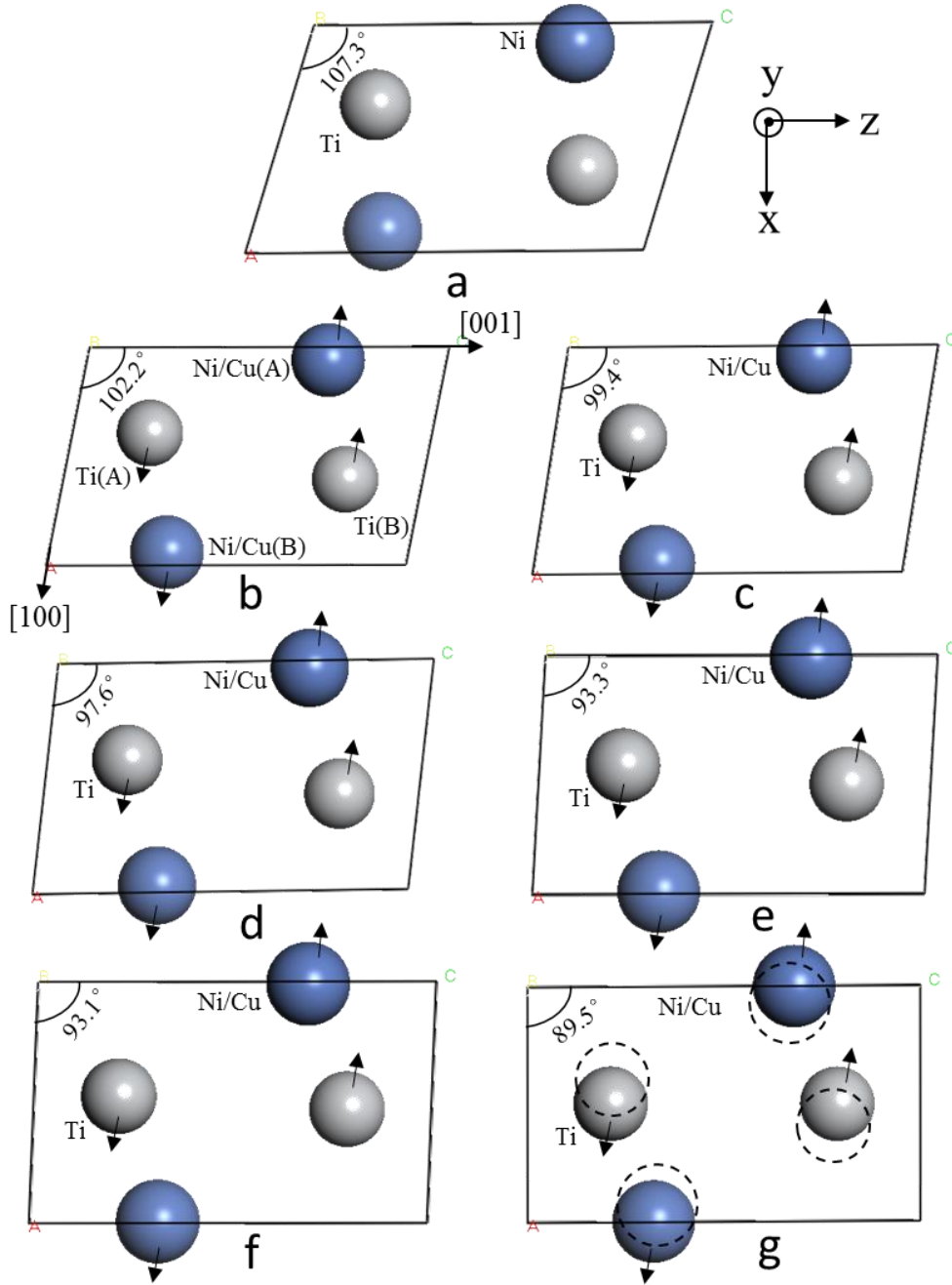


Figure 4.6 Projections of the martensite crystal structures along  $\langle 010 \rangle$  direction of (a) binary  $\text{Ti}_{50}\text{Ni}_{50}$ ; (b)  $\text{Ti}_{50}\text{Ni}_{45}\text{Cu}_5$ ; (c)  $\text{Ti}_{50}\text{Ni}_{37.5}\text{Cu}_{12.5}$ ; (d)  $\text{Ti}_{50}\text{Ni}_{35}\text{Cu}_{15}$ ; (e)  $\text{Ti}_{50}\text{Ni}_{31.25}\text{Cu}_{18.75}$ ; (f)  $\text{Ti}_{50}\text{Ni}_{30}\text{Cu}_{20}$  and (g)  $\text{Ti}_{50}\text{Ni}_{25}\text{Cu}_{25}$ , comparing the typical relative average positions of Ni site (blue) and Ti site (grey) along 'a' and 'c' lattice parameters with respect to the binary alloy.



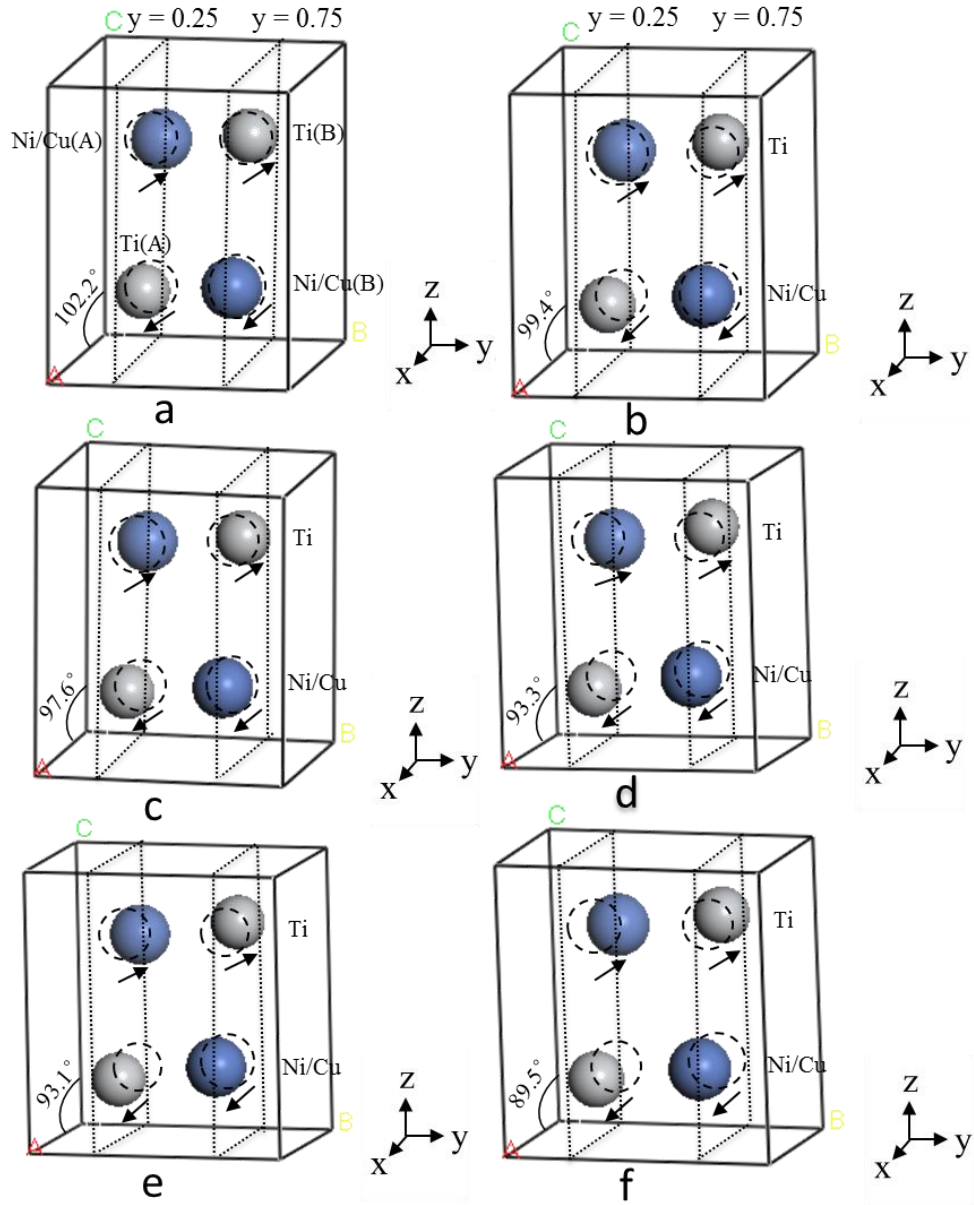


Figure 4.7 3-D diagrams showing the atomic positions of (a)  $\text{Ti}_{50}\text{Ni}_{45}\text{Cu}_5$ ; (b)  $\text{Ti}_{50}\text{Ni}_{37.5}\text{Cu}_{12.5}$ ; (c)  $\text{Ti}_{50}\text{Ni}_{35}\text{Cu}_{15}$ ; (d)  $\text{Ti}_{50}\text{Ni}_{31.25}\text{Cu}_{18.75}$ ; (e)  $\text{Ti}_{50}\text{Ni}_{30}\text{Cu}_{20}$  and (f)  $\text{Ti}_{50}\text{Ni}_{25}\text{Cu}_{25}$ .

The three-dimensional (3D) diagrams are shown in Figure 4.7. From this figure, it is obvious that all the atomic displacements occurred within the (010) planes, i.e. (010) plane at  $y = 0.25$  (as listed in Table 4.6) and (010) plane at  $y = 0.75$  (as listed in Table 4.8) respectively. We label the atoms within the (010)

plane at  $y = 0.25$  as Ni/Cu(A) and Ti(A), and the atoms within the (010) plane at  $y = 0.75$  as Ni/Cu(B) and Ti(B), respectively. As shown in Figure 4.6, the Ti atoms on the left and right sides are Ti(A) and Ti(B), respectively, while the Ni/Cu atoms in upper and lower positions are Ni/Cu(A) and Ni/Cu(B), respectively. The monoclinic angles and the atom displacement directions are indicated in these two figures.

The crystal structure is determined by the atomic arrangements in crystalline solids. From Figure 4.6 and Figure 4.7, we observe that along the  $x$ -axis, the two Ti atoms shifted in the opposite directions, as did the two Ni/Cu atoms. With increasing Cu content, the distance between the two Ni/Cu atoms increases along the  $x$ -axis, while that between the Ti atoms decreases. Specifically for the Ni/Cu atom, when Cu content reaches 25 at%, the  $x$ -parameter is near zero. This form of atomic displacements within the (010) plane leads to a rotation of the (100) plane.

As shown in Figure 4.8, from  $\text{Ti}_{50}\text{Ni}_{50}$  to  $\text{Ti}_{50}\text{Ni}_{25}\text{Cu}_{25}$ , the (010) and (001) planes remain unchanged. However, the (100) plane rotates along the [010] direction, leading to a decrease in monoclinic angle. As a result, the crystal structure changes from monoclinic (B19') to orthorhombic (B19).

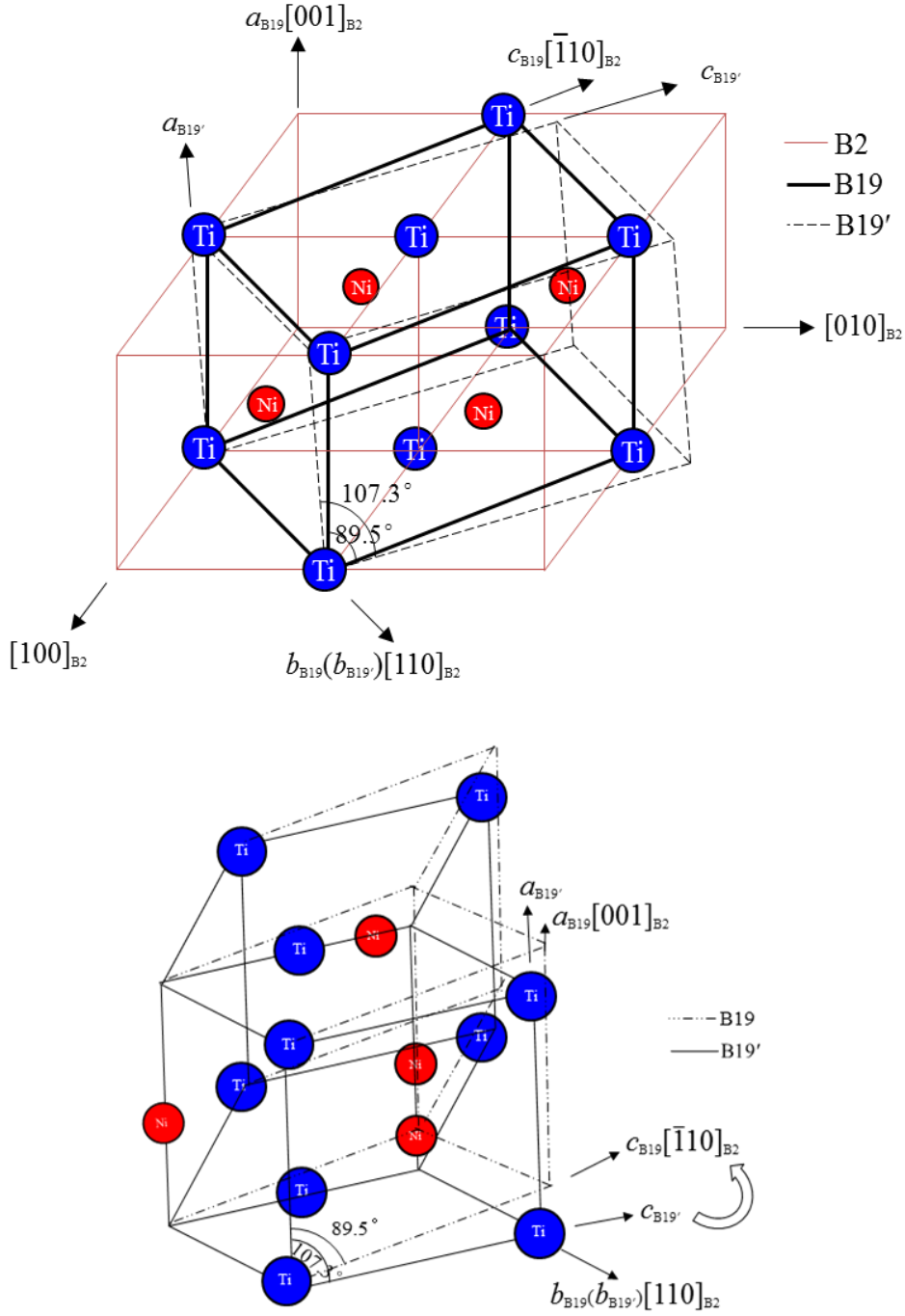


Figure 4.8 Schematic diagram showing the transition of martensite crystal structure from B19' to B19 as a result of Cu addition in TiNi.

Moreover, this change is gradual. From Table 4.6, Table 4.7, Table 4.8, Table 4.9 and Figure 4.6, it can be clearly observed that the displacements of both Ti and Ni/Cu atoms in the  $x$ -direction are continuous, which results in a

continuous change of the monoclinic angle and lattice parameters, leading to successive changes in the crystal structure. Thus, it can be surmised that, with increasing Cu content in TiNiCu alloys, the change in the martensite crystal structure from monoclinic B19' to orthorhombic B19 is not dramatic but gradual. Furthermore, MT temperatures can be affected by various factors, in particular the chemical content. Accompanied by the change of the martensite crystal structure from B19' to B19, the transformation hysteresis in TiNiCu SMAs drastically reduces from as high as 30 K to as low as 5 K. Through understanding the pathway of transition of martensite crystal structures from B19' to B19 as a result of alloying, it might help to understand the drastic change in the transformation hysteresis due to Cu addition.

Accommodation of Cu in the monoclinic martensitic TiNi takes place by substitution of Ni atom, and it is assumed that replacements are controlled primarily by the size mismatch of Cu [184]. The atomic radii of Ti, Ni and Cu are 1.45 Å, 1.29 Å and 1.28 Å, respectively. As the atomic radii of Cu is slightly smaller than that of Ni, the size mismatch is not significant, which is consistent with previous observation that there is no dramatic change of crystal structure when substituting Cu in TiNiCu martensitic alloys [185].

In Section 4.3, we noted that more electrons escape from the Ti atoms in comparison with equiatomic TiNi binary alloy with increasing Cu content [185]. The more charge transfer between Ti and Ni/Cu atoms, the stronger the

interaction between them will be, and the higher the bonding force between them is, leading to a shorter bond length.

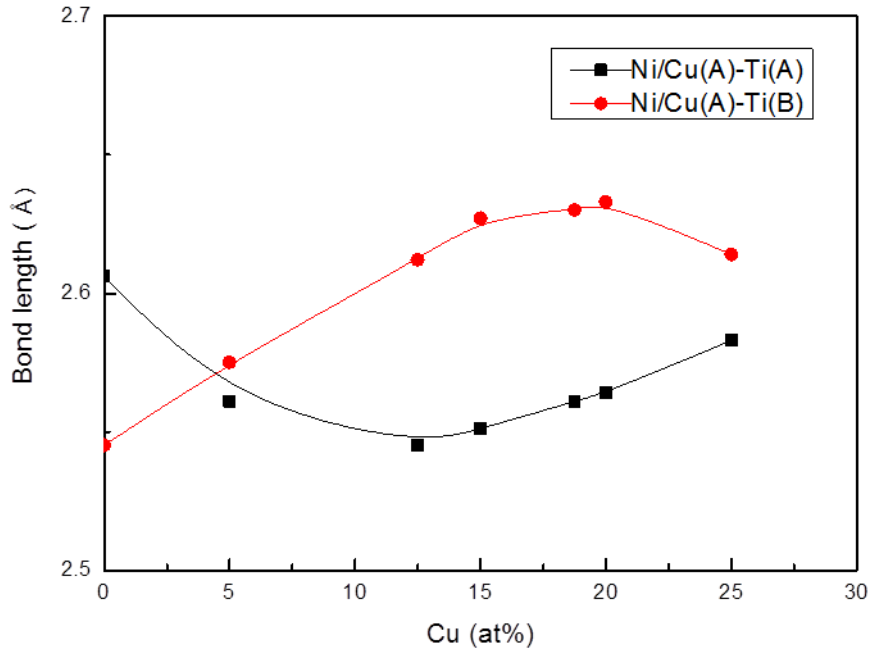


Figure 4.9 Variation of Ni/Cu-Ti bond length with Cu content.

In Figure 4.9, the bond length of Ni/Cu(A)-Ti(A) and Ni/Cu(A)-Ti(B) as a function of Cu content in TiNiCu alloys are presented. It can be observed that, with increasing Cu content in TiNiCu martensite, the bond length between Ni/Cu(A) and Ti(B) atoms increases, leading to an increase of lattice parameter  $b$ , which agrees well with previous observation [185]. For the bond length between Ni/Cu(A) and Ti(A) atoms, it decreases initially and then increases. When Cu content increases from 0 at% to 15 at%, more electrons escape from Ti(A) to Ni/Cu(A), leading to a stronger interaction and resulting in a decrease

of bond length between them. When Cu content is more than 15 at%, less electrons escape from Ti(A) to Ni/Cu(A), leading to a weak interaction which results in an increase in the bond length between them. Meanwhile, the interaction between Ni/Cu(A) and Ti(B) becomes stronger, and when Cu content reaches 20 at%, the bond length between them begins to decrease.

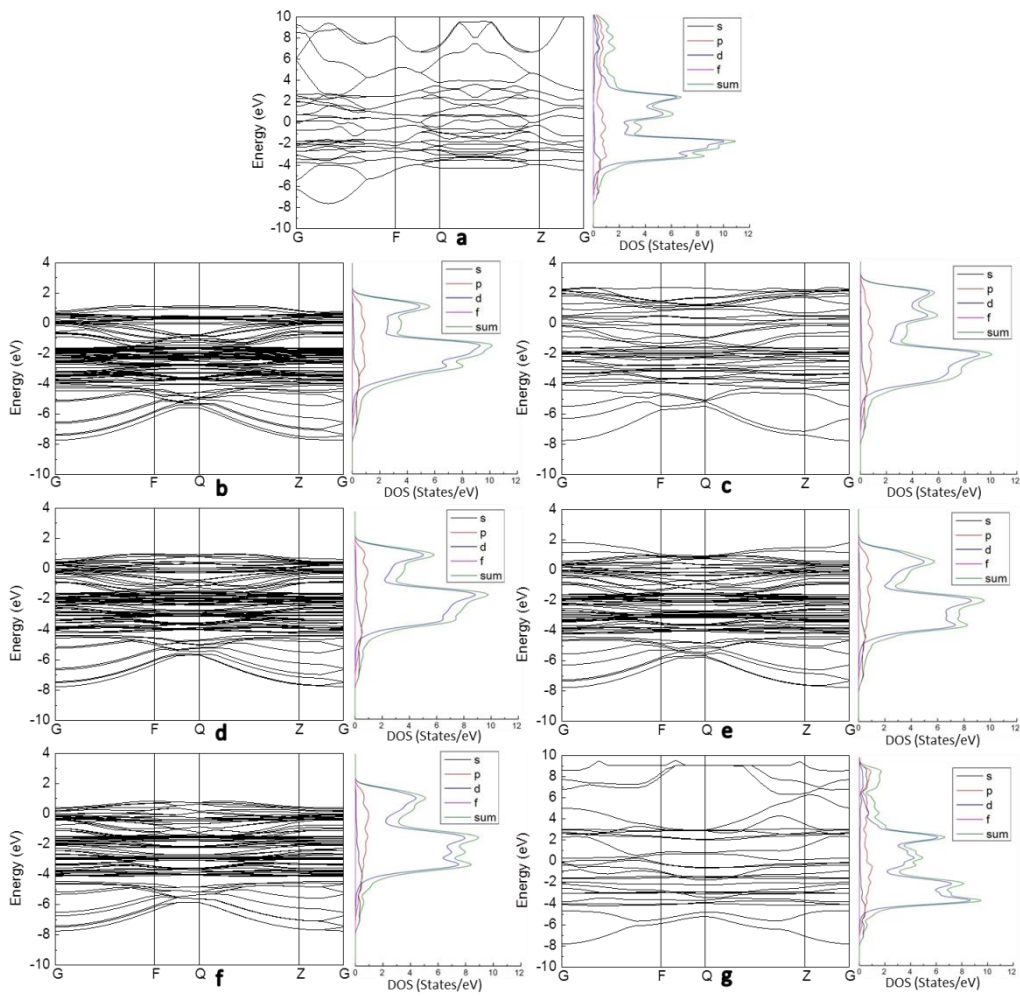


Figure 4.10 Band structures and associated partial density of states for (a) binary  $\text{Ti}_{50}\text{Ni}_{50}$ ; (b)  $\text{Ti}_{50}\text{Ni}_{45}\text{Cu}_5$ ; (c)  $\text{Ti}_{50}\text{Ni}_{37.5}\text{Cu}_{12.5}$ ; (d)  $\text{Ti}_{50}\text{Ni}_{35}\text{Cu}_{15}$ ; (e)  $\text{Ti}_{50}\text{Ni}_{31.25}\text{Cu}_{18.75}$ ; (f)  $\text{Ti}_{50}\text{Ni}_{30}\text{Cu}_{20}$ ; and (g)  $\text{Ti}_{50}\text{Ni}_{25}\text{Cu}_{25}$  with the Fermi level defined at 0 eV.

Figure 4.10 presents the band structures and associated partial density of states (DOS) of TiNiCu alloys for several symmetry directions in  $k$  space. The number of bands varies when a different number of unit cells was used to carry out the calculations. From this figure, most of the bands are observed near and below the Fermi level and the bands are similar at lower energy. For TiNiCu with Cu content between 5% and 20%, a narrow gap exists near the Fermi level, which is different from the TiNi binary alloy and  $\text{Ti}_{50}\text{Ni}_{25}\text{Cu}_{25}$ . Moreover, bands at higher energy are only observed in the TiNi binary alloy and  $\text{Ti}_{50}\text{Ni}_{25}\text{Cu}_{25}$ , which also indicates that the TiNiCu with Cu content between 5% and 20% is the transition phase from monoclinic to orthorhombic.

On the other hand, in this figure, the partial local s, p and f DOS are very small in all compounds compared to the d DOS, which indicates that, for TiNiCu alloys, d orbital character plays a primary role in DOS, the same as in the TiNi binary alloy. In partial DOS, the Ti, Ni and Cu states exhibit sharp peaks, in which the peak apex of the Ti d-states occurs at a higher energy than the peak apex of the Ni and Cu d-states. It also can be observed that with Cu content exceeding 15%, a dual peak is shown at a lower energy, which shows that with increasing Cu content, the Cu d-states are making an increasingly important contribution to the partial DOS which may be responsible for the transition of the crystal structure.

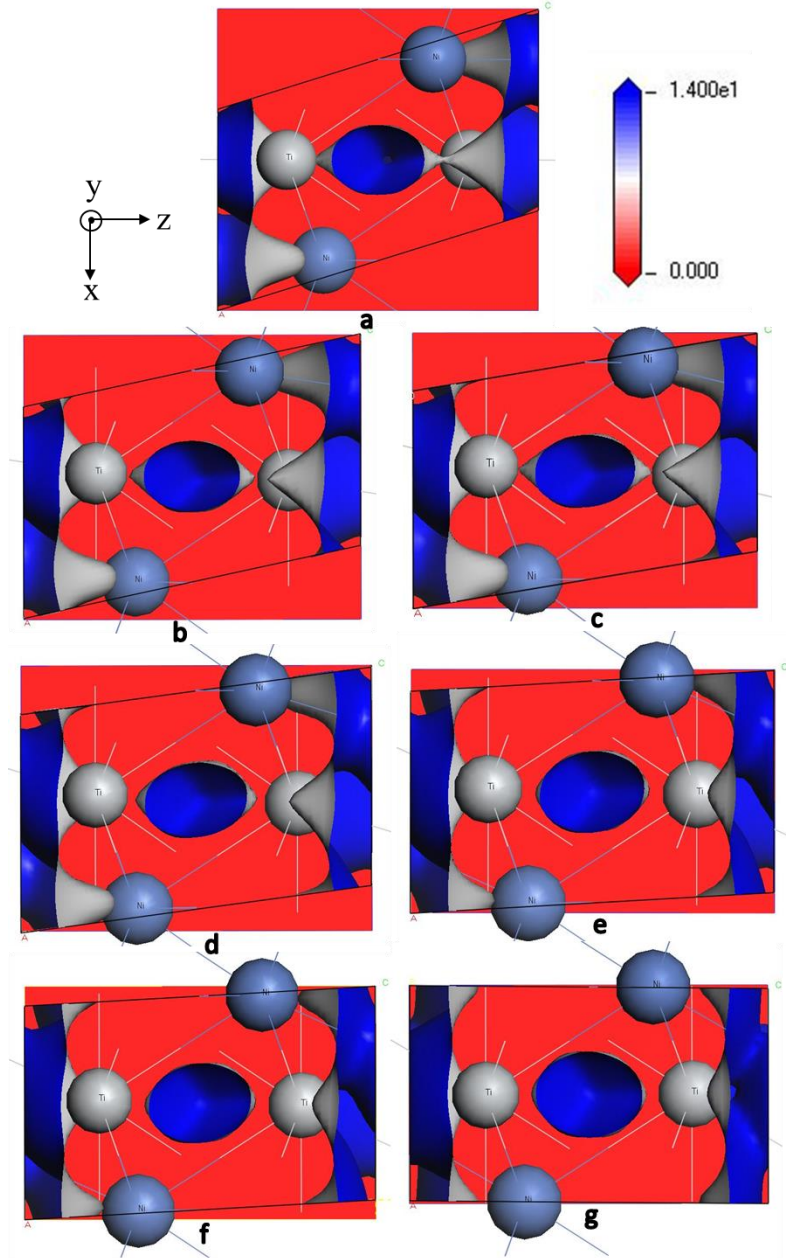


Figure 4.11 2D total electron density projection plots in the XZ plane with color legend indicating magnitude of charge distribution for (a) binary  $\text{Ti}_{50}\text{Ni}_{50}$ ; (b)  $\text{Ti}_{50}\text{Ni}_{45}\text{Cu}_5$ ; (c)  $\text{Ti}_{50}\text{Ni}_{37.5}\text{Cu}_{12.5}$ ; (d)  $\text{Ti}_{50}\text{Ni}_{35}\text{Cu}_{15}$ ; (e)  $\text{Ti}_{50}\text{Ni}_{31.25}\text{Cu}_{18.75}$ ; (f)  $\text{Ti}_{50}\text{Ni}_{30}\text{Cu}_{20}$ ; and (g)  $\text{Ti}_{50}\text{Ni}_{25}\text{Cu}_{25}$ .

Figure 4.11 shows the two-dimensional (2D) plots for the total electron density projection in the XZ plane, from which an electronic charge depletion at the Ti lattice site and accumulation at the Ni/Cu site, with increasing Cu content, can be observed. When Cu content is below 15%, the charge density is



approximately symmetrically distributed throughout the crystal structure. However, it becomes uneven when Cu content exceeds 15%. More charge transfer between Ti(A) and Ni/Cu(B) is observed, which may lead to a lower bonding force between Ti(A) and Ni/Cu(A), and hence an increase in the bond length, being consistent with our previous observations of bond length. In addition, the gradual change in the charge density redistribution plays an essential role in the gradual change of crystal structures.

#### 4.4.3 Summary

The present section has studied the atomic positions and displacements in martensite crystal structure of  $\text{Ti}_{50}\text{Ni}_{50-x}\text{Cu}_x$  ( $x = 0, 5, 12.5, 15, 18.75, 20, 25$ ) alloys using density functional theory. Based on the crystal structure optimizations of TiNiCu martensite consisting of different amounts of Cu substituting for Ni, the following conclusions can be drawn:

As a result of Cu addition to TiNi, the shifting of Ti and Ni/Cu atoms along the  $x$ -axis is clearly evident, but minimal along the  $y$ - and  $z$ -axes. With increasing Cu content, the distance between two Ni/Cu atoms increases along the  $x$ -axis while the Ti atoms become closer, which is responsible for the rotation of the (100) plane, leading to a decrease in the monoclinic angle.

Due to the similar sizes of Ni and Cu atoms, by introduction of Cu into TiNi, the displacements of both Ti and Ni/Cu atoms along the  $x$ -axis are progressive, indicating no dramatic change in TiNiCu martensite crystal

structures, but the monoclinic angle decreases gradually until the orthorhombic structure is formed.

With increasing Cu content, the charge transfer between Ti and Ni/Cu atoms is suggested here to be responsible for the observed atomic displacement. The increase of bond length between the Ni/Cu(A) and Ti(B) atoms leads to an increase of lattice parameter  $b$ .

Through revealing the pathway of crystal structure change due to Cu-addition it might help to provide some useful information for understanding the drastic change in transformation hysteresis in TiNiCu alloys and for adjusting the transformation hysteresis through adjusting the chemical content of particular SMAs of interest.

## **4.5 Effect of Charge Transfers on Lattice Properties of TiNiCu SMAs**

In this section, the martensite crystal structures, electronic structures as well as the atomic displacement of  $\text{Ti}_{50}\text{Ni}_{50-x}\text{Cu}_x$  ( $x = 25, 30, 35, 37.5, 40, 45, 50$ ) shape memory alloys are studied using DFT. In order to effectively design SMAs with required properties, understanding the atomic displacement and subsequent changes in crystal structure as a result of alloying is of primary importance. However, a full quantum-level understanding of TiNiCu alloys with Cu content exceeding 25 at% is still lacking, where the mechanism of Cu addition in modifying the martensite crystal structure is not clearly understood.

As a plausible explanation for atomic displacement and martensite crystal

structure transition, the charge transfer in TiNiCu alloys is also examined. The results presented in this section may provide an insight for a better understanding of the martensite crystal structures of TiNiCu alloys with Cu content exceeding 25 at% and the transformation hysteresis in TiNiCu SMAs.

#### 4.5.1 Research Method

In the present section, Supercell Method (SM) and Virtual Crystal Method (VCM) are used to simulate the configurations. Currently, SM and VCM are the most widely adopted simulation methods in doping research. Generally, the results of SM possess higher accuracy but VCM incurs less computational time and can provide quick results on the trends. In our research, both these methods are used in terms of optimization of crystal structures and the calculated results are cross-checked.

Moreover, the earlier study in Section 4.3 has shown that the calculated lattice constants are independent of the number of unit cells as well as the atomic positions of Cu. Thus for each Cu content considered here, only one supercell or unit cell will be used to carry out the calculations. The unit cells of B19' and B19 martensite structures used here are the same as those shown in Figure 4.5, in which four atoms are indicated for each unit cell. The initial structures (unit cell and supercells) used for SM are shown in Figure 4.12.

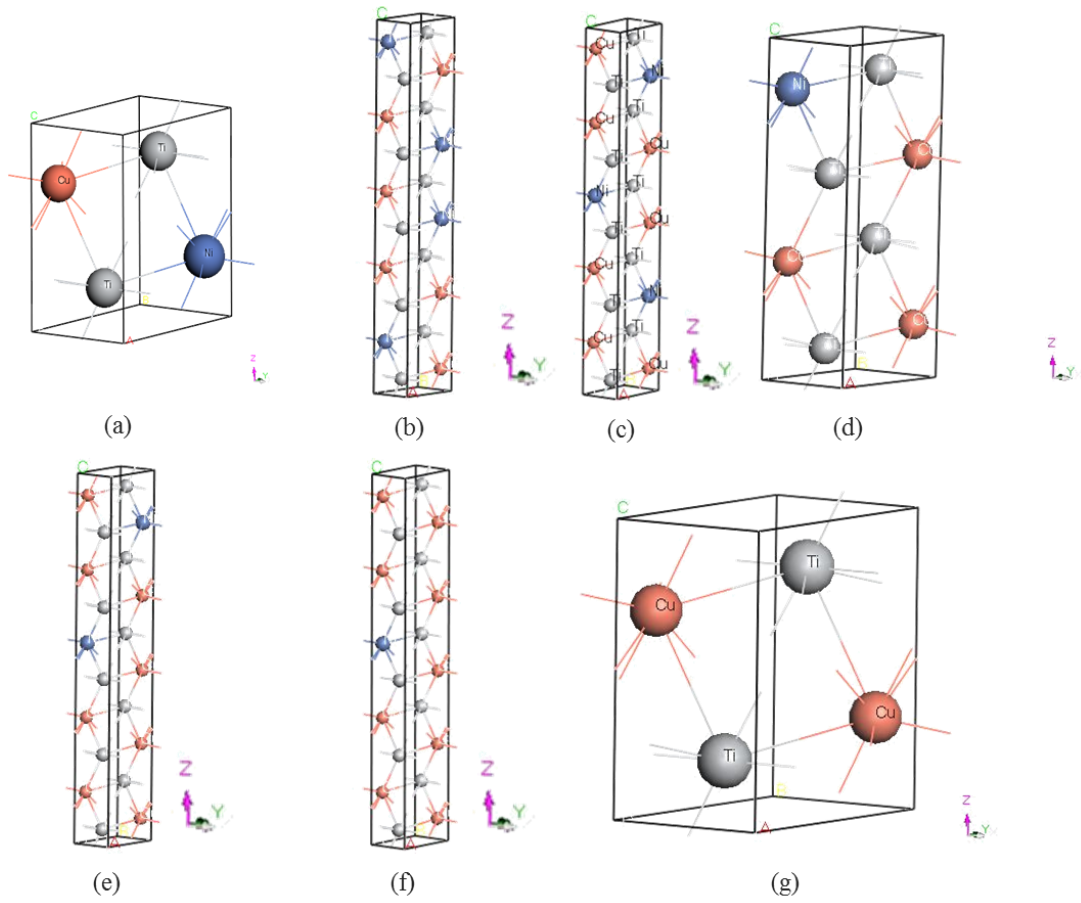


Figure 4.12 Initial unit cells and supercells of  $\text{Ti}_{50}\text{Ni}_{50-x}\text{Cu}_x$  (a) unit cell of  $\text{Ti}_{50}\text{Ni}_{25}\text{Cu}_{25}$  (b)  $1 \times 1 \times 5$  supercell of  $\text{Ti}_{50}\text{Ni}_{20}\text{Cu}_{30}$  (c)  $1 \times 1 \times 5$  supercell of  $\text{Ti}_{50}\text{Ni}_{15}\text{Cu}_{35}$  (d)  $1 \times 1 \times 2$  supercell of  $\text{Ti}_{50}\text{Ni}_{12.5}\text{Cu}_{37.5}$  (e)  $1 \times 1 \times 5$  supercell of  $\text{Ti}_{50}\text{Ni}_{10}\text{Cu}_{40}$  (f)  $1 \times 1 \times 5$  supercell of  $\text{Ti}_{50}\text{Ni}_5\text{Cu}_{45}$  (g) unit cell of  $\text{Ti}_{50}\text{Cu}_{50}$ .

#### 4.5.2 Results and Discussions

The calculated lattice parameters of  $\text{Ti}_{50}\text{Ni}_{25}\text{Cu}_{25}$ ,  $\text{Ti}_{50}\text{Ni}_{20}\text{Cu}_{30}$ ,  $\text{Ti}_{50}\text{Ni}_{15}\text{Cu}_{35}$ ,  $\text{Ti}_{50}\text{Ni}_{12.5}\text{Cu}_{37.5}$ ,  $\text{Ti}_{50}\text{Ni}_{10}\text{Cu}_{40}$ ,  $\text{Ti}_{50}\text{Ni}_5\text{Cu}_{45}$  and  $\text{Ti}_{50}\text{Cu}_{50}$  alloys by SM and VCM are listed in Table 4.10 and Table 4.11, respectively. The calculated results are compared with previously reported data. The lattice parameters and monoclinic angle, as a function of Cu content in TiNiCu alloys calculated using both SM and VCM, are shown in Figure 4.13.

Table 4.10. Lattice parameters and free energy of TiNiCu alloys with Cu content exceeding 25 at% obtained by the Supercell Method.

Alloys	No. of unit cell used	$a$ (Å)	$b$ (Å)	$c$ (Å)	$\beta$ (°)	Free Energy per unit cell (eV)	Volume per unit cell (Å <sup>3</sup> )
<b>Ti<sub>50</sub>Ni<sub>25</sub>Cu<sub>25</sub></b>	1	2.684	4.396	4.702	90.09	-5908.5414	55.4807
<b>Ti<sub>50</sub>Ni<sub>20</sub>Cu<sub>30</sub></b>	5	2.681	4.419	4.710	90.33	-5906.9002	55.8096
<b>Ti<sub>50</sub>Ni<sub>15</sub>Cu<sub>35</sub></b>	5	2.690	4.426	4.718	90.53	-5905.2554	56.1812
<b>Ti<sub>50</sub>Ni<sub>12.5</sub>Cu<sub>37.5</sub></b>	2	2.697	4.426	4.722	90.52	-5904.4304	56.3647
<b>Ti<sub>50</sub>Ni<sub>10</sub>Cu<sub>40</sub></b>	5	2.686	4.440	4.727	90.19	-5903.6087	56.4899
<b>Ti<sub>50</sub>Ni<sub>5</sub>Cu<sub>45</sub></b>	5	2.692	4.443	4.751	90.23	-5901.9633	56.8205
<b>Ti<sub>50</sub>Cu<sub>50</sub></b>	1	2.683	4.464	4.771	90.07	-5900.3158	57.1423
<b>Ti<sub>50</sub>Ni<sub>50</sub>-B19[186]</b>	---	2.88	4.28	4.52	90	---	---
<b>Ti<sub>50</sub>Ni<sub>50</sub>-B19'[123]</b>	---	2.89	4.12	4.62	96.5	---	---
<b>Ti<sub>50</sub>Ni<sub>50</sub>-BCO[126]</b>	1	2.948	4.006	4.928	107.3	-5916.8766	55.5891

Firstly, from Table 4.10, Table 4.11 and Figure 4.13, it can be found that the results from both SM and VCM are highly comparable and the trends are identical, which indicate that the calculated results are reliable and accurate.

Secondly, from the calculated results shown in Table 4.10, Table 4.11 and Figure 4.13, it can be observed that for Cu content exceeding 25 at%, the stable martensite crystal structure of TiNiCu alloys is orthorhombic (with monoclinic angle equal to 90 °). It is also clearly observed that compared to TiNiCu alloys with lower Cu content, the lattice parameters vary slightly with increasing Cu content, whereby  $a$  decreases while  $b$  and  $c$  increase slightly. It can be stated

that for TiNiCu alloys with Cu content exceeding 25 at%, Cu content has insignificant effect on the lattice constants.

Table 4.11 Lattice parameters and free energy of TiNiCu alloys with Cu content exceeding 25 at% obtained by the Virtual Crystal Method.

<b>Alloys</b>	<b><i>a</i> (Å)</b>	<b><i>b</i> (Å)</b>	<b><i>c</i> (Å)</b>	<b><i>β</i> (°)</b>	<b>Free Energy per unit cell (eV)</b>	<b>Volume per unit cell (Å<sup>3</sup>)</b>
<b>Ti<sub>50</sub>Ni<sub>25</sub>Cu<sub>25</sub></b>	2.789	4.314	4.645	90.313	-5859.1065	55.887204
<b>Ti<sub>50</sub>Ni<sub>20</sub>Cu<sub>30</sub></b>	2.754	4.354	4.671	89.91	-5858.8461	56.009126
<b>Ti<sub>50</sub>Ni<sub>15</sub>Cu<sub>35</sub></b>	2.730	4.383	4.694	90.12	-5862.2498	56.168501
<b>Ti<sub>50</sub>Ni<sub>12.5</sub>Cu<sub>37.5</sub></b>	2.722	4.396	4.703	90.10	-5865.3726	56.356821
<b>Ti<sub>50</sub>Ni<sub>10</sub>Cu<sub>40</sub></b>	2.712	4.409	4.716	90.11	-5869.7746	56.402589
<b>Ti<sub>50</sub>Ni<sub>5</sub>Cu<sub>45</sub></b>	2.695	4.439	4.740	90.18	-5882.1444	56.695032
<b>Ti<sub>50</sub>Cu<sub>50</sub></b>	2.683	4.465	4.771	90.07	-5900.3158	57.142322
<b>Ti<sub>50</sub>Ni<sub>50</sub>-B19[186]</b>	2.88	4.28	4.52	90	---	---
<b>Ti<sub>50</sub>Ni<sub>50</sub>-B19'[123]</b>	2.89	4.12	4.62	96.5	---	---
<b>Ti<sub>50</sub>Ni<sub>50</sub>-BCO[126]</b>	2.948	4.006	4.928	107.3	-5916.8766	55.5891

Thirdly, from Table 4.10 and Table 4.11, it can also be observed that with increasing Cu substitution in TiNiCu alloys with Cu content exceeding 25 at%, the free energy changes only slightly. This is consistent with the stable martensite crystal structure remaining unchanged, which is orthorhombic structure.

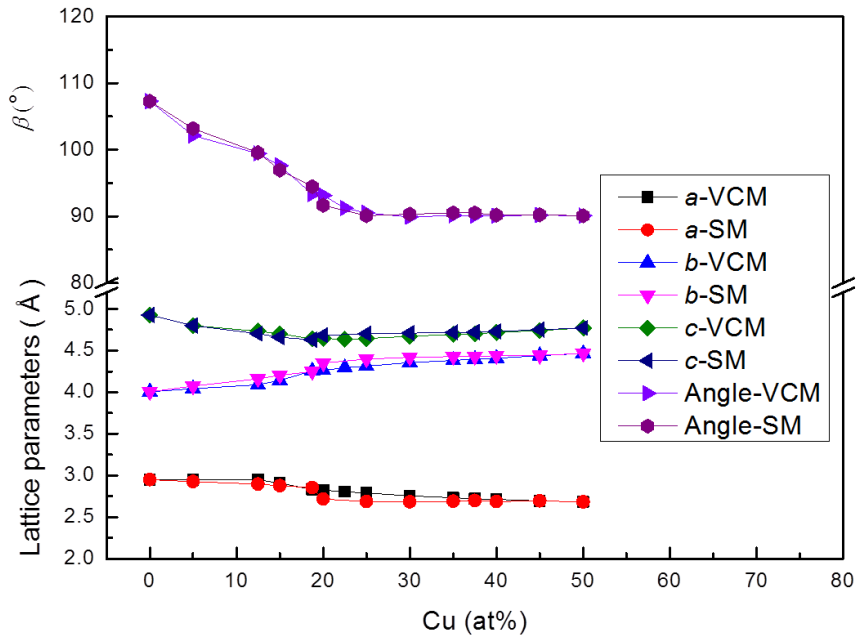


Figure 4.13 Variation of lattice parameters and monoclinic angle with Cu content.

The densities of states (DOS) of  $\text{Ti}_{50}\text{Ni}_{25}\text{Cu}_{25}$ ,  $\text{Ti}_{50}\text{Ni}_{20}\text{Cu}_{30}$ ,  $\text{Ti}_{50}\text{Ni}_{15}\text{Cu}_{35}$ ,  $\text{Ti}_{50}\text{Ni}_{12.5}\text{Cu}_{37.5}$ ,  $\text{Ti}_{50}\text{Ni}_{10}\text{Cu}_{40}$ ,  $\text{Ti}_{50}\text{Ni}_5\text{Cu}_{45}$  and  $\text{Ti}_{50}\text{Cu}_{50}$  alloys are presented in Figure 4.14. The calculated charge transfer per atom in TiNiCu alloys are listed in Table 4.12.

Table 4.12 Calculated charge transfer per atom in TiNiCu alloys with Cu content exceeding 25 at%.

Alloys	Charges ( $e$ )		
	Ti	Ni	Cu
$\text{Ti}_{50}\text{Ni}_{25}\text{Cu}_{25}$	0.54	-0.23	-0.85
$\text{Ti}_{50}\text{Ni}_{20}\text{Cu}_{30}$	0.578	-0.245	-0.8
$\text{Ti}_{50}\text{Ni}_{15}\text{Cu}_{35}$	0.617	-0.257	-0.774
$\text{Ti}_{50}\text{Ni}_{12.5}\text{Cu}_{37.5}$	0.638	-0.25	-0.767
$\text{Ti}_{50}\text{Ni}_{10}\text{Cu}_{40}$	0.654	-0.26	-0.7525
$\text{Ti}_{50}\text{Ni}_5\text{Cu}_{45}$	0.691	-0.26	-0.739
$\text{Ti}_{50}\text{Cu}_{50}$	0.73	--	-0.73

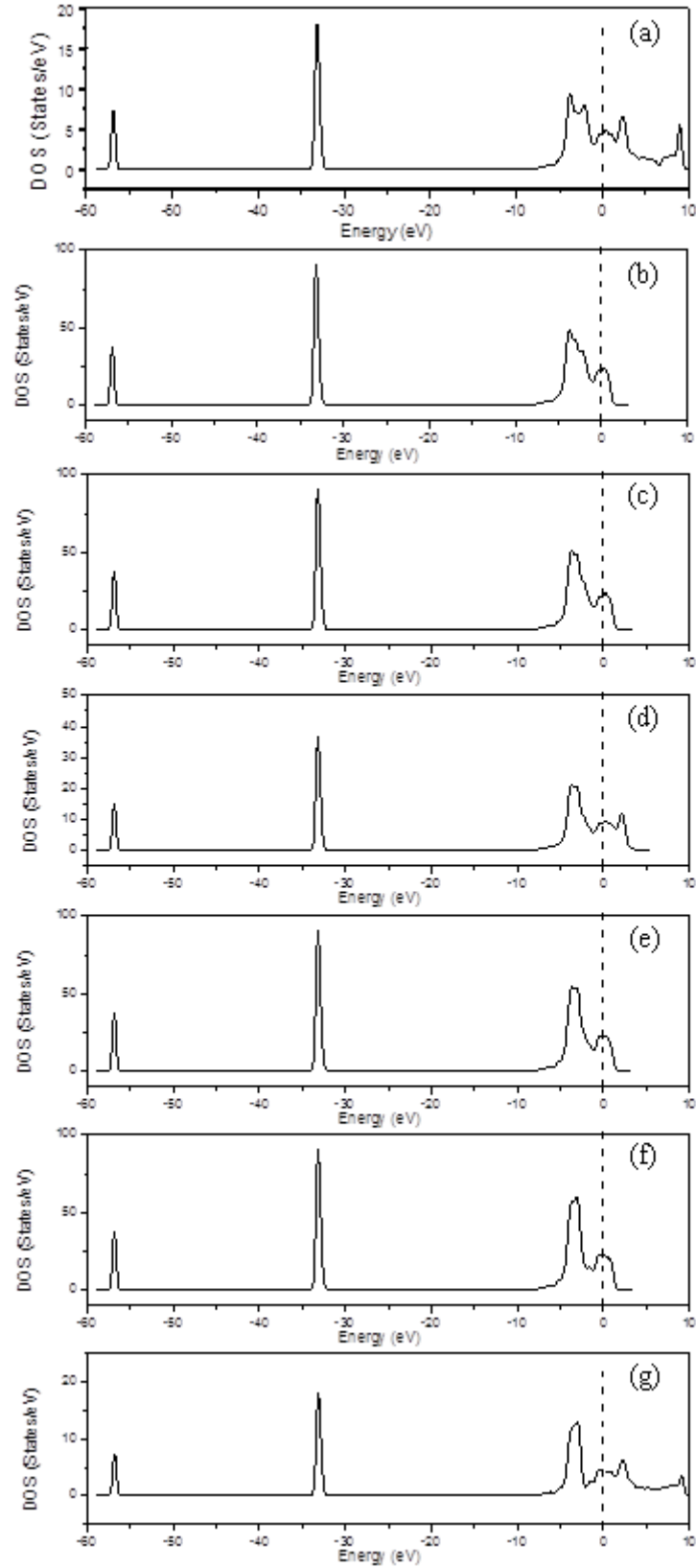


Figure 4.14 Density of states (DOS) for (a)  $\text{Ti}_{50}\text{Ni}_{25}\text{Cu}_{25}$ ; (b)  $\text{Ti}_{50}\text{Ni}_{20}\text{Cu}_{30}$ ; (c)  $\text{Ti}_{50}\text{Ni}_{15}\text{Cu}_{35}$ ; (d)  $\text{Ti}_{50}\text{Ni}_{12.5}\text{Cu}_{37.5}$ ; (e)  $\text{Ti}_{50}\text{Ni}_{10}\text{Cu}_{40}$ ; (f)  $\text{Ti}_{50}\text{Ni}_5\text{Cu}_{45}$  and (g)  $\text{Ti}_{50}\text{Cu}_{50}$ .



Since the DOS of electrons depends mainly on the local atomic environment [181], from Figure 4.14, it can be observed that these alloys have similar DOS since they have the same amount of Ti. For these alloys, the DOS at Fermi level are highly similar, which implies that the equilibrium crystal structures for these alloys are the same, and it agrees well with our previous observations. As observed in Table 4.12, since Cu atom attracts more electrons than Ni atom, with increasing Cu content, Ti atoms will progressively lose more and more electrons. However, with more Cu addition to TiNi, the charge transferred to Cu per atom decreases while that for Ni increases, leading to a weaker interaction between Ti and Cu atoms.

The calculated atomic positions of Ti and Ni/Cu as a result of Cu addition from VCM and SM are listed in Table 4.13, Table 4.15 and Table 4.14, Table 4.16 respectively.

Table 4.13 Atomic coordinates of Ti and Ni/Cu in TiNiCu alloys with Cu content exceeding 25 at% ( $y = 0.25$ ) from VCM.

Alloys	Atomic coordinate (Ni/Cu)			Atomic coordinate (Ti)		
	$x$	$y$	$z$	$x$	$y$	$z$
<b>Ti<sub>50</sub>Ni<sub>25</sub>Cu<sub>25</sub></b>	-0.0019	0.25	0.679	0.5065	0.25	0.212
<b>Ti<sub>50</sub>Ni<sub>20</sub>Cu<sub>30</sub></b>	-0.0004	0.25	0.679	0.5014	0.25	0.208
<b>Ti<sub>50</sub>Ni<sub>15</sub>Cu<sub>35</sub></b>	0.0004	0.25	0.679	0.4975	0.25	0.206
<b>Ti<sub>50</sub>Ni<sub>12.5</sub>Cu<sub>37.5</sub></b>	0.0003	0.25	0.678	0.4981	0.25	0.205
<b>Ti<sub>50</sub>Ni<sub>10</sub>Cu<sub>40</sub></b>	0.0003	0.25	0.677	0.4980	0.25	0.203
<b>Ti<sub>50</sub>Ni<sub>5</sub>Cu<sub>45</sub></b>	0.0003	0.25	0.677	0.4968	0.25	0.201
<b>Ti<sub>50</sub>Cu<sub>50</sub></b>	0.0001	0.25	0.676	0.4986	0.25	0.198

Table 4.14 Atomic coordinates of Ti and Ni/Cu in TiNiCu alloys with Cu content exceeding 25 at% ( $y = 0.25$ ) from SM.

Alloys	Atomic coordinate (Ni/Cu)			Atomic coordinate (Ti)		
	$x$	$y$	$z$	$x$	$y$	$z$
<b>Ti<sub>50</sub>Ni<sub>25</sub>Cu<sub>25</sub></b>	-0.0002	0.25	0.682	0.5003	0.25	0.213
<b>Ti<sub>50</sub>Ni<sub>20</sub>Cu<sub>30</sub></b>	0.0026	0.25	0.676	0.4760	0.25	0.199
<b>Ti<sub>50</sub>Ni<sub>15</sub>Cu<sub>35</sub></b>	0.0010	0.25	0.679	0.4913	0.25	0.198
<b>Ti<sub>50</sub>Ni<sub>12.5</sub>Cu<sub>37.5</sub></b>	0.0014	0.25	0.675	0.4909	0.25	0.190
<b>Ti<sub>50</sub>Ni<sub>10</sub>Cu<sub>40</sub></b>	0.0004	0.25	0.672	0.4969	0.25	0.193
<b>Ti<sub>50</sub>Ni<sub>5</sub>Cu<sub>45</sub></b>	0.0003	0.25	0.677	0.4958	0.25	0.198
<b>Ti<sub>50</sub>Cu<sub>50</sub></b>	0.0002	0.25	0.676	0.4978	0.25	0.198

Table 4.15 Atomic coordinates of Ti and Ni/Cu in TiNiCu alloys with Cu content exceeding 25 at% ( $y = 0.75$ ) from VCM.

Alloys	Atomic coordinate (Ni/Cu)			Atomic coordinate (Ti)		
	$x$	$y$	$z$	$x$	$y$	$z$
<b>Ti<sub>50</sub>Ni<sub>25</sub>Cu<sub>25</sub></b>	1.0079	0.75	0.321	0.4935	0.75	0.788
<b>Ti<sub>50</sub>Ni<sub>20</sub>Cu<sub>30</sub></b>	1.0004	0.75	0.321	0.4987	0.75	0.792
<b>Ti<sub>50</sub>Ni<sub>15</sub>Cu<sub>35</sub></b>	0.9996	0.75	0.322	0.5025	0.75	0.794
<b>Ti<sub>50</sub>Ni<sub>12.5</sub>Cu<sub>37.5</sub></b>	0.9997	0.75	0.322	0.5019	0.75	0.795
<b>Ti<sub>50</sub>Ni<sub>10</sub>Cu<sub>40</sub></b>	0.9997	0.75	0.323	0.5020	0.75	0.797
<b>Ti<sub>50</sub>Ni<sub>5</sub>Cu<sub>45</sub></b>	0.9998	0.75	0.323	0.5032	0.75	0.799
<b>Ti<sub>50</sub>Cu<sub>50</sub></b>	0.9999	0.75	0.324	0.5014	0.75	0.802

Table 4.16 Atomic coordinates of Ti and Ni/Cu in TiNiCu alloys with Cu content exceeding 25 at% ( $y = 0.75$ ) from VCM.

Alloys	Atomic coordinate (Ni/Cu)			Atomic coordinate (Ti)		
	$x$	$y$	$z$	$x$	$y$	$z$
<b>Ti<sub>50</sub>Ni<sub>25</sub>Cu<sub>25</sub></b>	1.0002	0.75	0.318	0.4997	0.75	0.787
<b>Ti<sub>50</sub>Ni<sub>20</sub>Cu<sub>30</sub></b>	0.9974	0.75	0.324	0.5240	0.75	0.801
<b>Ti<sub>50</sub>Ni<sub>15</sub>Cu<sub>35</sub></b>	0.9989	0.75	0.322	0.5087	0.75	0.802
<b>Ti<sub>50</sub>Ni<sub>12.5</sub>Cu<sub>37.5</sub></b>	0.9986	0.75	0.325	0.5091	0.75	0.809
<b>Ti<sub>50</sub>Ni<sub>10</sub>Cu<sub>40</sub></b>	0.9996	0.75	0.328	0.5030	0.75	0.807
<b>Ti<sub>50</sub>Ni<sub>5</sub>Cu<sub>45</sub></b>	0.9997	0.75	0.323	0.5042	0.75	0.802
<b>Ti<sub>50</sub>Cu<sub>50</sub></b>	0.9998	0.75	0.324	0.5022	0.75	0.802

From the calculated results listed in Table 4.13, Table 4.15 and Table 4.14, Table 4.16, it can be clearly observed that for Cu content from 25 at% to 50 at%, the displacements of both Ni/Cu and Ti atoms along the  $y$ -axis remain unchanged and change slightly along the  $x$ - and  $z$ -axes.

In Section 4.3 and Section 4.4, we noted that more electrons escape from the Ti atoms in comparison with equiatomic TiNi binary alloy with increasing Cu content from 0 at% to 25 at%. The more charge transfer between Ti and Ni/Cu atoms, the stronger will be the interaction between them, and the higher is the bonding force between them, leading to a shorter bond length [187]. In Figure 4.15, the 3-D illustration of Ti<sub>50</sub>Ni<sub>25</sub>Cu<sub>25</sub> and the charge transfer per atom as well as the bond length of Ni/Cu(A)-Ti(A) and Ni/Cu(A)-Ti(B) as a function of Cu content in TiNiCu alloys are presented. From these calculations, we note that for TiNiCu alloys with Cu content exceeding 25 at%, the positions

of both Ti and Cu/Ni atoms along the  $y$ -axis remain unchanged, while slight changes were observed along the  $x$ - and  $z$ -axes. This means that all the atomic displacements occurred within the (010) planes, i.e. (010) plane at  $y = 0.25$  and (010) plane at  $y=0.75$ . As shown in Figure 4.15(a), we label the atoms within the (010) plane at  $y=0.25$  as Ni/Cu(A) and Ti(A), and the atoms within the (010) plane at  $y=0.75$  as Ni/Cu(B) and Ti(B), respectively.

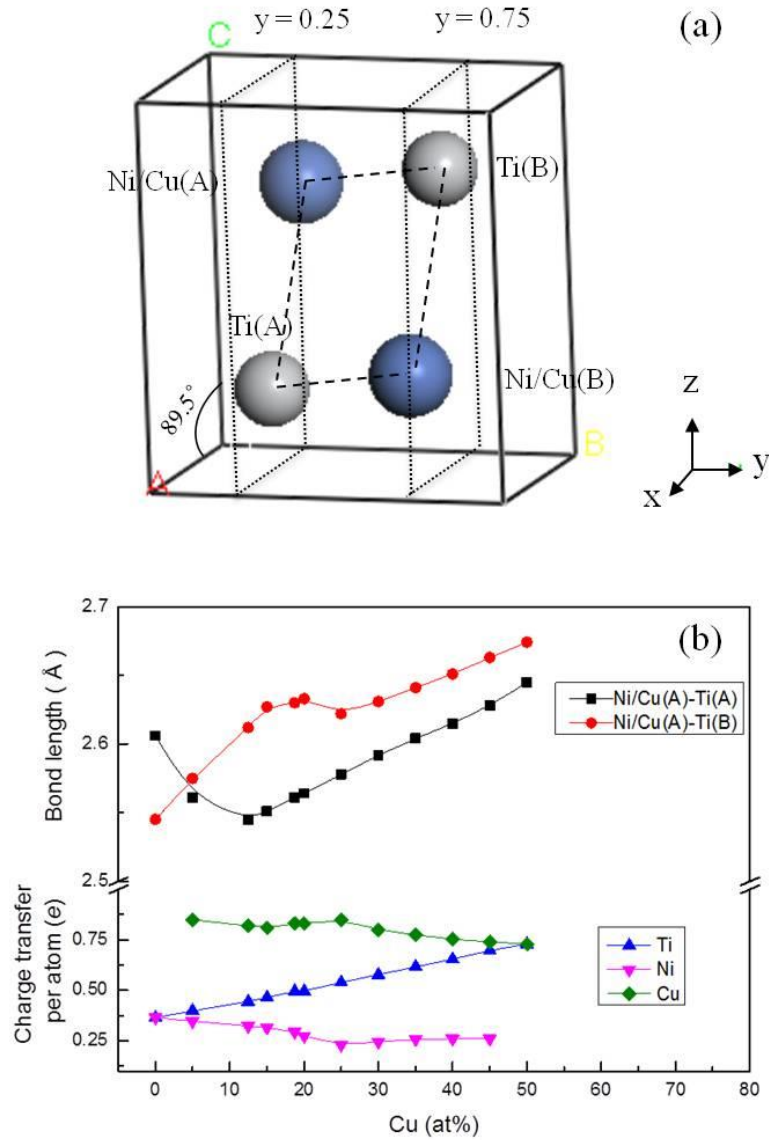


Figure 4.15 (a) 3-D illustration of  $\text{Ti}_{50}\text{Ni}_{25}\text{Cu}_{25}$  (b) Variation of charge transfer and Ni/Cu-Ti bond length with Cu content.

Figure 4.15(b) shows that with increasing Cu content in TiNiCu martensite, the electrons which escape per Ti atom increase linearly, whereas the electrons transferred to both Ni and Cu (per atom) decrease. Since each Cu atom attracts more electrons than Ni atom, it is reasonable to relate the increment in electrons escaping from Ti to the increasing Cu content. However, the increasing Cu content also results in the escaped electrons (from Ti) being competed for, by more Cu atoms theoretically. This competition among the Cu atoms hence lessens the charge transfer for each Cu atom. In addition, Figure 4.15 also shows that with increasing Cu content, the bond length between Ni/Cu(A) and Ti(B) atoms increases, leading to an increment of lattice parameter  $b$ , which agrees well with previous observation. It can thus be explained that with Cu content between 0 at% and 15 at%, more electrons escape from Ti(A) to Ni/Cu(A), leading to a strong interaction and a decrease of bond length between them. However, when Cu content exceeds 15 at%, less electrons escape from Ti(A) to Ni/Cu(A), leading to a weak interaction which results in an increase of bond length. Therefore, along with the increment of Cu content, the bond length between Ni/Cu(A) and Ti(A) atoms decreases before Cu content reaches 15 at%, and increases when Cu content exceeds 15 at%. Correspondingly, the lattice parameter  $c$  shares the same trend which is well consistent with previous observations.

Accommodation of Cu in the monoclinic martensitic TiNi takes place by substitution of Ni atom, and it is assumed that replacements are controlled

primarily by the size mismatch of Cu. Table 4.10 and Table 4.11 also show that for TiNiCu alloys with Cu content exceeding 25 at%, the unit cell volume increases slightly with increasing Cu content. The unit cell volume of an intermetallic crystal is controlled by the bond lengths. The atomic radii of Ti, Ni and Cu are 1.45 Å, 1.29 Å and 1.28 Å, respectively. As the size mismatch of Cu atom and Ni atom is minimal, this effect on unit cell volume changes is insignificant. On the other hand, when Cu content is higher than 25 at%, the bond length between Ni/Cu and Ti increases with increasing Cu content, leading to the slight increase of unit cell volume.

### 4.5.3 Summary

In this section, we have studied the stable crystal structure and electronic structure of  $\text{Ti}_{50}\text{Ni}_{50-x}\text{Cu}_x$  ( $x = 25, 30, 35, 37.5, 40, 45, 50$ ) alloys as well as the atomic positions and displacements in their martensite crystal structure using density functional theory. Based on the crystal structure optimizations of TiNiCu martensite with Cu content exceeding 25 at%, the following conclusions can be drawn:

For  $\text{Ti}_{50}\text{Ni}_{50-x}\text{Cu}_x$  alloys with Cu content exceeding 25 at%, the stable martensite structure is orthorhombic. With increasing Cu content, the positions of both Ti and Cu/Ni atoms along y-axis remain unchanged and change slightly along  $x$  and  $z$  axes, leading to only minimal changes in the lattice parameters, whereby  $a$  decreases while  $b$  and  $c$  increase slightly.

With increasing Cu content, the charge transfer between Ti and Ni/Cu atoms is suggested here to be responsible for the observed atomic displacements. The increase in bond length between the Ni/Cu(A) and Ti(B) atoms leads to an increase of lattice parameter  $b$  and changes in the bond length between Ni/Cu(A) and Ti(A) atoms, which decreases initially and then increases. This also results in the lattice parameter  $c$  initially decreasing and then increasing.

When Cu content is higher than 25 at%, the bond length between both Ni/Cu(A) - Ti(A) and Ni/Cu(A) - Ti(B) increase with increasing Cu content. Since the size mismatch of Cu atom and Ni atom is not significant, the unit cell volume increases only slightly.

Also, the numerical approach used in this chapter provides a new avenue for better understanding of the martensite crystal structures of TiNiCu alloys with Cu content exceeding 25 at%, and offers reasonable explanations.

# Chapter 5 Conclusions and Future Work

## 5.1 Summary

The current research on TiNi-based SMAs shows that the martensitic phase transformation and the reverse transformation are integral to the shape memory effect as well as superelasticity in TiNi-based SMAs. In this thesis, the different phase transformation paths of TiNi-based SMAs have been reviewed. The review revealed that there is no unambiguous structure for these martensitic transformations. Then, the density functional theory (DFT) and other relevant background information are introduced.

Leveraging on the DFT CASTEP code, the crystal structures of equiatomic TiNi binary alloy and TiNiCu with various Cu contents were constructed and investigated. In tandem, the study has also calculated the Mulliken charge transfers, density of states, and atomic displacement, to analyze these structures in detail. The simulation outcomes obtained from this study shows good correspondence with earlier reported experimental and theoretical data, thus verifying that the DFT methodology and results presented in this thesis are accurate and reliable for investigating the mechanisms of martensite transformation associated with the shape memory effect.



## 5.2 Conclusions

We have studied the stable crystal structure and electronic structure as well as the atomic positions and displacements in martensite crystal structure of  $\text{Ti}_{50}\text{Ni}_{50-x}\text{Cu}_x$  ( $x = 0, 5, 12.5, 15, 18.75, 20, 25, 30, 35, 37.5, 40, 45, 50$ ) alloys using density functional theory. Based on the crystal structure optimizations of equiatomic TiNi martensite structure and TiNiCu martensite structures, the following conclusions were drawn:

1. Due to the lower free energy, the base-centred orthorhombic (BCO) structure is more stable than the B19'' structure. The B19'' phase can be considered as a transition phase between B19' and BCO and may play a role in the stabilization of the B19' structure, based on observations of the monoclinic angle.
2. For TiNiCu alloys with Cu content between 0 at% and 25 at%, as a result of Cu addition to TiNi, the martensite lattice parameters  $a$  and  $c$  and the monoclinic angle decrease, whereas the lattice parameter  $b$  increases with increasing Cu content. When Cu content reaches 20 at%, the monoclinic martensite crystal structure becomes unstable and an orthorhombic crystal structure is formed. This computational outcome agrees well with experimental observations.
3. With increasing Cu content, more electrons escape from the Ti atoms. As the Cu atoms attract more electrons as compared to the Ni atoms, fewer charge transfer from Ti to Ni occurs as compared to that in binary TiNi

alloy. Since both the atomic radius and the number of valence electrons of Cu are quite similar to those of Ni, the unit cell volumes of TiNiCu martensite structures vary only slightly with different Cu contents.

4. For TiNiCu alloys with Cu content between 0 at% and 25 at%, as a result of Cu addition to TiNi, the shifting of Ti and Ni/Cu atoms along the  $x$ -axis is clearly evident, but minimal along the  $y$  and  $z$  axes. With increasing Cu content, the distance between two Ni/Cu atoms increases along the  $x$ -axis while the Ti atoms become closer, which is responsible for the rotation of the (100) plane, leading to a decrease in the monoclinic angle.
5. Due to the similar sizes of Ni and Cu atoms, by introduction of Cu into TiNi, the displacements of both Ti and Ni/Cu atoms along the  $x$ -axis are progressive, indicating no dramatic change in TiNiCu martensite crystal structures, but the monoclinic angle decreases gradually until the orthorhombic structure is formed.
6. With increasing Cu content, the charge transfer between Ti and Ni/Cu atoms is suggested here to be responsible for the observed atomic displacement. The increase of bond length between the Ni/Cu(A) and Ti(B) atoms leads to an increase of lattice parameter  $b$ .
7. For  $\text{Ti}_{50}\text{Ni}_{50-x}\text{Cu}_x$  alloys with Cu content exceeding 25 at%, the stable martensite structure is orthorhombic. With increasing Cu content, the positions of both Ti and Cu/Ni atoms along the  $y$ -axis remain unchanged,

and change slightly along  $x$ - and  $z$ -axes, leading to insignificant changes in the lattice parameters, whereby  $a$  decreases while  $b$  and  $c$  increase slightly.

8. With increasing Cu content, the charge transfer between Ti and Ni/Cu atoms is suggested here to be responsible for the observed atomic displacements. The increase in bond length between the Ni/Cu(A) and Ti(B) atoms leads to an increase of lattice parameter  $b$  and changes in the bond length between Ni/Cu(A) and Ti(A) atoms, which decreases initially and then increases. This also leads to the lattice parameter  $c$  decreasing initially and then increasing.
9. When Cu content is higher than 25 at%, the bond lengths between both Ni/Cu(A) - Ti(A) and Ni/Cu(A) - Ti(B) increase with increasing Cu content. Since the size mismatch of Cu atom and Ni atom is not significant, the unit cell volume increases only slightly due to the bond length changes.
10. The first-principle DFT numerical approach employed in this thesis provides a new avenue for investigating the effect of alloying on the crystal structure change in SMAs, and offers reasonable predictions.

### **5.3 Suggestions for Future Work**

Although substantial work on equiatomic TiNi and  $\text{Ti}_{50}\text{Ni}_{50-x}\text{Cu}_x$  martensite structure has been conducted in this thesis, the following studies are also important and can be investigated further in the future.

1. For equiatomic TiNi alloys, as aforementioned, there are diversified twinning structures in TiNi-based SMAs. Further investigations should be carried out to validate whether other twinning conditions could stabilize the B19' structure in TiNi martensite. In other words, more B19' twinning structures should be established and optimized to provide a more comprehensive explanation to the difference between experimental observations and theoretical results.
2. Element replacement effect, which can effectively improve the mechanical and physical properties of alloys can be explored. In tandem, based on the computational method provided in this thesis, the possibility of developing new shape memory alloys by substituting other metal atoms for the Ni and Ti atoms can be investigated in a quick and efficiency way. On the other hand, more efforts can also be dedicated to discover the relations between the electronic structures and the alloys' significant properties such as martensite transformation path, hysteresis, etc.
3. With the rapid development of thin film SMAs, the computational methods used in this thesis can also be applied to investigate the electronic properties of thin film SMAs, which may provide us with very important information for realizing their full potential in future applications.
4. Moreover, the role of temperature and stress during the martensite transformation should also be further investigated to obtain a better

understanding of temperature and stress effects on the crystal structures, as well as the mechanical and physical properties.

Through all the above efforts, a full atomic and electronic level understanding can be established to describe the martensite transformation processes associated with the shape memory effect.

# Reference

- [1] Ölander A. An electrochemical investigation of solid cadmium-gold alloys. *Journal of the American Chemical Society* 1932;54:3819-3833.
- [2] Vernon LB, Vernon HM. Process of manufacturing articles of thermoplastic synthetic resins. U.S. Patent 2,234,993[P]. 1941-3-18.
- [3] Chang L, Read T. Behavior of the elastic properties of AuCd. *Transactions of the Metallurgical Society of AIME* 1951;189:47.
- [4] Buehler WJ, Gilfrich JV, Wiley RC. Effect of low-temperature phase changes on mechanical properties of alloys near composition TiNi. *Journal of Applied Physics* 1963;34:1475-1477.
- [5] Kauffman GB, Mayo I. The story of nitinol: the serendipitous discovery of the memory metal and its applications. *The chemical educator* 1997;2:1-21.
- [6] Otsuka K, Kakeshita T. Science and technology of shape-memory alloys: New developments. *Mrs Bulletin* 2002;27:91-100.
- [7] Cai W, Meng XL, Zhao LC. Recent development of TiNi-based shape memory alloys. *Current Opinion in Solid State & Materials Science* 2005;9:296-302.
- [8] Yuan B, Chung CY, Zhu M. Microstructure and martensitic transformation behavior of porous NiTi shape memory alloy prepared by hot isostatic pressing processing. *Materials Science and Engineering a-Structural Materials Properties Microstructure and Processing* 2004;382:181-187.
- [9] Van Humbeeck J. Non-medical applications of shape memory alloys. *Materials Science and Engineering: A* 1999;273:134-148.
- [10] Hosoda H, Hanada S, Inoue K, Fukui T, Mishima Y, Suzuki T. Martensite transformation temperatures and mechanical properties of ternary NiTi alloys with offstoichiometric compositions. *Intermetallics* 1998;6:291-301.
- [11] Honma T, Matsumoto M, Shugo Y, Yamazaki I. Effects of Addition of 3 d Transition Elements on the Phase Tranformation in TiNi Compound. *ICOMAT 1979 Martensitic Transformations* 1979:259-264.
- [12] Hsieh S, Chen S, Lin H, Lin M, Huang J, Lin M. A study of TiNiCr ternary shape memory alloys. *Journal of Alloys and Compounds* 2010;494:155-160.
- [13] Toth L, Beyer J. Structure of a new orthorhombic phase in TiNi--Mn shape memory alloys. *Scripta metallurgica et materialia* 1991;25:425-430.
- [14] Zhu Y, Pan H, Wang G, Gao M, Ma J, Chen C, Wang Q. Phase structure, crystallography and electrochemical properties of Laves phase compounds  $\text{Ti}_{0.8}\text{Zr}_{0.2}\text{V}_{1.6}\text{Mn}_{0.8-x}\text{MxNi}_{0.6}$  (M= Fe, Al, Cr, Co). *International journal of hydrogen energy* 2001;26:807-816.
- [15] Lindquist P, Wayman C. Shape Memory and Transformation Behavior of Martensitic Ti--Pd--Ni and Ti--Pt--Ni Alloys. Butterworth-Heinemann, Engineering Aspects of Shape Memory Alloys(UK), 1990 1990:58-68.
- [16] Klopotov A, Gyunter V, Chekalkin T, Kozlov E. Crystal chemistry and martensite phase diagrams of titanium-nickel based ternary alloys. *Technical Physics Letters* 2002;28:803-805.

- [17] Hosoda H, Tsuji M, Takahashi Y, Inamura T, Wakashima K, Yamabe-Mitarai Y, Miyazaki S, Inoue K. Phase stability and mechanical properties of Ti-Ni shape memory alloys containing platinum group metals. *Materials Science Forum: Trans Tech Publ*; 2003. 2333-2338.
- [18] Tan C, Tian X, Ji G, Gui T, Cai W. Elastic property and electronic structure of TiNiPt high-temperature shape memory alloys. *Solid state communications* 2008;147:8-10.
- [19] Tan C, Tian X, Cai W. Martensitic transformation of TiNiPd high-temperature shape memory alloys: A first-principles study. *Physica B: Condensed Matter* 2009;404:3662-3665.
- [20] Kovarik L, Yang F, Garg A, Diercks D, Kaufman M, Noebe R, Mills M. Structural analysis of a new precipitate phase in high-temperature TiNiPt shape memory alloys. *Acta Materialia* 2010;58:4660-4673.
- [21] Guanjin Y, Jiu D. Recent advances in the study of the TiNiNb shape memory alloy with wide hysteresis. *Rare Metal Materials and Engineering* 1998;27:322-326.
- [22] Siegert W, Neuking K, Mertmann M, Eggeler GF. Influence of Nb content and processing conditions on microstructure and functional properties of NiTiNb shape-memory alloys. *Materials Science Forum: Trans Tech Publ*; 2002. 361-364.
- [23] He X, Rong L, Yan D, Li Y. TiNiNb wide hysteresis shape memory alloy with low niobium content. *Materials Science and Engineering: A* 2004;371:193-197.
- [24] Wu Y, MENG X, Wei C, ZHAO L. Microstructure and mechanical behaviors of TiNiNb wide hysteresis shape memory alloy wire argon arc welding joint. *Material science and technology* 2005;3.
- [25] Xiao M, Li F, Zhao W, Yang G. Constitutive equation for elevated temperature flow behavior of TiNiNb alloy based on orthogonal analysis. *Materials & Design* 2012;35:184-193.
- [26] Mercier O, Melton KN. The substitution of Cu for Ni in NiTi shape memory alloys. *Metallurgical and Materials Transactions A* 1979;10:387-389.
- [27] Rong L, Miller DA, Lagoudas DC. Transformation behavior in a thermomechanically cycled TiNiCu alloy. *Metallurgical and Materials Transactions A* 2001;32:2689-2693.
- [28] Wang Z, Zu X, Feng X, Zhu S, Dai J, Lin L, Wang L. Study of two-way shape memory extension spring of narrow hysteresis TiNiCu shape memory alloys. *Materials Letters* 2002;56:284-288.
- [29] Zu X, Zhang C, Zhu S, Huo Y, Wang Z, Wang L. Electron irradiation-induced changes of martensitic transformation characteristics in a TiNiCu shape memory alloy. *Materials Letters* 2003;57:2099-2103.
- [30] Zu X, Wang L, Huo Y, Lin L, Wang Z, Lu T, Liu L, Feng X. Effect of electron irradiation on the transformation characteristics of narrow hysteresis TiNiCu shape memory alloys. 2002.
- [31] Lin K-N, Wu S-K. Multi-stage transformation in annealed Ni-rich Ti<sub>49</sub>Ni<sub>41</sub>Cu<sub>10</sub> shape memory alloy. *Intermetallics* 2010;18:87-91.
- [32] Otsuka K, Ren X. Recent developments in the research of shape memory alloys. *Intermetallics* 1999;7:511-528.

- [33] Miyazaki S, Kim H, Hosoda H. Development and characterization of Ni-free Ti-base shape memory and superelastic alloys. *Materials Science and Engineering: A* 2006;438:18-24.
- [34] Es-Souni M, Es-Souni M, Fischer-Brandies H. Assessing the biocompatibility of NiTi shape memory alloys used for medical applications. *Analytical and bioanalytical chemistry* 2005;381:557-567.
- [35] Tan S, Miyazaki S, Ueki T, Horikawa H. Ti-content and annealing temperature dependence of transformation behavior of  $\text{Ti}_{92}\text{Ni}_8\text{Cu}_8$  shape memory alloys. *Materials Science and Engineering: A* 1997;230:132-138.
- [36] Nam TH, Kim JH, Kim TY, Lee YK, Kim YW. Superelasticity of Ti-Ni-Cu alloy ribbons fabricated by melt spinning. *Journal of materials science letters* 2002;21:1851-1853.
- [37] Cheng G, Xie Z, Liu Y. Transformation characteristics of annealed  $\text{Ti}_{50}\text{Ni}_{25}\text{Cu}_{25}$  melt spun ribbon. *Journal of Alloys and Compounds* 2006;415:182-187.
- [38] Xie Z, Cheng G, Liu Y. Microstructure and texture development in  $\text{Ti}_{50}\text{Ni}_{25}\text{Cu}_{25}$  melt-spun ribbon. *Acta Materialia* 2007;55:361-369.
- [39] Kim Yw, Nam Th. Shape Memory Characteristics of  $\text{Ti}_{50}\text{Ni}_{20}\text{Cu}_{30}$  Strips Fabricated by Arc Melt Overflow. *International Conference on Martensitic Transformations (ICOMAT)*: Wiley Online Library; 2009. 621-624
- [40] Kim K, Song K, Zhang X, Yi S. Understanding of martensitic (TiCu)-based bulk metallic glasses through deformation behavior of a binary  $\text{Ti}_{50}\text{Cu}_{50}$  martensitic alloy. *Applied Physics Letters* 2008;92.
- [41] Kim YW, Nam TH, Lee SH. Shape Memory Characteristics of  $\text{Ti}_{50}\text{Ni}_{50-x}\text{Cu}_x$  ( $x=35, 40$ ) Alloy Strips. *Advanced Materials Research*: 2008. 463-466.
- [42] Li L, Wang W, Hu L, Ruan Y, Wei B. Lattice properties of supersaturated Ni-Sn solid solutions. *Materials Letters* 2015;160:72-74.
- [43] Funakuba H. Shape memory alloys. USA: Gordon and Breach Publisher; 1987.
- [44] Tellinen J, Suorsa I, Jämskeläinen A, Aaltio I, Ullakko K. Basic properties of magnetic shape memory actuators. 8th international conference ACTUATOR 2002. 566-569.
- [45] Czimmek P. Characterization of magnetic shape memory material. *Siemen VDO Automotive Engineering Report* 2004.
- [46] Henry CP. Dynamic actuation properties of Ni-Mn-Ga ferromagnetic shape memory alloys: Massachusetts Institute of Technology; 2002.
- [47] Tsuchiya K, Tsutsumi A, Ohtsuka H, Umemoto M. Modification of Ni-Mn-Ga ferromagnetic shape memory alloy by addition of rare earth elements. *Materials Science and Engineering: A* 2004;378:370-376.
- [48] Heczko O, Straka L. Temperature dependence and temperature limits of magnetic shape memory effect. *Journal of Applied Physics* 2003;94:7139-7143.
- [49] Massalski TB. Binary alloy phase diagrams. ASM International, Metals Park, OH, 1986;550.
- [50] Arneodo W, Ahlers M. Plastic deformation of martensitic Cu-Zn single crystals. *Scripta metallurgica et materialia* 1973;7:1287-1293.
- [51] Duerig T, Pelton A, Trepanier C. PART I Mechanisms and Behavior. 2011.



- [52] Hanlon J, Butler S, Wasilewski R. Effect of martensitic transformation on the electrical and magnetic properties of NiTi. *Transactions of the Metallurgical Society of AIME* 1967;239:1323-1326.
- [53] Yahia H. *Shape memory implants*: Springer Verlag; 2000.
- [54] Duerig T, Pelton A, Stöckel D. An overview of nitinol medical applications. *Materials Science and Engineering: A* 1999;273:149-160.
- [55] Cai W, Meng X, Zhao L. Recent development of TiNi-based shape memory alloys. *Current Opinion in Solid State and Materials Science* 2005;9:296-302.
- [56] Kumar PK, Lagoudas DC. *Introduction to Shape Memory Alloys*. Shape Memory Alloys: Springer US; 2008. 1-51.
- [57] Wayman C, Duerig T. *An Introduction to Martensite and Shape Memory. Engineering Aspects of Shape Memory Alloys*: Butterworth-Heinemann, 1990. 3-20.
- [58] Otsuka K, Sawamura T, Shimizu K. Crystal structure and internal defects of equiatomic TiNi martensite. *Physica status solidi (a)* 1971;5:457-470.
- [59] Onda T, Bando Y, Ohba T, Otsuka K. Electron microscopy study of twins in martensite in a Ti-50.0 at% Ni alloy. *Materials Transactions, JIM* 1992;33:354-359.
- [60] Gupta S, Johnson A. Morphology and crystallography of beta prime martensite in TiNi alloys. *Japan Institute of Metals, Transactions* 1973;14:292-302.
- [61] Waitz T, Spišák D, Hafner J, Karnthaler H. Size-dependent martensitic transformation path causing atomic-scale twinning of nanocrystalline NiTi shape memory alloys. *Europhysics Letters* 2005;71:98-103.
- [62] Nishida M, Ohgi H, Itai I, Chiba A, Yamauchi K. Electron microscopy studies of twin morphologies in B19' martensite in the Ti-Ni shape memory alloy. *Acta Metallurgica et Materialia* 1995;43:1219-1227.
- [63] Otsuka K, Wayman C. *Shape memory materials*: Cambridge university press; 1999.
- [64] Bojarski Z, Morawiec H. *Metafile z pamięcią kształtu*. Państwowe Wydawnictwo Naukowe, Warszawa 1989.
- [65] Liu Y, Liu Y, Van Humbeeck J. Two-way shape memory effect developed by martensite deformation in NiTi. *Acta Materialia* 1998;47:199-209.
- [66] Perkins J, Hodgson D. The Two-Way Shape Memory Effect A2 - Wayman C, Duerig K, Melton D, Stöckel C. *Engineering Aspects of Shape Memory Alloys*: Butterworth-Heinemann; 1990. 195-206.
- [67] Waram T. *Actuator design using shape memory alloys*: Hamilton, Ont.: TC Waram; 1993.
- [68] Takagi T, Khovailo V, Nagatomo T, Matsumoto M, Ohtsuka M, Abe T, Miki H. Two-way shape memory effect and mechanical properties of Pulse Discharge Sintered Ni<sub>2</sub>.18Mn0.82Ga. 2003.
- [69] Contardo L, Guenin G. Training and two way memory effect in CuZnAl alloy. *Acta Metallurgica et Materialia* 1990;38:1267-1272.
- [70] Miller DA, Lagoudas DC. Thermomechanical characterization of NiTiCu and NiTi SMA actuators: influence of plastic strains. *Smart materials and structures* 2000;9:640.

- [71] Otsuka K, Ren X. Physical metallurgy of Ti–Ni-based shape memory alloys. *Progress in Materials Science* 2005;50:511-678.
- [72] Otsuka K, Shimizu K. Pseudoelasticity and shape memory effects in alloys. *International Metals Reviews* 1986;31:93-114.
- [73] Otsuka K, Wayman C. Reviews on the deformation behavior of materials. Felthman ed., Freund, Israel, Vol II 1977:81.
- [74] Otsuka K, Wayman C. Mechanism of shape memory effect and superelasticity. *Shape Memory Materials* 1998:27-48.
- [75] Jani JM, Leary M, Subic A, Gibson MA. A review of shape memory alloy research, applications and opportunities. *Materials & Design* 2014;56:1078-1113.
- [76] Johnson RW, Evans JL, Jacobsen P, Thompson JR, Christopher M. The changing automotive environment: high-temperature electronics. *Electronics Packaging Manufacturing, IEEE Transactions on* 2004;27:164-176.
- [77] Butera F, Coda A, Vergani G, SpA SG. Shape memory actuators for automotive applications. *Nanotec IT newsletter Roma: AIRI/nanotec IT* 2007:12-16.
- [78] Stoeckel D. Shape memory actuators for automotive applications. *Engineering Aspects of Shape Memory Alloys* 1990:283.
- [79] Browne AL, Alexander PW, Mankame N, Usoro P, Johnson NL, Aase J, Sarosi P, Keefe AC, McKnight GP, Herrera G. SMA heat engines: advancing from a scientific curiosity to a practical reality. *Smart materials, structures and NDT in Aerospace Montreal, Quebec, Canada: CANSMART CINDE IZFP* 2011.
- [80] Stoeckel D, Tinschert F. Temperature compensation with thermovisible rate springs in automatic transmissions. *SAE Technical Paper*; 1991.
- [81] Huett B, Willey C. Design and development of miniature mechanisms for small spacecraft. 2000.
- [82] Hartl DJ, Lagoudas DC. Aerospace applications of shape memory alloys. *Proceedings of the Institution of Mechanical Engineers, Part G: Journal of Aerospace Engineering* 2007;221:535-552.
- [83] Singh K, Chopra I. Design of an improved shape memory alloy actuator for rotor blade tracking. *SPIE's 9th Annual International Symposium on Smart Structures and Materials: International Society for Optics and Photonics*; 2002. 244-266.
- [84] Godard OJ, Lagoudas MZ, Lagoudas DC. Design of space systems using shape memory alloys. *Smart Structures and Materials: International Society for Optics and Photonics*; 2003. 545-558.
- [85] Schetky L. Shape memory alloy applications in space systems. *Engineering Aspects of Shape-Memory Alloys* 1990:170-178.
- [86] Hartl D, Mooney J, Lagoudas D, Calkins F, Mabe J. Use of a Ni60Ti shape memory alloy for active jet engine chevron application: II. Experimentally validated numerical analysis. *Smart materials and structures* 2010;19:015021.
- [87] Hartl D, Lagoudas D, Calkins F, Mabe J. Use of a Ni60Ti shape memory alloy for active jet engine chevron application: I. Thermomechanical characterization. *Smart materials and structures* 2010;19:015020.

- [88] Oehler S, Hartl D, Lopez R, Malak R, Lagoudas D. Design optimization and uncertainty analysis of SMA morphing structures. *Smart materials and structures* 2012;21:094016.
- [89] Honma D, Miwa Y, Iguchi N. Micro robots and micro mechanisms using shape memory alloy. The Third Toyota Conference, Integrated Micro Motion Systems, Micro-machining, Control and Applications 1984.
- [90] Kuribayashi K. A new actuator of a joint mechanism using TiNi alloy wire. *the International journal of Robotics Research* 1986;4:47-58.
- [91] Caldwell D, Taylor P. Artificial muscles as robotic actuators. *Robot Control* 1988 (SYROCO'88): Selected Papers from the 2nd IFAC Symposium, Karlsruhe, FRG, 5-7 October 1988: Elsevier; 2014. 401.
- [92] Kuribayashi K. Millimeter size joint actuator using shape memory alloy. *Micro Electro Mechanical Systems, 1989, Proceedings, An Investigation of Micro Structures, Sensors, Actuators, Machines and Robots IEEE: IEEE; 1989. 139-144.*
- [93] Fujita H. Studies of micro actuators in Japan. *Robotics and Automation, 1989 Proceedings, 1989 IEEE International Conference on: IEEE; 1989. 1559-1564.*
- [94] Furuya Y, Shimada H. Shape memory actuators for robotic applications. *Engineering Aspects of Shape Memory Alloys* 1990:338-355.
- [95] Derby S, Sreekumar M, Nagarajan T, Singaperumal M, Zoppi M, Molfino R. Critical review of current trends in shape memory alloy actuators for intelligent robots. *Industrial Robot: An International Journal* 2007;34:285-294.
- [96] Cepolina F, Michelini RC. Robots in medicine: A survey of in-body nursing aids. *International Symposium on Robotics, France* 2004.
- [97] Menciassi A, Accoto D, Gorini S, Dario P. Development of a biomimetic miniature robotic crawler. *Autonomous Robots* 2006;21:155-163.
- [98] Kate M, Bettencourt G, Marquis J, Gerratt A, Fallon P, Kierstead B, White R, Trimmer B. SoftBot: A soft-material flexible robot based on caterpillar biomechanics. *Tufts University, Medford, MA* 2008;2155.
- [99] Buehler WJ, Wang FE. A summary of recent research on the Nitinol alloys and their potential application in ocean engineering. *Ocean Engineering* 1968;1:105-120.
- [100] Hodgson DE, Ming W, Biermann RJ. Shape memory alloys. *ASM International, Metals Handbook, Tenth Edition* 1990;2:897-902.
- [101] Ryhänen J, Kallioinen M, Tuukkanen J, Junila J, Niemelä E, Sandvik P, Serlo W. In vivo biocompatibility evaluation of nickel-titanium shape memory metal alloy: Muscle and perineural tissue responses and capsule membrane thickness. *Journal of biomedical materials research* 1998;41:481-488.
- [102] Mantovani D. Shape memory alloys: Properties and biomedical applications. *JOM* 2000;52:36-44.
- [103] Dahlgren JM, Gelbart D. System for mechanical adjustment of medical implants. *U.S. Patent Application* 11/902,099[P]. 2007-9-19.
- [104] Pfeifer R, Müller CW, Hurschler C, Kaierle S, Wesling V, Haferkamp H. Adaptable orthopedic shape memory implants. *Procedia CIRP* 2013;5:253-258.
- [105] Lim G, Park K, Sugihara M, Minami K, Esashi M. Future of active catheters. *Sensors and Actuators A: Physical* 1996;56:113-121.

- [106] Wang Y, Zheng G, Zhang X, Zhang Y, Xiao S, Wang Z. Comparative analysis between shape memory alloy-based correction and traditional correction technique in pedicle screws constructs for treating severe scoliosis. *European Spine Journal* 2010;19:394-399.
- [107] Liu CT, Kunsmann H, Wuttig M. Shape-memory materials and phenomena, fundamental aspects and applications. Pittsburgh, PA (United States); Materials Research Society; 1992.
- [108] Christian J. The Theory of Transformations in Metals and Alloys: Part I, II: Elsevier; 2002.
- [109] Nishiyama Z, Fine ME, Meshii M, Wayman CM. Martensitic transformation: Academic Press; 1978.
- [110] Wayman CM. Introduction to the crystallography of martensitic transformations: Macmillan; 1964.
- [111] Michal G, Sinclair R. The structure of TiNi martensite. *Acta Crystallographica Section B: Structural Crystallography and Crystal Chemistry* 1981;37:1803-1807.
- [112] Buhner W, Gotthardt R, Kulik A, Mercier O, Staub F. Powder Neutron Diffraction Study of Nickel--Titanium Martensite. *Journal of Physics F: Metal Physics* 1983;13.
- [113] Tang W, Sundman B, Sandström R, Qiu C. New modelling of the B2 phase and its associated martensitic transformation in the Ti-Ni system. *Acta Materialia* 1999;47:3457-3468.
- [114] Stoeckel D. Forming of nitinol—a challenge. *New Developments in Forging Technology—International conference, Fellbach—Germany* 2003. 119-134.
- [115] Purdy GR, Parr JG. A Study of The Titanium-Nickel System Between Ti<sub>2</sub>Ni and TiNi. *Transactions of the Metallurgical Society of Aime* 1961;221:636-639.
- [116] Dautovic DP, Purdy GR. Phase Transformations in TiNi. *Canadian Metallurgical Quarterly* 1965;4: 129-143.
- [117] Liu Y, Xie Z. Twinning and detwinning of  $\langle 0\ 1\ 1 \rangle$  type II twin in shape memory alloy. *Acta Materialia* 2003;51:5529-5543.
- [118] Hwang CM, Meichle M, Salamon M, Wayman C. Transformation behaviour of a Ti<sub>50</sub>Ni<sub>47</sub>Fe<sub>3</sub> alloy I. Premartensitic phenomena and the incommensurate phase. *Philosophical Magazine A* 1983;47:9-30.
- [119] Schryvers D, Potapov PL. R-phase structure refinement using electron diffraction data. *Materials Transactions* 2002;43:774-779.
- [120] Fukuda T, Saburi T, Chihara T, Tsuzuki Y. Mechanism of B2-B19-B19' transformation in shape memory Ti-Ni-Cu Alloys. *Materials transactions-JIM* 1995;36:1244-1248.
- [121] Nam TH, Saburi T, Shimizu K. Cu-content dependence of shape memory characteristics in Ti-Ni-Cu alloys. *Materials Transactions JIM*, 1990;31: 959-967
- [122] Nam TH, Saburi T, Nakata Y, Shimizu K. Shape memory characteristics and lattice deformation in Ti-Ni-Cu alloys. *Materials Transactions JIM* 1990;31:1050-1056.
- [123] Bricknell R, Melton K, Mercier O. The structure of NiTiCu shape memory alloys. *Metallurgical and Materials Transactions A* 1979;10:693-697.

- [124] Rösner H, Schloßmacher P, Shelyakov A, Glezer A. The influence of coherent plate-like precipitates on the thermoelastic martensitic transformation in melt-spun Ti50Ni25Cu25 shape memory alloys. *Acta Materialia* 2001;49:1541-1548.
- [125] Tong Y, Liu Y, Xie Z, Zarinejad M. Effect of precipitation on the shape memory effect of Ti50Ni25Cu25 melt-spun ribbon. *Acta Materialia* 2008;56:1721-1732.
- [126] Huang X, Ackland GJ, Rabe KM. Crystal structures and shape-memory behaviour of NiTi. *Nature Materials* 2003;2:307-311.
- [127] Kudoh Y, Tokonami M, Miyazaki S, Otsuka K. Crystal structure of the martensite in Ti-49.2 at.% Ni alloy analyzed by the single crystal X-ray diffraction method. *Acta Metallurgica* 1985;33:2049-2056.
- [128] Buhner W, Gotthardt R, Kulik A, Mercier O, Staub F. Powder neutron diffraction study of nickel-titanium martensite. *Journal of Physics F: Metal Physics* 2000;13:77.
- [129] Kresse G, Hafner J. Ab initio molecular dynamics for liquid metals. *Physical Review B* 1993;47:558.
- [130] Kresse G, Furthmüller J. Efficient iterative schemes for ab initio total-energy calculations using a plane-wave basis set. *Physical Review B* 1996;54:11169.
- [131] Šesták P, Černý M, Pokluda J. Can twinning stabilize B19' structure in NiTi martensite? *Intermetallics* 2011;19:1567-1572.
- [132] Gonze X, Beuken J-M, Caracas R, Detraux F, Fuchs M, Rignanese G-M, Sindic L, Verstraete M, Zerah G, Jollet F. First-principles computation of material properties: the ABINIT software project. *Computational Materials Science* 2002;25:478-492.
- [133] Gonze X. A brief introduction to the ABINIT software package. *Zeitschrift für Kristallographie* 2005;220:558-562.
- [134] Guda Vishnu K, Strachan A. Phase stability and transformations in NiTi from density functional theory calculations. *Acta Materialia* 2010;58:745-752.
- [135] Schultz P, Muller R. SeqQuest Electronic Structure Code. Sandia National Laboratories Albuquerque, NM; 2002.
- [136] Kibey S, Sehitoglu H, Johnson D. Energy landscape for martensitic phase transformation in shape memory NiTi. *Acta Materialia* 2009;57:1624-1629.
- [137] Teng Y, Zhu S, Wang F, Wu W. Electronic structures and shape-memory behavior of Ti50Ni50-xCux(x= 0, 6.25, 12.5, 18.75 and 25.0 at%) by density functional theory. *Physica B: Condensed Matter* 2007;393:18-23.
- [138] Šesták P, Černý M, Pokluda J. Influence of normal stress on shear strength along  $\langle 111 \rangle \{110\}$  and  $\langle 111 \rangle \{112\}$  deformation paths in B2 NiTi alloy from first principles. *Materials Science and Engineering: A* 2008;481:247-249.
- [139] Ezaz T, Sehitoglu H, Maier H. Energetics of twinning in martensitic NiTi. *Acta Materialia* 2011;59:5893-5904.
- [140] Wang XQ. Twinned structure for shape memory: first-principles calculations. *Physical Review B* 2008;78:092103.
- [141] Ezaz T, Sehitoglu H, Abuzaid W, Maier HJ. Higher order twin modes in martensitic NiTi—The  $(201\bar{1})$  case. *Materials Science and Engineering: A* 2012;558:422-430.
- [142] Wang J, Sehitoglu H. Resolving quandaries surrounding NiTi. *Applied Physics Letters* 2012;101:081907.

- [143] Ezaz T, Wang J, Sehitoglu H, Maier HJ. Plastic deformation of NiTi shape memory alloys. *Acta Materialia* 2013;61:67-78.
- [144] Sholl D, Steckel JA. *Density functional theory: a practical introduction*: Wiley-Interscience; 2011.
- [145] Hartree DR. The wave mechanics of an atom with a non-Coulomb central field. Part I. Theory and methods. *Mathematical Proceedings of the Cambridge Philosophical Society*: Cambridge University Press; 1928. 89-110.
- [146] Koch W, Holthausen MC. *A chemist's guide to density functional theory*: Wiley-Vch Weinheim; 2001.
- [147] Hohenberg P, Kohn W. Inhomogeneous electron gas. *Physical Review* 1964;136:B864.
- [148] Kohn W, Sham LJ. Self-consistent equations including exchange and correlation effects: APS; 1965.
- [149] Gilbert T. Hohenberg-Kohn theorem for nonlocal external potentials. *Physical Review B* 1975;12:2111.
- [150] Hedin L, Lundqvist B. Explicit local exchange-correlation potentials. *Journal of Physics C Solid State Physics* 1971;4:2064-2083.
- [151] Ceperley DM, Alder B. Ground state of the electron gas by a stochastic method. *Physical Review Letters* 1980;45:566-569.
- [152] Becke AD. Density-functional thermochemistry. I. The effect of the exchange-only gradient correction. *The Journal of chemical physics* 1992;96:2155.
- [153] Becke AD. Density-functional thermochemistry. II. The effect of the Perdew-Wang generalized-gradient correlation correction. *Journal of Chemical Physics* 1992;97:9173-9177.
- [154] Becke AD. Density-functional thermochemistry. III. The role of exact exchange. *The Journal of chemical physics* 1993;98:5648.
- [155] Payne MC, Teter MP, Allan DC, Arias T, Joannopoulos J. Iterative minimization techniques for ab initio total-energy calculations: molecular dynamics and conjugate gradients. *Reviews of Modern Physics* 1992;64:1045-1097.
- [156] Clark SJ, Segall MD, Pickard CJ, Hasnip PJ, Probert MIJ, Refson K, Payne MC. First principles methods using CASTEP. *Zeitschrift für Kristallographie* 2005;220:567-570.
- [157] Kleinman L, Bylander D. Efficacious form for model pseudopotentials. *Physical Review Letters* 1982;48:1425-1428.
- [158] Vanderbilt D. Soft self-consistent pseudopotentials in a generalized eigenvalue formalism. *Physical Review B* 1990;41:7892.
- [159] Perdew JP, Zunger A. Self-interaction correction to density-functional approximations for many-electron systems. *Physical Review B* 1981;23:5048.
- [160] Perdew JP, Chevary J, Vosko S, Jackson KA, Pederson MR, Singh D, Fiolhais C. Atoms, molecules, solids, and surfaces: Applications of the generalized gradient approximation for exchange and correlation. *Physical Review B* 1992;46:6671.
- [161] Probert M. Improved algorithm for geometry optimisation using damped molecular dynamics. *Journal of Computational Physics* 2003;191:130-146.

- [162] Srivastava G, Weaire D. The theory of the cohesive energies of solids. *Advances in Physics* 1987;36:463-517.
- [163] Segall M. Population analysis in plane wave electronic structure calculations. *Molecular Physics* 1996;89:571-577.
- [164] Segall M, Shah R, Pickard C, Payne M. Population analysis of plane-wave electronic structure calculations of bulk materials. *Physical Review B* 1996;54:16317.
- [165] Sanchez-Portal D, Artacho E, Soler JM. Projection of plane-wave calculations into atomic orbitals. *Solid state communications* 1995;95:685-690.
- [166] Mulliken RS. Electronic Population Analysis on LCAO MO Molecular Wave Functions. I. *The Journal of chemical physics* 1955;23:1833-1840.
- [167] Firstov G, Van Humbeeck J, Koval YN. High temperature shape memory alloys problems and prospects. *Journal of intelligent material systems and structures* 2006;17:1041-1047.
- [168] Firstov G, Van Humbeeck J, Koval YN. High-temperature shape memory alloys: some recent developments. *Materials Science and Engineering: A* 2004;378:2-10.
- [169] Firstov G, Van Humbeeck J, Koval YN. Comparison of high temperature shape memory behaviour for ZrCu-based, Ti-Ni-Zr and Ti-Ni-Hf alloys. *Scripta materialia* 2004;50:243-248.
- [170] Nishida M, Chiba A, Ueda T, Toyama Y. Phase Transformations in Ti40Ni60-XCuX Alloys. *Materials Science Forum: Materials Science Forum*. 1991, 56: 599-604.
- [171] Tang W, Sandström R, Wei Z, Miyazaki S. Experimental investigation and thermodynamic calculation of the Ti-Ni-Cu shape memory alloys. *Metallurgical and Materials Transactions A* 2000;31:2423-2430.
- [172] Saburi T, Watanabe Y, Nenno S. Morphological characteristics of the orthorhombic martensite in a shape memory Ti-Ni-Cu alloy. *ISIJ International* 1989;29:405-411.
- [173] Tadaki T, Wayman C. Electron microscopy studies of martensitic transformations in Ti50Ni50-xCu alloys. Part I. Compositional dependence of one-third reflections from the matrix phase. *Metallography* 1982;15:233-245.
- [174] Miyazaki S, Mizukoshi K, Ueki T, Sakuma T, Liu Y. Fatigue life of Ti-50 at.% Ni and Ti-40Ni-10Cu (at.%) shape memory alloy wires. *Materials Science and Engineering: A* 1999;273:658-663.
- [175] Strnadel B, Ohashi S, Ohtsuka H, Miyazaki S, Ishihara T. Effect of mechanical cycling on the pseudoelasticity characteristics of TiNi and TiNiCu alloys. *Materials Science and Engineering: A* 1995;203:187-196.
- [176] Strnadel B, Ohashi S, Ohtsuka H, Ishihara T, Miyazaki S. Cyclic stress-strain characteristics of TiNi and TiNiCu shape memory alloys. *Materials Science and Engineering: A* 1995;202:148-156.
- [177] Xie ZL, Van Humbeeck J, Liu Y, Delaey L. TEM study of Ti50Ni25Cu25 melt spun ribbons. *Scripta materialia* 1997;37:363-371.
- [178] Grossmann C, Frenzel J, Sampath V, Depka T, Oppenkowski A, Somsen C, Neuking K, Theisen W, Eggeler G. Processing and property assessment of NiTi and

- NiTiCu shape memory actuator springs. *Materialwissenschaft Und Werkstofftechnik* 2008;39:499-510.
- [179] Grossmann C, Frenzel J, Sampath V, Depka T, Eggeler G. Elementary transformation and deformation processes and the cyclic stability of NiTi and NiTiCu shape memory spring actuators. *Metallurgical and Materials Transactions A* 2009;40:2530-2544.
- [180] Jhi S-H, Ihm J, Louie SG, Cohen ML. Electronic mechanism of hardness enhancement in transition-metal carbonitrides. *Nature* 1999;399:132-134.
- [181] Haydock R, Heine V, Kelly M. Electronic structure based on the local atomic environment for tight-binding bands. *Journal of Physics C: Solid State Physics* 1972;5:2845.
- [182] Ravi C, Vajeeston P, Mathijaya S, Asokamani R. Electronic structure, phase stability, and cohesive properties of Ti<sub>2</sub>XAl (X= Nb, V, Zr). *Physical Review B* 1999;60:15683.
- [183] Simon A. Intermetallic compounds and the use of atomic radii in their description. *Angewandte Chemie International Edition in English* 1983;22:95-113.
- [184] Zarinejad M, Liu Y, White TJ. The crystal chemistry of martensite in NiTiHf shape memory alloys. *Intermetallics* 2008;16:876-883.
- [185] Gou L, Liu Y, Ng TY. An investigation on the crystal structures of Ti<sub>50</sub>Ni<sub>50-x</sub>Cu<sub>x</sub> shape memory alloys based on density functional theory calculations. *Intermetallics* 2014;53:20-25.
- [186] Nam TH, Saburi T, Kawamura Y, Shimizu Ki. Shape Memory Characteristics Associated With the B2  $\leftrightarrow$  B19 and B19  $\leftrightarrow$  B19' Transformations in a Ti-40Ni-10Cu(at.%) Alloy. *Materials Transactions, JIM* 1990;31:262-269.
- [187] Gordy W. A relation between bond force constants, bond orders, bond lengths, and the electronegativities of the bonded atoms. *The Journal of chemical physics* 1946;14:305-320.